

**CHARACTERIZING THE MECHANICAL BEHAVIOR OF  
EXTRACELLULAR MATRIX NETWORKS *IN SITU***

by

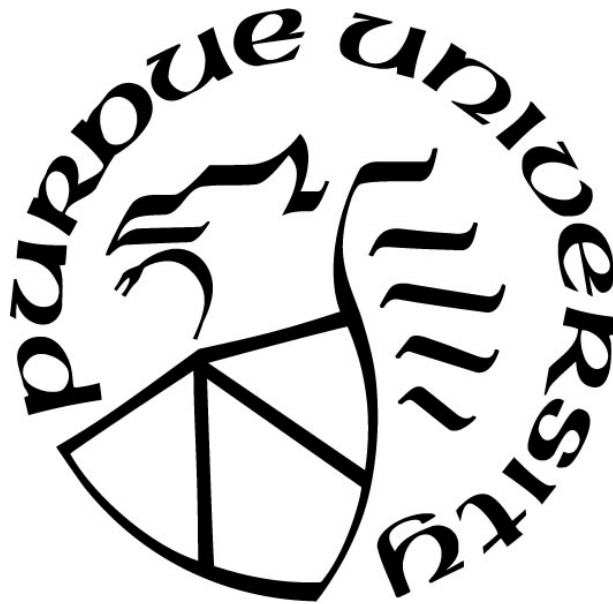
**Andrea Acuña Briceño**

**A Dissertation**

*Submitted to the Faculty of Purdue University*

*In Partial Fulfillment of the Requirements for the degree of*

**Doctor of Philosophy**



Weldon School of Biomedical Engineering

West Lafayette, Indiana

August 2020

**THE PURDUE UNIVERSITY GRADUATE SCHOOL  
STATEMENT OF COMMITTEE APPROVAL**

**Dr. Sarah Calve, Chair**

Weldon School of Biomedical Engineering

**Dr. Craig J. Goergen**

Weldon School of Biomedical Engineering

**Dr. Adrian Buganza Tepole**

School of Mechanical Engineering

**Dr. Abigail Cox**

Department of Comparative Pathobiology

**Approved by:**

Dr. George R. Wodicka

*To my parents Gabriela & Rafael; for everything I am began with you*

## ACKNOWLEDGMENTS

The following document is the culmination of years of work made possible by the constant support and guidance of mentors, friends, and family. First and foremost, I want to express my most sincere appreciation to my advisor, Dr. Sarah Calve, for trusting me with the incredible opportunity and responsibility to help further establish her research lab. Sarah always encouraged me to think independently and critically, while also making herself available to provide guidance. She gave me the freedom to explore my research and professional interests as I navigated my graduate career and pursued my professional and personal development. I am continually inspired by Sarah's innovative thinking, passion for science, and her enthusiasm, not only when teaching me a new technique at the bench, but also while editing my many early attempts at scientific writing. I also want to thank my co-advisor Dr. Craig Goergen for his mentorship throughout my graduate career. Craig cultivates a positive lab environment encouraging students to support and uplift each other. I am deeply grateful for the opportunity to be a part of his group and for the many opportunities to practice communicating my work and research interests.

Thank you to my dissertation committee members, Dr. Adrian Buganza Tepole and Dr. Abigail Cox. Dr. Buganza Tepole was always open to discuss my work and ask critical questions about some of the most challenging parts of my projects. I want to thank Dr. Cox for encouraging me to strategize and set ambitious, yet attainable goals. I would like to acknowledge the faculty at Purdue who have supported me, particularly those who are also research collaborators, such as Drs. David Umulis, Vitaliy Rayz, Jacqueline Linnes, Chelsea Davis, and Luis Solorio. The supportive and collaborative environment in the department had a great positive impact on my graduate school experience and my development as a scientist. Additionally, I would like to thank the staff at the Weldon School of Biomedical Engineering for everything they do to support graduate students on a daily basis. I especially want to thank Tammy Siemers for all her incredible work towards facilitating professional development opportunities, from coordinating career exploration trips all over the country to helping me set goals for my individual development plan.

I want to thank all of the members of the Musculoskeletal Extracellular Matrix Lab (MEML) and the Cardiovascular Imaging Research Lab (CVIRL), particularly those who worked closely with me on the projects presented in this dissertation, including Julian Jimenez, Yue Leng, Kathryn Jacobson, Alex Ocken, Michael Drakopoulos, and Sydney Sofronici. I am deeply grateful

for the support and friendship from past and present labmates, especially Arvin, Alycia, Amelia, Evan, Gurneet, Jessica, Juan Martin, and Katie, and the many conversations over lab lunches. There are many other individuals I would like to thank for making my experiences at Purdue memorable and that much more enjoyable. In Rachel, Carmen, Divya, Elizabeth, K, Taylor, and Tran I have found wonderful friends and outstanding support during challenging times, both in research and in life, and for that I'm deeply grateful. I thank them for the many reminders to find joy in the small things and their countless words of encouragement. I also want to thank the Biomedical Engineering Graduate Student Association (BMEGSA) for creating a sense of community among graduate students, establishing a great support network, and providing professional development opportunities.

Next, I want to express my deepest gratitude to my parents, Gabriela and Rafael. My journey towards completing this doctoral degree would not have been possible without their unwavering love and support, the values they instilled in me, and the many opportunities I have been able to pursue because they believed in the value of education. I want to thank them for teaching me to persevere towards my goals and always encouraging my scientific curiosity; even as a child fascinated by looking at bugs under a microscope. I also want to thank my brother, Rafael, my extended family, aunts and uncles, family friends, as well as my college and high school friends who continuously shared words of encouragement from afar.

Finally, I would like to acknowledge the Weldon School of Biomedical Engineering and the Purdue Graduate School for granting me the Frederick N. Andrews and the Bilsland Dissertation Fellowships. It was through these funding opportunities that I was able to carry out the research presented in this dissertation.

## PREFACE

Two chapters of this dissertation (**Chapters 2 and 3**) have been published in peer-reviewed journals as noted at the start of those chapters. Minor edits to the formatting and wording have been made in these chapters to produce a cohesive piece of writing. The organization of this dissertation begins with an introduction to the extracellular matrix and an in-depth overview of its role in biological tissues. Next, the approaches used to characterize extracellular matrix mechanics are reviewed and a more comprehensive thesis overview is presented. **Chapter 2** focuses on the development of a novel technique to enhance extracellular matrix visualization in embryonic tissues without disrupting their integrity. **Chapter 3** describes experimental and computational methodologies for the quantification of extracellular matrix strain. **Chapters 4 and 5** are presented as manuscripts currently in preparation, focused on the development of tensile testing systems for soft tissues and extracellular matrix networks. **Chapter 4** includes a characterization of embryonic and postnatal tendon mechanics. This is followed by the investigation of extracellular matrix networks in embryonic tissues under tension (**Chapter 5**). Finally, we conclude this dissertation by reflecting on its contributions, as well as providing future directions for the work presented (**Chapter 6**). A complete list of authored journal articles can be found in the Publications section.

# TABLE OF CONTENTS

LIST OF TABLES.....	10
LIST OF FIGURES .....	11
LIST OF ABBREVIATIONS.....	18
ABSTRACT.....	19
1. INTRODUCTION .....	20
1.1 Background.....	20
1.1.1 The extracellular matrix and its role in biological tissues .....	20
1.1.2 Fibril and Network Forming ECM Molecules.....	21
1.1.3 ECM organization and mechanics .....	23
1.1.4 Approaches to characterize ECM mesoscale mechanics.....	27
1.2 Thesis overview: characterizing extracellular matrix networks <i>in situ</i> .....	30
2. THREE DIMENSIONAL VISUALIZATION OF EXTRACELLULAR MATRIX NETWORKS DURING MURINE DEVELOPMENT .....	33
2.1 Abstract.....	33
2.2 Introduction.....	34
2.3 Materials and methods .....	35
2.3.1 Embryo harvest.....	35
2.3.2 Embryo decellularization.....	36
2.3.3 Fluorescent labeling of ECM.....	38
2.3.4 Clearing of control tissues .....	39
2.3.5 Cryosectioning of control tissues.....	39
2.3.6 Imaging.....	39
2.3.7 Image processing .....	41
2.3.8 Ultrasound quantification of embryo swelling .....	41
2.3.9 Statistical analyses .....	41
2.4 Results and Discussion .....	43
2.4.1 Decellularization increases embryo transparency .....	43
2.4.2 Independent ECM networks are maintained after cell removal .....	44
2.4.3 Intact embryos can be visualized at multiple scales .....	47

2.4.4	The epidermis is linked to the underlying musculoskeletal tissues via proteoglycan-rich fibrils.....	48
2.5	Conclusions.....	49
3.	<i>IN SITU</i> MEASUREMENT OF NATIVE EXTRACELLULAR MATRIX STRAIN .....	50
3.1	Abstract.....	50
3.2	Introduction.....	51
3.3	Experimental procedures .....	52
3.3.1	Visualization of ECM fibril architecture in 3D .....	52
3.3.2	Quantification of ECM displacement .....	55
3.3.3	Validating fibril displacements.....	59
3.3.4	Calculation of the Green-Lagrange strain tensor.....	61
3.4	Results.....	64
3.4.1	Fibril deformation.....	64
3.4.2	Fibril strain.....	64
3.4.3	Displacement error.....	67
3.5	Discussion.....	67
4.	DESIGN AND VALIDATION OF A MODULAR MICRO-ROBOTIC SYSTEM FOR THE MECHANICAL CHARACTERIZATION OF SOFT TISSUES.....	74
4.1	Abstract.....	74
4.2	Introduction.....	75
4.3	Materials and Methods.....	77
4.3.1	Development of a modular tensile testing system .....	77
4.3.2	Sample preparation .....	80
4.4	Results.....	85
4.4.1	Spring design .....	85
4.4.2	Spring-micromanipulator system comparison to bulk tensile tester.....	87
4.4.3	Uniaxial loading of various materials.....	88
4.5	Statistical methods .....	91
4.6	Discussion.....	91
5.	CHARACTERIZATION OF EXTRACELLULAR MATRIX NETWORKS UNDER TENSION .....	96

5.1	Abstract.....	96
5.2	Introduction.....	97
5.3	Materials and Methods.....	99
5.3.1	Tendon decellularization for enhanced ECM visualization.....	99
5.3.2	Preliminary uniaxial loading on confocal microscope .....	101
5.3.3	Uniaxial loading using micromanipulator system on confocal .....	104
5.3.4	Ultrastructure of embryonic and postnatal tendons .....	107
5.4	Results.....	108
5.5	Discussion.....	111
6.	CONCLUSIONS AND FUTURE DIRECTIONS .....	119
	APPENDIX A. SUPPLEMENT TO CHAPTER 4.....	121
	APPENDIX B. SUPPLEMENT TO CHAPTER 5.....	122
	REFERENCES .....	124
	PUBLICATIONS.....	137

## LIST OF TABLES

Table 2.1. Composition of hydrogel solution to create polyacrylamide framework. Modified from Chung <i>et al.</i> , 2013 <sup>78</sup> . .....	38
Table 2.2 Antibodies and stains used for fluorescent labeling of embryonic ECM. ....	38
Table 3.1. FIDVC absolute displacement error .....	72
Table 4.1. Tangent moduli of E16.5 and E18.5 tendons.....	94

## LIST OF FIGURES

- Figure 1.1. Schematic representation of cells sensing mechanical stimuli from ECM fibrils in their surroundings via the ECM- integrin ( $\alpha\beta$ )- cytoskeleton path. Adapted from Doyle and Yamada and Heinegård and Saxne. .... 21
- Figure 1.2. Hierarchical structure of tendon from the single type I collagen molecule up to fibrils, fascicles, and whole tendon, including the ECM fibrils at the mesoscale (50 nm – 300  $\mu$ m), and describing the structure of fibril-associated proteoglycans (from Connizzo *et al.*)..... 22
- Figure 1.3. Comparison of network organization of type I collagen and fibrillin-2 between embryonic tendon and skin. Images of these decellularized tissues were acquired at 20 $\times$  and then processed and 3D reconstructed using FIJI *3D Viewer* (bars=20  $\mu$ m). .... 25
- Figure 1.4. Visual representation of the mesoscale (b) between the single fibril (a) and the bulk tissue scales (c) . a. Transmission electron microscopy image of a postnatal murine tendon showing collagen fibrils along the short axis acquired at 18,500 $\times$ . b. Fibrillin-2 (white) and fibronectin (red) networks in an embryonic decellularized murine tendon acquired at 20 $\times$ . c. Adult murine tibialis anterior tendon shown with respective bone and muscle insertions, imaged with a dissecting scope at 0.75 $\times$ . .... 26
- Figure 2.1. Decellularization increases transparency of murine embryos. (A) Isolated murine embryos were incubated in hydrogel solution (Table 2.1) and gently rocked at 4  $^{\circ}$ C overnight. Excess hydrogel was removed, and embryos were submerged in mineral oil at 37  $^{\circ}$ C to induce polymerization. Embryos were decellularized in sodium dodecyl sulfate (SDS) with protease inhibitor (PI) then processed for immunohistochemistry. (B) Comparison of control and decellularized E12.5 embryos from the same litter showed swelling occurred after cell removal; however, overall morphology was retained. Bar = 2 mm. (C) Ultrasound setup used to quantify changes in embryonic volume and segmentations (blue) of a E14.5 embryo before decellularization for whole body 3D rendering. Bar = 2 mm. (D) Volume changes remained consistent over the time periods investigated (n = 4; bars = SD) and were largely isotropic (see **Fig. 2.5**). .... 36
- Figure 2.2 Influence of SDS concentration on ECM visualization. E12.5 embryos were permeated with hydrogel, decellularized with 0.03 – 0.3% SDS and then stained for nuclei (DAPI, blue), proteoglycans (WGA, green), fibronectin (red) and fibrillin-2 (white). Control samples were not incubated in hydrogel or SDS. Eyes were imaged at 25 $\times$ . Nuclei became disrupted as SDS increased but DNA was not completely removed. WGA labeling substantially decreased with SDS treatment, due to the removal of cell surface proteoglycans. FN and FBN2 could only be visualized at 0.05 – 0.3% SDS. Bar = 100  $\mu$ m..... 37
- Figure 2.3 Decellularization increases matrix visibility and retains independent networks. (A) E14.5 control and decellularized forelimbs were stained for fibronectin (FN; red) and fibrillin- 2 (FBN2; white) and digit tips were imaged using confocal microscopy (blue = DAPI). Bar = 100  $\mu$ m. (B) Higher magnification view of A reveals FN and FBN2 maintain independent, interpenetrating networks after removal of cells with SDS. Arrowheads show FN+ blood vessels. Bar = 50  $\mu$ m. (C, D) The native distribution of different ECM was maintained in developing cartilage and bone in decellularized E14.5 forelimbs. Tenascin-C (TNC, red) expression was

restricted to the periphery of the developing cartilage (left). FBN2 (red) was localized to fibrils within the cartilage (middle). YZ section shows extended FBN2-expressing microfibril (arrowhead). Type VI collagen (col VI, red) was found throughout the developing cartilage (right). Green = WGA. Bars = 50  $\mu\text{m}$ . Dimensions of stacks in C: 237  $\times$  237  $\times$  78  $\mu\text{m}$  (x  $\times$  y  $\times$  z). (D) TNC (red, left) was restricted to the perichondrium/periosteum in the developing long bone, whereas perlecan (red, right) was found throughout the tissue. Green = WGA. Bars = 100  $\mu\text{m}$ , axes oriented as in C. Dimensions of stacks in D: 242  $\times$  338  $\times$  69  $\mu\text{m}$ . ..... 40

Figure 2.4 3D visualization of ECM in E12.5 embryo. (A) Widefield view of WGA-stained E12.5 decellularized embryo. (A') Virtual confocal section of E12.5 embryo stained with WGA (green) and type VI collagen (red). Various structures can be identified including the 4th ventricle of the brain (v), future cerebral cortex (cc), vomeronasal organ (vo), scapula (s), midgut (m), liver (l), heart (h) and ribs (r). 10 $\times$ , bar = 2 mm. (B-B''): 3D rendering of the eye at 25 $\times$  (567  $\times$  567  $\times$  395  $\mu\text{m}$ ; x  $\times$  y  $\times$  z). The vascularization of the vitreous body (vb) can be visualized (B') and the lens and optic nerve can be clearly resolved in a YZ projection of the image stack. Bars = 100  $\mu\text{m}$ . (C-C'') 3D rendering reveals dense vascular network around the elbow (567  $\times$  567  $\times$  186  $\mu\text{m}$ ). Comparison of XY (C') and YZ planes (C'') revealed that blood vessels remained patent. 25 $\times$ , bars = 100  $\mu\text{m}$ . (D-D'') 3D rendering of developing spinal cord at 10 $\times$  (850  $\times$  850  $\times$  251  $\mu\text{m}$ ). Z-projection of 12 slices (70  $\mu\text{m}$ ) shows maintenance of spinal cord vascularization (D') and intact blood vessel in the YZ projection (arrowhead; D''). Bars = 200  $\mu\text{m}$ . ..... 42

Figure 2.5. No significant differences in embryo swelling at earlier stages of development. (A) Location of the area measurements taken before and after decellularization to quantify expansion from 3D segmentations. Scale bar=2 mm. (B) Percentage change in areas in different anatomical imaging planes. The percentages of change in different planes are only statistically significant at E14.5, suggesting swelling is isotropic at the earlier stages (n=4; \*p<0.05; \*\*p<0.005; error bars = SD). ..... 43

Figure 2.6. Multiscale imaging of the musculoskeletal system in the developing forelimb. E12.5 (A – C) and E14.5 (D – F) forelimbs were decellularized and stained with WGA (green) and an antibody against fibrillin-2 (FBN2, red). Dorsal view. (A, D) Cartilage elements of the autopod and zeugopod were easily resolved with WGA. FBN2 became more restricted with time. 10 $\times$ , bar = 500  $\mu\text{m}$ . (A: 2471  $\times$  3599  $\times$  600  $\mu\text{m}$ ; D: 2799  $\times$  4733  $\times$  450  $\mu\text{m}$ ; x  $\times$  y  $\times$  z) (B, E) 3D rendering of digits showed a network of WGA+ fibrils radiating from the cartilage as well as staining of joint tissues and the extensor tendons. 25 $\times$ , bar = 100  $\mu\text{m}$ . (381  $\times$  1364  $\times$  289  $\mu\text{m}$ ). (C, F) Higher magnification of digits in B, E (\*) revealed WGA+ fibrils extended from dorsal epidermis (epi) to cartilage (c) at E12.5 and at E14.5 fibrils appeared to connect the extensor tendons (t) to the epidermis and cartilage. 40 $\times$ , bars = 50  $\mu\text{m}$ , (213  $\times$  213  $\times$  227  $\mu\text{m}$ ). ..... 45

Figure 2.7. SeeDB is not effective for visualization of ECM within the developing embryo. E14.5 forelimbs were either cleared with SeeDB or decellularized and stained for fibrillin-2 or WGA. Virtual cross-sections at 10 $\times$  demonstrate that staining in SeeDB samples is mostly restricted to the periphery. Higher resolution imaging (63 $\times$ ) of a tendon within the zeugopod reveals minimal penetration of FBN2 antibody and WGA in to SeeDB sample (epidermis is to the left of the image). ..... 46

Figure 2.8. Differential penetration of antibodies into decellularized embryos. Anti-perlecan (blue) showed substantial more penetration into the decellularized E12.5 embryo from Fig. 3 than anti-type VI collagen (red), suggesting antibody penetration is limited by concentration rather than

diffusion. For example, perlecan in the blood vessels of the corpus callosum (arrowhead) were labeled at least 1mm deep. 10×, bar = 2 mm..... 47

Figure 2.9. Presence of fibrillar networks within intact tissues. E14.5 forelimbs were sectioned and stained with WGA (green) and an antibody against fibrillin-2 (red). Fibrils (f) extending between the epidermis (e) and cartilage (c) were observed on the ventral side of the developing digit. Blue = DAPI, 25×, bar = 50 μm. .... 48

Figure 3.1. Experimental procedure. **a.** Decellularization of murine embryonic forelimbs allows the visualization of the extracellular matrix in its native conformation using confocal microscopy, after staining for ECM of interest. Decellularized forelimbs are imaged with an inverted confocal microscope while submerged in PBS. Embryo decellularization panels adapted from [12]. **b.** Volume images obtained before (cyan) and after load (magenta), corresponding to the same area of the digit, are correlated to extract displacements with fast iterative digital volume correlation (FIDVC). Displacements are analyzed and plotted in color as vector fields. Strain is calculated by fitting polynomial functions to each set of displacement values and then calculating their derivatives analytically, indicated by  $u(x)$  and  $u'(x)$ . .... 53

Figure 3.2. Representative confocal images of a decellularized murine forelimb. **a.** Global confocal image of the developing forelimb stained with wheat germ agglutinin (WGA; green) and for fibrillin-2 (red) at 10× (bottom; scale bar = 500 μm) and at 25×, focusing on the distal phalange (top; scale bar = 100 μm). The location of the cartilage and the adjacent loose connective tissue are boxed and labeled in white. Dashed box (white) represents the area analyzed when quantifying regional differences, including both cartilage and the adjacent loose connective tissue in the same sub-stack. **b.** Composite images of the loose connective tissue (top) and the cartilage (bottom), indicating the spatial distribution of fibrillin-2 (red) and WGA (green) (scale bar = 100 μm). **c.** Composite images of a representative sub-stack in the loose connective tissue (top) and the cartilage (bottom) corresponding to fibrillin-2 (left) and WGA (right), showing an overlay of the reference (cyan) and compressed (magenta) (scale bar = 10 μm). .... 56

Figure 3.3. Representative deformation response from sample B for WGA and fibrillin-2 sub-stacks of  $22 \times 22 \times 15 \mu\text{m}^3$  in the cartilage and loose connective tissue. Displacements are represented as vector fields with color representing magnitude from 0 to 8 μm. Maximum principal strain ( $E_1$ ) is shown on the surface of the segmented ECM networks with color representing magnitude ranging from -0.4 to 0.8. .... 58

Figure 3.4. Displacement fields for representative ECM sub-stacks from sample B.  $u_x, u_y,$  and  $u_z$  were plotted for FBN2 and WGA in the loose connective tissue (top) and the cartilage (bottom) regions with color indicating magnitude and directionality of displacement. .... 59

Figure 3.5. Comparison of maximum principal strain ( $E_1$ ) from large ECM networks. **a.** Representative ECM networks fibrillin-2 (left) and WGA (right) segmented in 3D with color representing the magnitude of  $E_1$  (scale bar=50 μm). **b.** Average  $E_1$  for each protein in each region from the large ECM networks across 5 different embryonic samples is dependent on protein ( $p \leq 0.032$ , two-way ANOVA). Tukey post-hoc comparison did not show significant differences between individual groups ( $n=5$ ; bar =S.D.)..... 63

Figure 3.6. Comparison of independent samples reveals similar trends in ECM strain profiles. Maximum principal strain ( $E_1$ ) for sample A (left) and sample B (right) was dependent on both

protein and region ( $p \leq 0.0021$ ;  $p \leq 0.032$ , respectively, two-way ANOVA). Tukey post-hoc comparison showed significant differences between individual groups ( $*0.0021 < p \leq 0.032$ ;  $**0.0002 < p \leq 0.0021$ ) ( $n=3$ ; bars = S.D.)..... 65

Figure 3.7. Error quantification and analysis. **a.** Representative displacement vector field resulting from the fast-iterative digital volume correlation (FIDVC) of the same configuration imaged twice, without the application of load for WGA (top) and FBN2 (bottom). Displacement magnitude (in the order of picometers) is shown with color in the vector field. **b.** Representative absolute displacement error distribution for fibrin gel compression experiment and FIDVC. **c.** Displacement fields of the fibrils (top) and the fluorescent particles (bottom) in the fibrin gels generated for FIDVC displacement validation. **d.** Representative absolute difference between the FIDVC-calculated displacement of fluorescent particles and the adjacent fibrils. .... 66

Figure 3.8. Comparison of Green-Lagrange strain components across independent samples. **a.** Significant differences between normal strains ( $E_{xx}$ ,  $E_{yy}$ ,  $E_{zz}$ ) across proteins and regions for sample A (left) and sample B (right) identified via a two-way ANOVA post-hoc Tukey test comparison are shown ( $*0.0021 < p \leq 0.032$ ;  $**0.0002 < p \leq 0.0021$ ) ( $n=3$ ; bars = S.D.), revealing similar trends in ECM strain profiles. **b.** Shear strain components ( $E_{xy}$ ,  $E_{xz}$ ,  $E_{yz}$ ) for sample A (left) and Sample B (right) ( $n = 3$ ; bars = S.D.)..... 70

Figure 3.9. Gaussian filtered FIDVC displacement components at 3 representative positions (indicated by different colors) in sample B, including their corresponding polynomial fit. Negative z-displacements are in the direction of the applied load..... 73

Figure 4.1. Schematic of mechanical resting set-up. **A.** Dissecting microscope and mechanical testing assembly **B.** FemtoTools micromanipulator and spring assembly. **C.** The microforce sensor has a custom probe that connects the micromanipulator to the spring, enabling the samples to remain hydrated in PBS. Samples are glued onto frames and loaded onto the spring. SolidWorks model of sample before **D** and during **E** tensile testing..... 78

Figure 4.2. Strain calculations. **A.** A FIJI macro is used to manually trace the fiducial lines from frames of the recorded videos, and the X and Y coordinates of each manually drawn line is returned ( $b$ =bone insertion attached to the fixed end,  $m$ =muscle insertion attached to the movable end of the system). **B.** A MATLAB algorithm is used to measure the average horizontal distance between fiducial lines for each selected frame. Strain is calculated relative to the initial distance between fiducial lines..... 80

Figure 4.3. Experimental methods shown with an E16.5 embryo and tendon. **A.** Tendons were removed excised from hindlimb by first removing the skin and exposing the tibialis anterior (muscle-tendon-bone unit; TA) and the extensor digitorum longus (EDL). Then the TA was carefully dissected using fine tweezers and an 11-blade to separate the surrounding connective tissue. In order to minimize damage to the tendon ( $t$ ) during decellularization, staining, handling, as well as to attach them to the 3D printed spring part during mechanical testing, TAs were glued onto PET frames using Loctite (L) from the muscle ( $m$ ) and the bone ( $b$ ) insertions (bars = 1mm). **B.** Z-projection of z-stack (Zeiss 800 WGA, 488, 10x) showing how the cross-sectional area of E16.5 tendon was obtained using orthogonal views (bar = 200  $\mu\text{m}$ ). **C.** Macroscopic imaging of E16.5 decellularized TA during tensile testing showing the muscle ( $m$ ) and bone ( $b$ ) insertions and the regions investigated..... 81

Figure 4.4. Mechanical contribution of three different 3D printed springs (SP9 is later referred as spring 1; SP10 is later referred to as spring 2)..... 85

Figure 4.5. Baseline adjustment (A) and testing modalities (B-D). **A.** Fibrin gel raw data, baseline, and baseline-adjusted fibrin gel. **B.** Force-displacement curves of Solaris, E16.5 TA, and fibrin gel. **C.** Stress relaxation test for E16.5 TA. **D.** Cyclic loading and tensile loading to failure for FN matrix. .... 86

Figure 4.6. Comparison of FemtoTools system to bulk material testing. **A.** Representative stress - strain curves of Solaris samples tested. **B.** Comparison of the tangent moduli of Solaris tested two spring configurations in the FemtoTools system (blue, magenta) and with bulk material testing instrument (black) (FemtoTools + spring 1 (n=5), FemtoTools + spring 2 (n=5), bulk material (n=5); error bars = std. dev.; \*\*\* $p < 0.0002$ , \*\*\*\* $p < 0.0001$ ). .... 87

Figure 4.7. Comparison of actuator strain (solid lines) and optical strain (dashed lines) for representative E16.5 and E18.5 tendons and fibronectin. Actuator strain is based on the imposed displacement and the initial sample length. Optical strain is calculated from the change in distance between photobleached lines. .... 88

Figure 4.8. Mechanical behavior of decellularized embryonic tendons. **A.** Calculated stress – strain curves for E16.5 (purple) and E18.5 (blue) samples, along with their fitted polynomial. **B.** Sidak multiple comparisons showed significant differences in the tangent modulus between E16.5 and E18.5 tendons (\* $0.0021 < p \leq 0.0332$ ; \*\* $0.0002 < p \leq 0.0021$ , \*\*\* $0.0002 < p \leq 0.0001$ , \*\*\*\* $p < 0.0001$ ; n = 3; bars = S.D.). .... 89

Figure 4.9. **A.** Regional stress - strain curves of decellularized E16.5 TA. **B.** Tukey multiple comparisons showed significant differences in the tangent modulus between individual groups (\* $0.0021 < p \leq 0.032$ ; \*\* $0.0002 < p \leq 0.0021$ , \*\*\* $0.0002 < p \leq 0.0001$ , \*\*\*\* $p < 0.0001$ ; n = 3; bars = S.D.)..... 90

Figure 4.10. Stress - strain curves show regional mechanical variations and an increase in tangent moduli as a function of development when comparing E18.5 (green) and P0 (blue). .... 91

Figure 5.1. Harvesting P3 tendons. **a.** Location of tibialis anterior (TA) in the P3 hindlimb showing the muscle (m) – tendon (t) – bone (b) units before and **b.** after dissection. **c.** Freshly harvested units fixed to clear vinyl frames and after decellularization using 0.05% SDS in PBS. .... 100

Figure 5.2. **a.** Representative 3D confocal rendering of TA immunostained to visualize ECM networks at 10x (bar=100  $\mu\text{m}$ ). **b.** IHC shows independent ECM networks with distinct fibril 3D organization in the developing tendon at 10 $\times$  (bar=50  $\mu\text{m}$ ). .... 101

Figure 5.3. **a.** Custom micromanipulator-based set- up to image network deformation for an inverted confocal microscope with a representative PET frame-TA sample (dashed box). Schematic shows the location of the bone (fixed end) and muscle insertions (movable end) on the PET frame. **b.** Visualization of fibrin gel deformation. AF488-labeled fibrin cast between porous PE anchors was axially loaded on micromanipulator-based set-up and imaged at 10 $\times$  with an inverted confocal (bar=200 $\mu\text{m}$ ). .... 102

Figure 5.4. Preliminary experiments allowed the visualization of different ECM networks under tension. Z-stacks acquired at 10 $\times$ . .... 103

Figure 5.5. **a.**E16.5 Decellularized TA imaged with a 10×W objective after stretching the tissue with micromanipulator translating stage. **b.** Composites show an overlay of the reference (blue) and deformed (magenta) networks of type I collagen, fibronectin, and WGA. **c.** Resulting displacement fields from relating the references and uniaxially loaded configurations using FIDVC. .... 105

Figure 5.6. **a.** Representative confocal images for E16.5 tendons visualizing ColI, FBN2, FN, and WGA during 2 loading cycles using a customized translating stage and an inverted confocal. Z-stacks were acquired at 10×. **b.** Image processing for the calculation of engineering strain using FIJI and MATLAB based on photobleached lines. .... 106

Figure 5.7. Adapting FemtoTools micro-robotic system to Zeiss 800 upright confocal for the visualization of immunostained ECM networks. **a.** A platform was machined to match the height of the microscope stage. **b.** The 3D printed spring is the same size as a 60 mm Petri dish, fitting well on the microscope stage. **c.** Sensor-3D printed spring interface and pillar do not interfere with objective. .... 107

Figure 5.8. Calculated prescribed (**a**) and residual (**b**) strain over 2 loading cycles corresponding to ECM protein networks for different locations along tendons averaged across biological replicates (n=3; bars = S.D; (\*0.0021 < p ≤ 0.0332; \*\*0.0002 < p ≤ 0.0021, \*\*\*0.0002 < p ≤ 0.0001) and a representative overlay of ColI and FBN2 before, during (**a**) or after (**b**) load. .... 109

Figure 5.9. Force – time curve recorded during 2 cycles of uniaxial loading of a decellularized E16.5 TA tendon immunostained to visualize FBN2 during testing. **b.** FBN2 networks in the reference (blue) and deformed (magenta) configurations for cycles 1 & 2 (bar =100 μm). ..... 110

Figure 5.10. TEM image analysis and type I collagen fibril diameter results in P3 tendons. **a.** Representative type I collagen fibrils acquired at 68,000× (bar=100 nm). **b.** Binarization of the image in (a) using thresholding in FIJI. **c.** Ellipses fitted to the fibrils in (a) to quantify fibril diameter. **d.** Distribution of fibril diameter for each sample across technical replicates (n=3; bars=S.D). **e.** Overview of fibril bundles acquired at 6,800× (bar = 1μm). .... 112

Figure 5.11. Ultrastructure of E18.5 tendons. **a.** Overview acquired at 2,550× (bar=5μm). **b.** Fibril bundles imaged at 9,900× (bar=1μm). **c.** Representative type I collagen fibrils acquired at 68,000× for diameter quantification (bar=200 nm). **d.** Distribution of fibril diameter for each sample across technical replicates (n=3; bar=S.D.). .... 114

Figure 5.12. Confocal imaging of ECM networks in P3 tendons after decellularization by gentle rocking in a 0.05% and 1× PI solution for 7 days. Images acquired at 10×W. .... 116

Figure A.1. SolidWorks assembly and finite element model simulations (mesh element size: 125 μm). **A.** Fixtures for **B** and **C** – fixed geometry (green), roller/slider (blue); and external load of 400 μN (pink). **D.** Fixtures for **E** and **F** – fixed geometry (green), and external load of 400 μN (pink). **B, E.** Displacement results from simulations ran using the elastic modulus for M2R-CL polymer provided by the manufacturer. Material properties – Young's modulus: 1750 MPa, shear modulus: 625 MPa, Poisson's ratio: 0.4, yield strength: 3.5 MPa, mass density: 1160 kg/m<sup>3</sup>, tensile Strength: 40 MPa. **C, F.** Displacement results from simulations ran using the elastic modulus obtained from empirical force-displacement data to calculate the stiffness of the M2R-CL 3D-printed spring. Material properties – Young's modulus: 20 MPa, shear modulus: 7.2 MPa, Poisson's ratio: 0.4, yield strength: 0.04 MPa, mass density: 1160 kg/m<sup>3</sup>, tensile strength: 40MPa. ....121

Figure B.1. Preliminary proteomic analysis of E14.5 control and decellularized skin showed a significant decrease in the relative amounts of ECM proteins, when comparing the label-free quantification (LFQ) intensity. GraphPad Prism was used to perform an unpaired t-test for protein control and decellularized group (n=3; bars=S.D.; \*0.0021 < p ≤ 0.0332; \*\*0.0002 < p ≤ 0.0021, \*\*\*0.0002 < p ≤ 0.0001, \*\*\*\* p<0.0001). .....122

Figure B.2. Decellularization of postnatal (P3) tendons with different treatments. **a.** Representative confocal images of treated tendons after immunostaining showing WGA (green), fibrillin-2 (white), and DAPI (blue). All images were acquired at 10×. **b.** Dissecting microscope images of control (freshly harvested) and treated tendons showing an increase in tissue transparency. .... 123

## LIST OF ABBREVIATIONS

**ECM:** extracellular matrix  
**E:** embryonic day (*e.g.* embryonic day 11.5, E11.5)  
**P:** postnatal day  
**3D:** three-dimensional  
**FBN2:** fibrillin-2  
**FN:** fibronectin  
**ELN:** elastin  
**WGA:** wheat germ agglutinin  
**col VI:** type VI collagen  
**LCT:** loose connective tissue  
**SDS:** sodium dodecyl sulfate  
**PI:** protease inhibitors  
**DVC:** digital volume correlation  
**FIDVC:** fast iterative digital volume correlation  
**E<sub>1</sub>:** maximum principal strain  
**TA:** tibialis anterior  
**TEM:** transmission electron microscopy  
**PDMS:** polydimethylsiloxane  
**PET:** polyethylene terephthalate

## ABSTRACT

The extracellular matrix (ECM) plays a significant role in defining the mechanical properties of biological tissues. The proteins, proteoglycans, and glycosaminoglycans that constitute the ECM are arranged into highly organized structures (*e.g.* fibrils and networks). Cellular behavior is affected by the stiffness of the microenvironment and influenced by the composition and organization of the ECM. Mechanosensing of ECM stiffness by cells occurs at the fibrillar (mesoscale) level between the single molecule (microscale) and the bulk tissue (macroscale) levels. However, the mechanical behavior of ECM proteins at the mesoscale are not well defined. Thus, better understanding of the ECM building blocks responsible for functional tissue assembly is critical in order to recapitulate *in vivo* conditions. There is a need for the mechanical characterization of the ECM networks formed by proteins synthesized *in vivo* while in their native configuration.

To address this gap, my goals highlighted in this dissertation were to develop appropriate experimental and computational methodologies and investigate the 3D organization and mechanical behavior of ECM networks *in situ*. The ECM of developing mouse tissues was used as a model system, taking advantage of the low-density networks present at this stage. First, we established a novel decellularization technique that enhanced the visualization of ECM networks in soft embryonic tissues. Based on this technique, we then quantified tissue-dependent strain of immunostained ECM networks *in situ*. Next, we developed mesoscale and macroscale testing systems to evaluate ECM networks under tension. Our systems were used to investigate tendon mechanics as a function of development, calculating tangent moduli from stress - strain plots. Similarly, we characterized ECM network deformation while uniaxially loading embryonic tissues, since this testing modality is ideal for fibril and network mechanics. Taken together, this information can facilitate the fabrication of physiologically relevant scaffolds for regenerative medicine by establishing mechanical guidelines for microenvironments facilitate functional tissue assembly.

# 1. INTRODUCTION

## 1.1 Background

### 1.1.1 The extracellular matrix and its role in biological tissues

The extracellular matrix (ECM) is an intricate network of proteins, proteoglycans, glycosaminoglycans, and other macromolecules that surrounds cells in biological tissues. Several main functions include providing structural integrity to tissues and regulating cellular behavior through biomechanical and biochemical cues during tissue morphogenesis, growth, repair, regeneration, and homeostasis<sup>1,2</sup>. Specifically, the ECM affects cell behavior by defining the stiffness of the cellular microenvironment and activating intracellular signaling via binding with cell surface receptors<sup>3</sup>. Cells sense and respond to mechanical loads from physical and soluble signals and from cell-to-cell interactions. Through a regulatory feedback mechanism between cells and the ECM, cells are able to adapt to their environment and adjust their behavior and gene expression according to the rigidity and composition of the ECM<sup>1,4-6</sup>. Of particular interest is mechanotransduction, or cells sensing and responding to mechanical stimuli by converting them to biochemical signals. The ECM- integrin ( $\alpha\beta$ )- cytoskeleton pathway is an important way mechanotransduction is transmitted (**Fig. 1.1**)<sup>7,8</sup>. Integrins physically connect the actin cytoskeleton to the ECM and transmit bidirectional (*i.e.* ECM-to-cell, cell-to-ECM) signals across the plasma membrane<sup>9,10</sup>. Altered mechanical stimuli can result in altered gene expression and cell properties; influencing cell processes such as differentiation, migration, and proliferation which consequently affect tissue formation, homeostasis, or regeneration<sup>8,11</sup>.

The local ECM composition and architecture depend on the biomechanical requirements of the tissue of interest, as well as the state (*e.g.* healthy, injured) the tissue is in. For instance, during embryogenesis, the ECM provides structural support and mechanical cues to direct global tissue movement and organization<sup>12</sup>. To this end, ECM proteins have both structural and biological roles when guiding cell behavior and consequently tissue function. However, the composition of the cellular microenvironment is known to influence its stiffness; therefore, the biochemical and mechanical functions of cellular microenvironments are closely intertwined *in vivo*<sup>13</sup>. Fibrillar proteins (*e.g.* type I collagen, elastin) provide tissues strength in tension, while space-filling molecules (*e.g.* hyaluronic acid, aggrecan) provide compressive resistance by creating a hydrated

environment<sup>14</sup>. Other ECM proteins such as fibronectin, tenascin-C, laminins and type VI collagen link different macromolecules together and orchestrate assembly<sup>15</sup>. The primary focus of this dissertation resides in proteins that arrange into multimeric organizations and organized 3D structures, such as fibrils and networks. Nevertheless, many other molecules, though lower in quantity, function as essential components of the ECM in soft tissues. For instance, decorin and fibril-associated collagens with interrupted triple helices do not form higher order structures, and instead indirectly regulate the stiffness and geometry of different parts of the ECM by mediating network assembly<sup>16,17</sup>. Other components of the extracellular space include growth factors, cytokines, and cell adhesion molecules. As a result, the ECM further actively participates in the establishment, separation, and maintenance of differentiated tissues by regulating the abundance of growth factors, receptors, the level of hydration, and the pH of the local environment<sup>2,4,6,18,19</sup>. Taken together, this indicates that the vast array of ECM proteins present in the cellular microenvironment is critical in guiding cellular behavior.

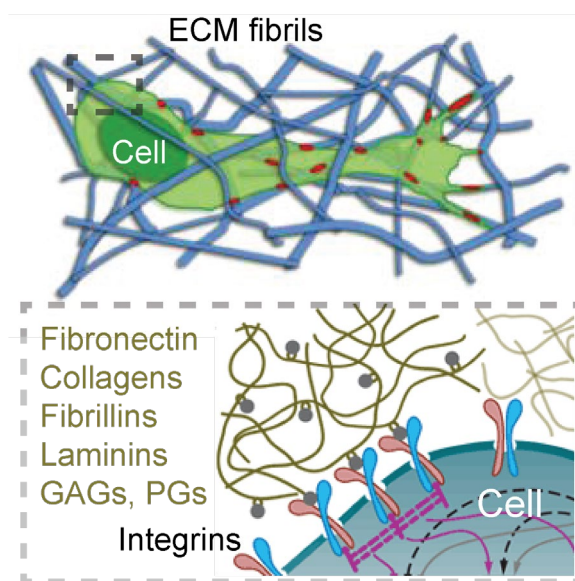


Figure 1.1. Schematic representation of cells sensing mechanical stimuli from ECM fibrils in their surroundings via the ECM- integrin ( $\alpha\beta$ )- cytoskeleton path. Adapted from Doyle and Yamada and Lutolf and Hubbell.

### 1.1.2 Fibril and Network Forming ECM Molecules

Fibril and network-forming proteins, such as collagens I, II and III, elastin (ELN), fibrillins, and fibronectin, are deposited by cells or recruited from the circulating plasma to help remodel an

existing network. Fibrillar ECM are abundant in tendons, ligaments, and cartilage and facilitate the effective transmission and absorption of cyclical forces while avoiding tissue injury through distinct structural and biomechanical properties<sup>2,20,21</sup>. The primary role of fibril-forming collagens is to provide mechanical strength to tissues, particularly type I collagen. Collagen subunits ( $\alpha$ -chains) assemble as homotrimers or heterotrimers to form triple-helical molecules, conferring considerable structural strength<sup>2,22</sup>. Triple-helical type I collagen units form fibrils that can then bundle together to form thick fibers with a given orientation and organization<sup>23,24</sup>. Fibril diameter varies depending on the stage of development, ranging from 12 nm to 500 nm<sup>25</sup>. For instance, in tendons, type I collagen comprises ~95% of the matrix in the adult and is aligned in the direction of loading, or the long axis of the tendon<sup>26</sup>. The hierarchical assembly of collagens in tendon, or fibrillogenesis, enables its organization, showing the important relationship between the three-dimensional protein structure and the function of the resultant ECM<sup>22,27</sup>. Fibers then group into primary fiber bundles or fascicles before gathering to form tertiary fiber bundles (**Fig. 1.2**)<sup>17</sup>.

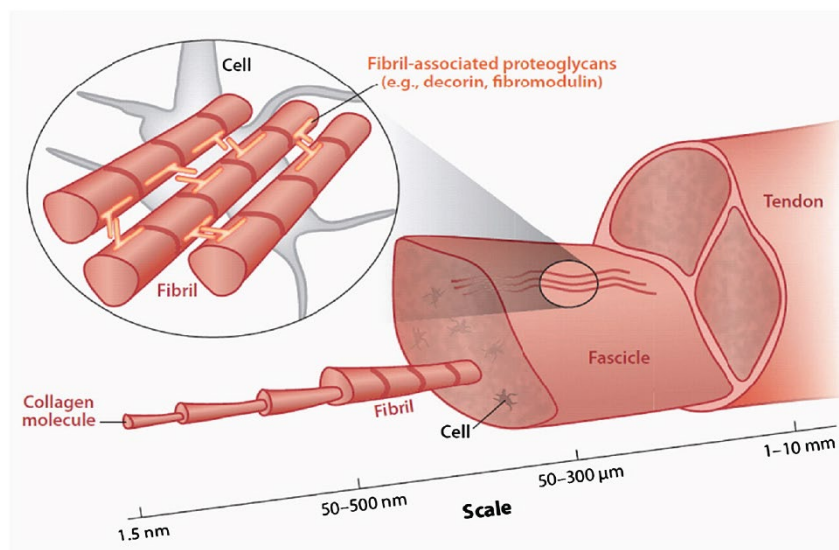


Figure 1.2. Hierarchical structure of tendon from the single type I collagen molecule up to fibrils, fascicles, and whole tendon, including the ECM fibrils at the mesoscale (50 nm – 300 μm), and describing the structure of fibril-associated proteoglycans (from Connizzo *et al.*).

Similar to collagens, the glycoproteins fibrillin-1 and fibrillin-2 (FBN2) also arrange to form fibrils and networks, yet these have very different biomechanical and biochemical functions. Their biomechanical roles relate to the temporal and hierarchical assembly of elastic fibers and microfibrils, serving as a structural template for tropoelastin deposition during elastic fiber

formation<sup>28,29</sup>. Moreover, they provide critical mechanical anchoring in dynamic connective tissues and are found in locations under repeated mechanical stress. Their biological significance is further emphasized by their relation to connective tissue disorders<sup>30</sup>. Mutations in the fibrillin-1 gene are closely associated with Marfan syndrome<sup>31</sup>. In contrast, the biochemical roles are dependent on the ability of fibrillins to sequester transforming growth factors  $\beta$  and bone morphogenetic proteins in the ECM, which can regulate a myriad of cellular activities. Fibrillins are able to self-polymerize into filamentous microfibrils with an average diameter of  $\sim 10$  nm<sup>28</sup>. Microfibrils and elastic fibers are polymeric structures that organize according to the mechanical demands of specific tissues, such as the strength and direction of forces<sup>29,32</sup>. For instance, they form a loosely organized network in the skin to confer its pliability, whereas in the eye, parallel bundles of microfibrils anchor the lens and adjust its thickness by conducting tension from the ciliary body, exemplifying that the ECM organization is tissue-specific<sup>29,33</sup>.

Fibronectin is another commonly studied fibril and network forming glycoprotein given its widespread presence in soft tissues and critical roles. Fibronectin molecules assemble into fibers that range in diameter from 10 nm to micrometers in size, with lengths of micrometers<sup>25,34</sup>. Cells can arrange soluble fibronectin into fibers or, alternatively, secrete their own. Both mechanical and biochemical factors can induce fibronectin expression<sup>34-36</sup>. Once assembled, the fibronectin matrix impacts tissue organization by affecting the assembly of other ECM proteins. For example, fibronectin is essential to the process of collagen matrix deposition<sup>37</sup>. It also functions as a lubricant for shear, as a medium for force transmission, and can simultaneously interact with other fibronectin molecules, ECM proteins, and cell surface receptors<sup>27,38,39</sup>. By facilitating interactions with other ECM proteins, cell signaling, and sequestering and releasing molecules that affect the overall tissue organization, fibronectin influences the mechanical behavior of the microenvironment<sup>40,41</sup>. Fibronectin is of particular importance in wound healing and embryogenesis; thus, characterizing its behavior and organization while in biological tissues is critical in further understanding of these processes<sup>37</sup>.

### **1.1.3 ECM organization and mechanics**

As previous sections explained, both ECM composition and 3D organization are critical for proper cell behavior and tissue function, contributing to the intricacy of the cellular microenvironment. Cells not only detect the composition and stiffness of the ECM but are also

influenced by its architecture, which is both tissue-specific and heterogeneous<sup>42</sup>. The complexity of the cellular microenvironment is tied to the myriad of biological needs it supports in tissues through their structural and biochemical properties<sup>2</sup>. The 3D architecture of specific ECM proteins depends on their primary function in a given tissue. For example, FBN2 and type I collagen are organized differently when found in developing skin versus developing tendon (**Fig. 1.3**). Both type I collagen and FBN2 fibers are highly aligned in the direction of load in tendon; while in skin they form a network arranged to handle biaxial loading. Additionally, the microenvironment is highly dynamic during tissue formation, both during embryonic development and healing and regeneration. For instance, proteomic analysis of developing murine cartilage reveals significant changes in composition as a function of development and an increase in ECM-related proteins between embryonic and postnatal timepoints<sup>43</sup>. Significant changes in ECM composition likely impact the mechanics of this system. Similarly, in the study of cardiac development, Hanson *et al.*, quantified significant differences in ECM composition depending on both location along the murine left ventricle and the developmental timepoint from fluorescent antibody-labeled sections of embryonic and postnatal tissues. As sophisticated mass spectrometry and metabolic labeling techniques are developed, the dynamics of the ECM and changes according to the critical processes of any given developmental stage increase in understanding<sup>44</sup>. These studies highlight the importance of ECM composition and spatial distribution for proper tissue formation.

Based on the instructive power of the ECM, through the regulation of signaling and cell differentiation, researchers and tissue engineers seek to recapitulate native microenvironments to fabricate physiologically relevant tissues<sup>2,45,46</sup>. Tissue engineering strives to replicate functional tissues in order to replace those damaged or lost, oftentimes through a supportive scaffold that serves as a guiding structure for the deposition and remodeling of the ECM *in vivo* and leads to the desired cell-ECM interactions needed for functionality and mechanical integrity<sup>41,47</sup>. Accordingly, the development of physiologically relevant scaffolds based on naturally derived polymeric materials requires the ability to understand the ECM cells receive instructive signaling from. Furthermore, recapitulating cellular differentiation for tissue morphogenesis and physiological remodeling needs an understanding of the ECM components that are produced by cells and how they assemble into a functional 3D structure<sup>4,6</sup>. ECM proteins in this 3D structure interact with cells while in a fibrillar or network state; in other words, mechanosensing of ECM stiffness by cells occurs at the fibrillar and network level. Therefore, the stiffness of the

cellular microenvironment is conferred at this scale (*i.e.* in the order of micrometers) between the single protein (*i.e.* nanometers) and the bulk tissue scales (*i.e.* millimeters and centimeters), or mesoscale (**Fig. 1.4**). One reason there is a large gap in what is known at the mesoscale is the insolubility of ECM networks, which precludes the extraction of fibrils for mechanical testing. Therefore, better understanding of the ECM building blocks responsible for functional tissue assembly is needed in order to engineer scaffolds that closely mimic *in vivo* conditions.

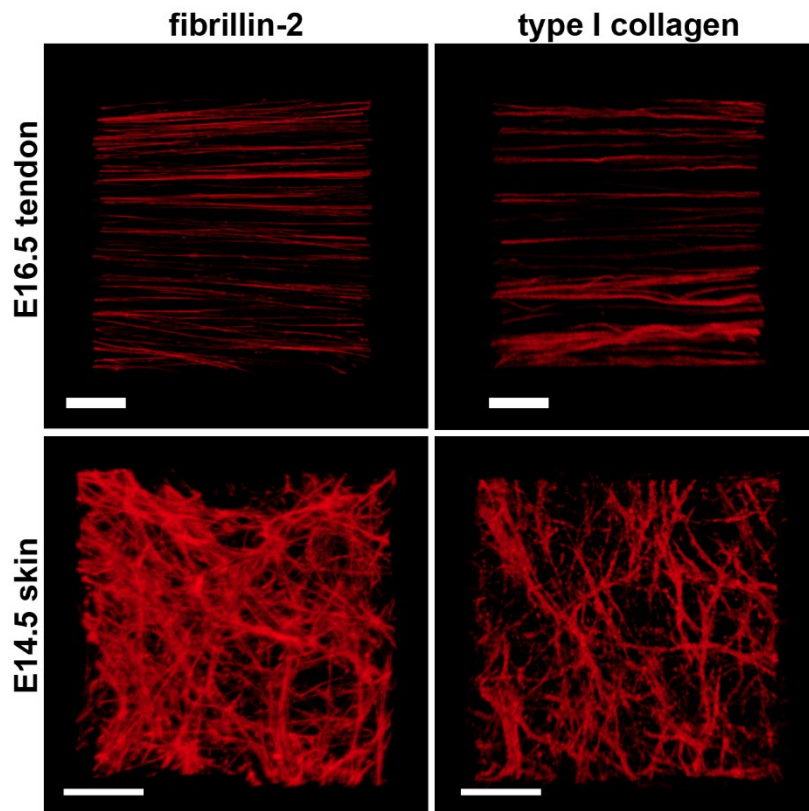


Figure 1.3. Comparison of network organization of type I collagen and fibrillin-2 between embryonic tendon and skin. Images of these decellularized tissues were acquired at 20 $\times$  and then processed and 3D reconstructed using FIJI 3D Viewer (bars=20  $\mu$ m).

Researchers have thus capitalized on the modular nature of the ECM macromolecules and their ability to self-assemble into networks to generate ECM-based hydrogels *in vitro*. Hydrogels have been widely used to investigate the relationship between cells and the material properties of their microenvironment and decipher how cues from the ECM regulate intracellular mechanisms that direct specific behaviors. Hydrogels are powerful tools that have been utilized to investigate, for instance, the host response to biomaterials and myoblast behavior<sup>48,49</sup>. However, without the

endogenous cells and other molecules in the intricate extracellular microenvironment to orchestrate proper assembly, it is unlikely that these networks have the same material properties or configuration as those synthesized *in vivo*. Mimicking the cellular and tissue complexity found *in vivo* by incorporating physical, chemical, temporal, and spatial gradients within engineered 3D scaffolds is therefore challenging, yet necessary for the fabrication of functional tissues.

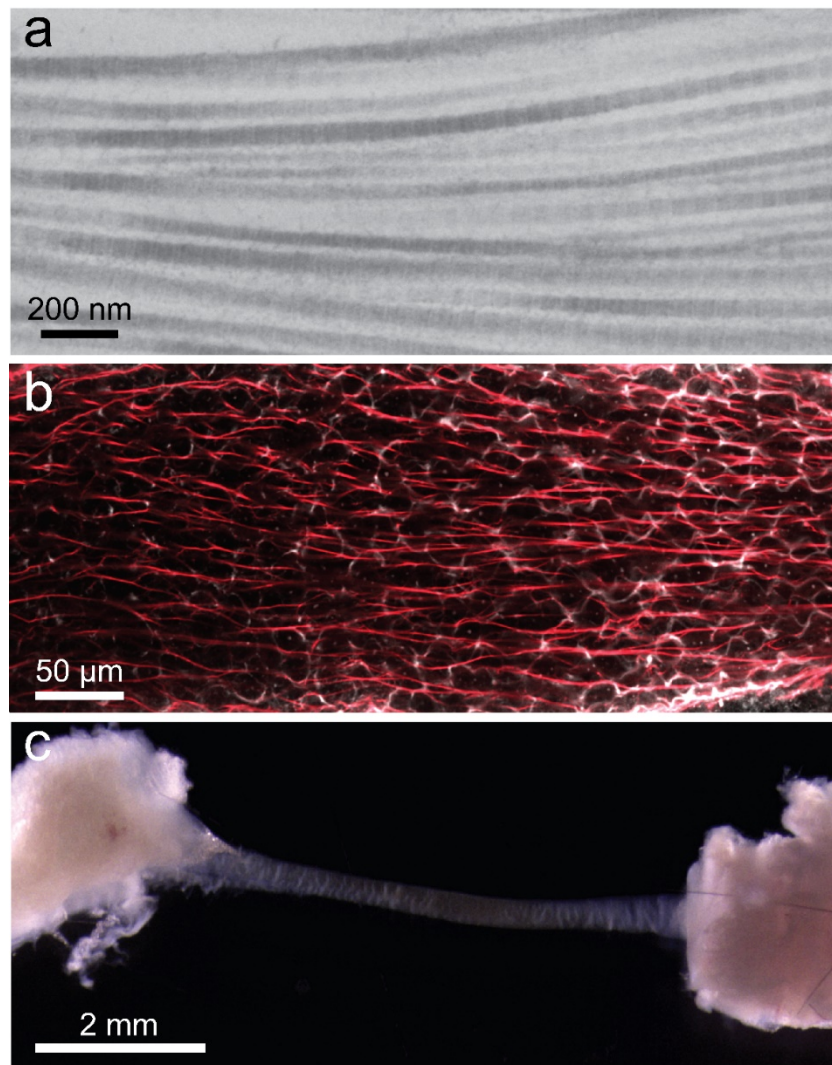


Figure 1.4. Visual representation of the mesoscale (**b**) between the single fibril (**a**) and the bulk tissue scales (**c**). **a**. Transmission electron microscopy image of a postnatal murine tendon showing collagen fibrils along the short axis acquired at 18,500 $\times$ . **b**. Fibrillin-2 (white) and fibronectin (red) networks in an embryonic decellularized murine tendon acquired at 20 $\times$ . **c**. Adult murine tibialis anterior tendon shown with respective bone and muscle insertions, imaged with a dissecting scope at 0.75 $\times$ .

#### 1.1.4 Approaches to characterize ECM mesoscale mechanics

##### *In vitro and in silico models*

To bypass a number of limitations related to the study of ECM mesoscale mechanics, researchers have used both *in vitro* and *in silico* models. It is challenging to study the mechanics in a complex *in vivo* environment, with a vast number of variables and confounding chemical and physical factors<sup>50</sup>. It is also difficult to isolate ECM networks without disrupting their native conformation. Therefore, a common approach that researchers take is to test the mesoscale mechanics of single types of ECM assembled *in vitro*, such as collagen and fibrin<sup>51</sup>. Characterization of viscoelastic properties of fibrin has provided insight into network stress-stiffening as a response to the presence of cells<sup>52</sup>. *In vitro* 2D and 3D models provide highly controlled culture environments to study the effects of specific cues in isolation<sup>50,53</sup>. Type I collagen has been thoroughly researched and often used to create reconstituted collagen gels since it can provide scaffolds with structural integrity<sup>54</sup>. A single collagen molecule is formed by left-handed alpha peptide strands coming together to form a right handed triple helix. A type I collagen fibril presents strain stiffening behavior, and its strain response is separated into the toe, the heel, and the linear regions, similar to the stress-strain response of mature tendons<sup>54,55</sup>.

Recent studies have reported discrepancies in the single molecule persistence length, a measure of the stiffness of a polymer, depending on the technique and the environment collagen is tested in. Similarly, at the network scale, studies have shown that the persistence length of *in vitro* networks depends on how fibrils are reconstituted<sup>54</sup>. This variability related to *in vitro* generated networks is disadvantageous when seeking to characterize the ECM network mechanics. Type I collagen fibril assembly is mediated by accessory molecules (*e.g.* decorin, types III & V collagen) that are challenging to fully recapitulate *in vitro*<sup>56,57</sup>. Additionally, sophisticated *in vitro* experiments combining fibril forming collagens and proteoglycan demonstrated how network assembly and mechanics are significantly dependent on other ECM molecules<sup>58,59</sup>. Without cells and accessory ECM molecules to orchestrate proper assembly, networks synthesized *in vitro* will not have the same organization and material properties as those deposited *in vivo*. Therefore, these studies do not fully capture the behavior of proteins as they would be synthesized *in vivo*.

Similarly, *in silico* studies that describe the mechanics of ECM networks are important tools for tissue engineering because they help predict microstructure-mechanical relationships and create a framework for understanding cell-ECM interactions. Networks based on experimental

data and imaging information are used to refine dimensions and calculate networks volume fractions. In a study by Susilo *et al.*, collagen fibrils were represented as incompressible hyperelastic neo-Hookean solids. The fibril intersections were assumed to be frictionless pin joints in order to form a network<sup>60</sup>. This work provides insight on the interactions between fibrils when forming networks, stating that the presence of fibril intersections where the fibrils can slide during stretching, instead of assuming a pin joint, plays a role in the non-linearity of the stress-stretch curve collagen matrices exhibit during biaxial loading. Some models incorporate the interactions between networks such as the work presented by Lake *et al.*<sup>61</sup>, including agarose and type I collagen networks in order to investigate the interactions between fibrillar and non-fibrillar matrices. However, analysis of single fibrils will not provide information regarding the mechanics of the entire network, without involving a number of assumptions. While models attempt to account for the 3D heterogeneity of networks, the interaction between them, and fiber realignment by using the volume-averaging theory<sup>62</sup>. *In silico* models oftentimes are based off a representative element based on assumptions, such as a homogenous matrix that perhaps does not represent the heterogeneity of an ECM protein<sup>63</sup>.

### ***In situ ECM mechanics at the mesoscale***

Although significant efforts have been made to quantify the mechanics of ECM networks generated *in vitro*, little is known about the mechanical properties of the native ECM networks (*i.e.* networks synthesized *in vivo*) that these hydrogels seek to emulate. The mechanical environment of the cells is regulated at the network or mesoscale levels (**Figs. 1.1, 1.4**). Mechanical testing of the ECM at this scale is challenging due to the difficulty in extracting these relatively insoluble networks in their native conformation from dense connective tissues. Methods to isolate intact type I collagen and fibrillin fibrils have been developed; however, to constrain these fibrils for mechanical tests, the samples are typically dried on a substrate and rehydrated. This alteration in the hydration state can significantly affect the mechanical response of biological materials<sup>64</sup>. Furthermore, the boundary conditions of the tissues are disrupted, and the fibril is not tested in the native network configuration. A critical component for characterizing the mechanics of the ECM at the mesoscale is to be able to reliably measure strain across large networks, given the heterogeneity of strain fields and the 3D organization and distribution of ECM proteins.

To measure strain across large ECM networks, we must be able to visualize them. Visualization of ECM architecture in its native conformation is hindered by the composite nature of intact tissues. Resident cells induce light scattering, which prevents visualization of networks beyond the superficial surface layers, making it challenging for high resolution imaging within opaque biological tissues<sup>65</sup>. Optical clearing is a powerful approach that enhances the ability to resolve 3D tissue architecture by either reducing the amount and diversity of light scattering elements (*e.g.* lipids) or minimizing refractive index mismatches<sup>66</sup>. Optical clearing-based approaches have improved the visualization of ECM proteins such as type IV collagen in the rat brain<sup>67</sup> and proteoglycans in bovine musculoskeletal tissues<sup>68</sup>. Hydrogel-based clearing techniques have been developed to address the issue of protein loss when using harsh solvents or detergents to remove light scattering biomolecules by first embedding the issue in hydrogel<sup>65</sup>. Decellularization using mild detergents can remove cellular interference; however, most adult tissues are dense and individual networks remain difficult to resolve. Furthermore, not all solvent-based clearing reagents are compatible with immunostaining, and for those techniques that are, tissue penetration and fluorescent signal attenuation are of concern<sup>65,69,70</sup>.

Some researchers bypass the need for immunostaining to visualize ECM networks by using nonlinear optical microscopy techniques. Keyes *et al.* developed an optomechanical device coupled with two-photon microscopy to look at collagen and ELN during biaxial testing of the left coronary artery<sup>71</sup>. Collagen is recorded from second harmonic generation and ELN from fluorescence emission, which is useful in the study of vascular mechanics and when tissue engineering vascular grafts. Coupling uniaxial or biaxial loading systems to microscopy systems has often focused on characterizing the tissue mechanics and exploring their relationship to the network microstructure (*i.e.* fiber orientation) and not on the mechanics of the networks themselves<sup>71,72</sup>. Another recent study by used multiphoton and confocal microscopes to look at collagen and cell nuclei and investigate the effects of tendon healing in multiscale mechanical structure and compositional response<sup>73</sup>. The mechanical characterization of the tendons was performed using atomic force microscopy-based nano-micro indentation. Coupling of mechanical and imaging system allowed them to identify correlations between nuclei and collagen disorganization and capture collagen structure through healing<sup>74</sup>. *In situ* studies oftentimes only look at one protein and make assumptions of the ECM content in the tissue of interest.

## 1.2 Thesis overview: characterizing extracellular matrix networks *in situ*

ECM 3D organization and composition are specific to the mechanical needs of each tissue and come together through an interplay between cells and their microenvironment. The mechanical characterization of tissues along multiple scales has helped elucidate how the microstructure and ultrastructure respond to mechanical stresses<sup>74</sup>. While significant efforts have been made in understanding the role of the ECM in disease progression and tissue formation, there remains an opportunity to explore the 3D organization and material behavior of these networks in their native conformation or *in situ*. The mechanical behavior of ECM proteins at the network mesoscale, are not well defined. It is evident that this characterization poses a variety of challenges, some of them stemming from the limitations of current methodologies from both a biological and engineering standpoint. The goals of this dissertation are to first develop appropriate experimental and computational methodologies, and then investigate the 3D organization and mechanical behavior of ECM networks *in situ* in order to establish guidelines for microenvironments that facilitate tissue assembly. The ECM of developing murine tissues are used as a model system for the study of the mechanics of networks as they are found *in vivo* (*i.e. in situ*). At this stage of development, networks are present at a lower density compared to the complex, mature adult environment that oftentimes hinders visualization. Given that the same networks are present in embryonic and adult tissues, we expect to be able to extrapolate these results and relate them back to the ECM of adult, healthy tissues. The overarching goals of this work can be broken up into the following 4 chapters.

The first step in the characterization of ECM networks *in situ* is the ability to visualize them. In **Chapter 2**, we describe a novel decellularization technique to visualize the 3D organization of the ECM using a polyacrylamide-based hydrogel to provide a 3D framework within developing murine embryos. Immunostaining and confocal microscopy were used to visualize the 3D distribution of independent ECM networks in multiple developing tissues, including the forelimb, eye, and spinal cord. We demonstrate this method can be a powerful tool in defining the spatiotemporal distribution of the ECM during musculoskeletal assembly and embryogenesis. Using this novel decellularization method to enhance the visualization of the ECM, we then quantify tissue-dependent strain of immunostained ECM networks *in situ* in **Chapter 3**. We establish a method to quantify ECM network strain after the application of a known compressive load on murine embryonic forelimbs. Samples were imaged, before and after the

application of load and a MATLAB-based fast iterative digital volume correlation algorithm was used to quantify network displacements by comparing the reference and compressed z-stacks. This method allowed us to quantify 3D geometry-specific ECM deformation and strain and serves as proof-of-concept for the combination of confocal microscopy and digital volume correlation for the study of the ECM. While significant differences in ECM strain were resolved, compression is not the ideal testing modality for characterizing fibril and network mechanics given that physiologically a large percentage of ECM are loaded in tension.

To address the limitations of characterizing the ECM under compression, the focus of **Chapter 4** is the development of a mechanical testing system for tensile testing of small soft tissues by adapting a commercially available micro-robotic system that can record force and displacement measurements with the appropriate resolution. The modularity and adaptability of this system allow us to couple it with a dissecting microscope in order to visualize tissue deformation during mechanical testing and thus facilitating the calculation of optical strain. This system is able to resolve a variety of mechanical responses and accommodate for several biologically relevant geometries and stiffnesses. Lastly, our system was used to investigate tendon mechanics, showing an increase in tangent moduli as a function of development. Similarly, in **Chapter 5**, we investigate and characterize ECM networks while uniaxially loading decellularized tissues. Mechanical testing systems appropriate for developing murine tissues are engineered for the study of networks in tissues of homogenous ECM. Uniaxial loading is the ideal testing modality for fibril and network mechanics. The ideal tissue for tensile testing must not only be easily dissected and have the correct aspect ratio, but also allow for tissue-level deformation measurements. In addition, the tissue should have a relatively homogeneous ECM distribution and arrangement throughout. This will decouple the influence that geometry and material behavior have in strain. Homogeneous tissue geometry will facilitate the calculation of tissue stress. Methodologies and studies outlined in this chapter provide a powerful framework for the characterization of ECM networks. Further, the combination of micro and macroscale mechanical testing systems allows us to obtain the deformation and boundary conditions at the tissue-level, and the 3D architecture of the ECM networks as a function of the load applied to quantify ECM tensile strain. Lastly, in **Chapter 6** this work's contributions to science will be discussed as well as future directions. Taken together, this information can facilitate the fabrication of physiologically relevant scaffolds for regenerative

medicine by establishing mechanical guidelines for microenvironments that are used for functional tissue assembly.

## 2. THREE DIMENSIONAL VISUALIZATION OF EXTRACELLULAR MATRIX NETWORKS DURING MURINE DEVELOPMENT

As outlined in the thesis overview, the first step in the characterization of extracellular matrix networks is visualizing them while in their native conformation. To do so, we modified an established hydrogel-based method for the decellularization of small, highly cellular embryonic tissues. The hydrogel cross-links only to itself allowing for the removal of intracellular proteins while providing a 3D framework for the remaining insoluble ECM networks and hence avoid the disruption of tissue integrity. We discuss how this method enabled the investigation of the musculoskeletal system in the developing murine forelimb, particularly looking at the formation of cartilage, bone, and tendon. The content presented in this chapter is adapted from our work “Three-dimensional visualization of extracellular matrix networks during murine development”, which was published in *Developmental Biology*. Minor edits to the formatting have been made, such as including the supplemental data for the published article in this chapter, to produce a cohesive dissertation. The published version of this chapter is available at the following link: <https://doi.org/10.1016/j.ydbio.2017.12.022>.

### 2.1 Abstract

The ECM plays a crucial role in embryogenesis, serving both as a substrate to which cells attach and as an active regulator of cell behavior. However, little is known about the spatiotemporal expression patterns and 3D structure of ECM proteins during embryonic development. The lack of suitable methods to visualize the embryonic ECM is largely responsible for this gap, posing a major technical challenge for biologists and tissue engineers. Here, we describe a method of viewing the 3D organization of the ECM using a polyacrylamide-based hydrogel to provide a 3D framework within developing murine embryos. After removal of soluble proteins using sodium dodecyl sulfate, confocal microscopy was used to visualize the 3D distribution of independent ECM networks in multiple developing tissues, including the forelimb, eye, and spinal cord. Comparative analysis of E12.5 and E14.5 autopods revealed proteoglycan-rich fibrils maintain connections between the epidermis and the underlying tendon and cartilage, indicating a role for the ECM during musculoskeletal assembly and demonstrating that our method can be a powerful tool for defining the spatiotemporal distribution of the ECM during embryogenesis.

## 2.2 Introduction

The ECM is an intricate network of proteins, proteoglycans, glycosaminoglycans, and other macromolecules. It has several main functions, including providing structure to tissue and regulating cellular behavior during growth, repair, regeneration, and homeostasis<sup>1,2</sup>. During embryogenesis, the ECM provides structural support and mechanical cues to direct global tissue movement and organization<sup>75</sup>. Furthermore, the ECM locally controls cell behavior by defining the stiffness of the cellular microenvironment and activating intracellular signaling via binding with cell surface receptors<sup>3</sup>. In addition, the ECM is thought to play a key role in paracrine signaling vital to development through growth factor sequestration<sup>76,77</sup>. While it is generally accepted that ECM composition undergoes dramatic remodeling during tissue formation, leading to changes in tissue mechanics and cellular behavior, little is known about how the 3D organization of these ECM components varies as a function of development.

Visualization of the ECM in 3D has been hindered by the inherent difficulty of high resolution imaging within opaque biological tissues. Optical clearing is a powerful approach to enhance the ability to resolve 3D tissue architecture by either reducing the amount and diversity of light scattering elements (*e.g.* lipids) or minimizing refractive index mismatches<sup>65,66</sup>. Hydrogel-based clearing techniques have been developed to address the issue of protein loss when using harsh solvents or detergents to remove light scattering biomolecules by first embedding the issue in hydrogel<sup>65</sup>. The tissue is incubated in a monomeric solution followed by polymerization triggered by a thermal initiator<sup>78</sup>. As polymerization occurs, a hybrid network composed of proteins and the polymer chains of the hydrogel is created that allows for the removal of lipids and other light-scattering biomolecules.

Optical clearing methods based on solutions that match the refractive index of tissue are also becoming more prevalent<sup>66</sup>. One example, SeeDB, is a concentrated aqueous fructose solution with a refractive index close to that of fixed tissue ( $n \sim 1.49$ ) that greatly enhances the depth at which a variety of tissues can be imaged using confocal microscopy ranging from embryos to dense connective tissues<sup>68,79</sup>. However, not all solvent-based clearing reagents are compatible with immunostaining<sup>69</sup>, and for those techniques that are, tissue penetration and fluorescent signal attenuation are of concern<sup>65,70</sup>.

Previous optical clearing-based approaches have improved the visualization of ECM proteins such as type IV collagen in the rat brain<sup>67</sup> and proteoglycans in bovine musculoskeletal

tissues<sup>68,80</sup>. Nonetheless, most clearing techniques were designed to resolve cellular structures and there have been few efforts to visualize the organization of the ECM fibrils within intact tissues. To address this need, we developed a method to selectively remove intracellular proteins while leaving behind proteins of the ECM in the native 3D conformation. Typically, decellularization involves using detergents to extract cell membranes and other components<sup>81</sup>; however, most decellularization techniques are harsh to the sample and generally only applicable to ECM-rich tissues<sup>82,83</sup>. Softer, embryonic tissues are highly cellular and susceptible to damage<sup>84</sup>. Therefore, we modified established hydrogel-based clearing methods such that the hydrogel only cross-linked to itself, allowing for removal of soluble, intracellular proteins while providing a 3D framework for the remaining insoluble ECM networks<sup>78,85</sup>. Decellularization significantly enhanced the visualization of ECM proteins and maintained the 3D architecture of independent networks. Using confocal microscopy, we demonstrate that the ECM within intact E12.5 embryos can be visualized at multiple scales. Comparative analysis of the autopod of E12.5 and E14.5 forelimbs revealed continuous proteoglycan-rich fibrils extended between the epidermis and cartilage, which remained present after the formation of the extensor tendons. Overall, we expect our method will be a powerful tool for investigating how the ECM remodels during tissue assembly.

## **2.3 Materials and methods**

Unless otherwise specified, all reagents were of chemical grade from Sigma-Aldrich.

### **2.3.1 Embryo harvest**

Tissues from E11.5-E14.5 mice were generated by the timed matings of wild type C57Bl/6 mice. All murine experiments were approved by the Purdue Animal Care and Use Committee (PACUC; protocol 1209000723). PACUC ensures that all animal programs, procedures, and facilities at Purdue University adhere to the policies, recommendations, guidelines, and regulations of the USDA and the United States Public Health Service in accordance with the Animal Welfare Act and Purdue's Animal Welfare Assurance. Dams were euthanized via CO<sub>2</sub> inhalation, confirmed by cervical dislocation. Embryos were removed from the uterine horns and rinsed in 1× PBS. Dissection of the yolk sac and amnion was performed under magnification to avoid damaging the embryos.

### 2.3.2 Embryo decellularization

Murine embryos were decellularized and imaged as depicted in **Fig. 2.1**. After dissection of yolk sac and amnion, embryos were rinsed in 1× PBS, submerged in 1–1.5 mL hydrogel solution (**Table 2.1**) in a 2.0 mL microcentrifuge tube, and gently rocked overnight at 4 °C. Excess hydrogel solution was removed and embryos were immersed in mineral oil in a round bottom 14 mL round bottom polypropylene tube (Falcon 352059). Tubes were sealed with Parafilm before being placed in a 37 °C water bath for 5–6 h to polymerize the hydrogel. Embryos were removed from mineral oil and rinsed three times in 1× PBS to remove excess oil. Each embryo was gently rocked in 1 mL 0.05% SDS with 1× Halt™ protease inhibitor (PI, Thermo Scientific, 78430) in 1×

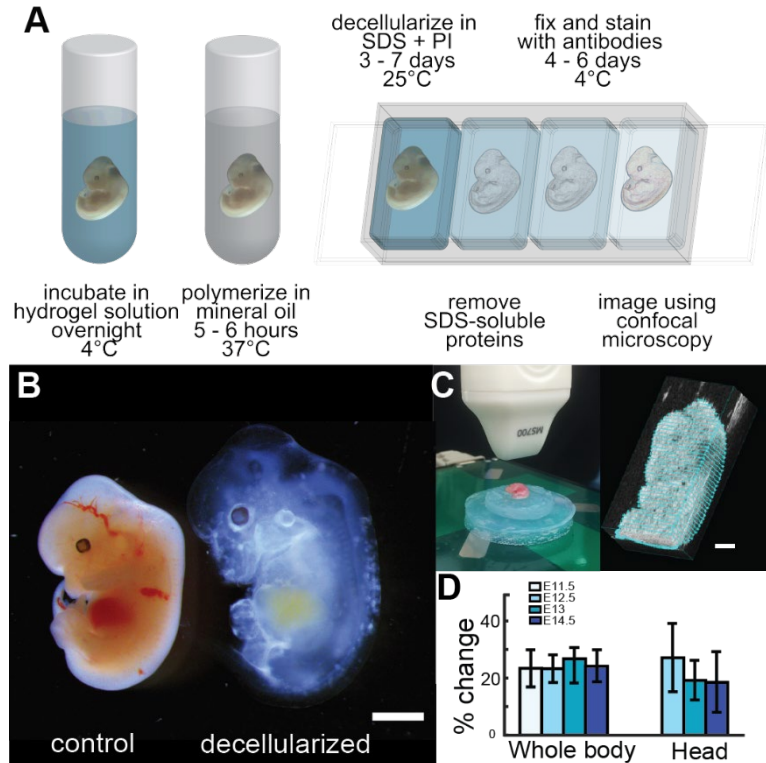


Figure 2.1. Decellularization increases transparency of murine embryos. (A) Isolated murine embryos were incubated in hydrogel solution (Table 2.1) and gently rocked at 4 °C overnight. Excess hydrogel was removed, and embryos were submerged in mineral oil at 37 °C to induce polymerization. Embryos were decellularized in sodium dodecyl sulfate (SDS) with protease inhibitor (PI) then processed for immunohistochemistry. (B) Comparison of control and decellularized E12.5 embryos from the same litter showed swelling occurred after cell removal; however, overall morphology was retained. Bar = 2 mm. (C) Ultrasound setup used to quantify changes in embryonic volume and segmentations (blue) of a E14.5 embryo before decellularization for whole body 3D rendering. Bar = 2 mm. (D) Volume changes remained consistent over the time periods investigated (n = 4; bars = SD) and were largely isotropic (see **Fig. 2.5**).

PBS in a dish suitable for confocal imaging (Ibidi, 80421) at 25 °C. Preliminary experiments showed that 0.05% SDS was the best compromise between cell removal and maintenance of networks (**Fig. 2.2**). SDS-PI solution was replaced every 24h until decellularization was complete (3–7 days). Completion of decellularization was determined by subjective visual inspection of samples for presence of cells with a light microscope, with variation in timing depending on the age and natural biological variability among samples being decellularized. Upon decellularization,

samples were rinsed in an excess of 1× PBS for 1 h, fixed in 4% paraformaldehyde (PFA) for 1h and then rinsed again in 1× PBS for 1h at 25 °C with gentle rocking.

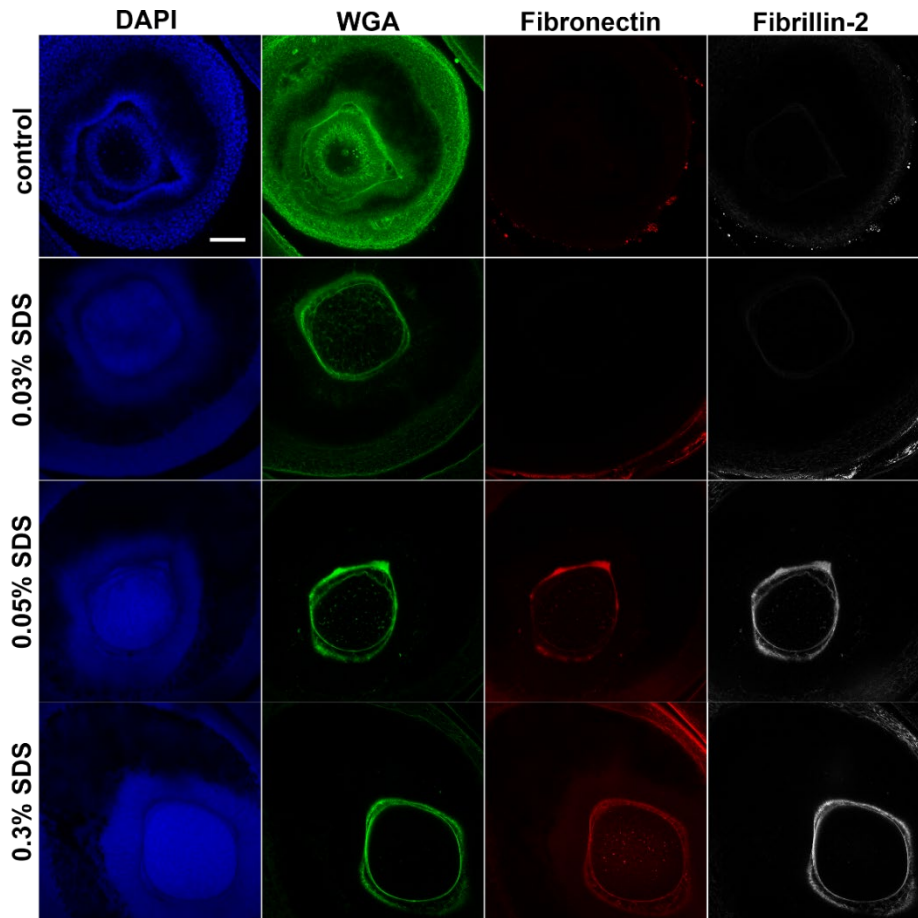


Figure 2.2 Influence of SDS concentration on ECM visualization. E12.5 embryos were permeated with hydrogel, decellularized with 0.03 – 0.3% SDS and then stained for nuclei (DAPI, blue), proteoglycans (WGA, green), fibronectin (red) and fibrillin-2 (white). Control samples were not incubated in hydrogel or SDS. Eyes were imaged at 25×. Nuclei became disrupted as SDS increased but DNA was not completely removed. WGA labeling substantially decreased with SDS treatment, due to the removal of cell surface proteoglycans. FN and FBN2 could only be visualized at 0.05 – 0.3% SDS. Bar = 100  $\mu$ m.

To confirm decellularization enhanced visualization of the ECM and demonstrate that network structure was maintained, littermates serving as whole-mount and cleared controls were rinsed in 1× PBS immediately after harvest and then fixed in 4% PFA overnight at 4 °C. After PFA fixation, control embryos were transferred to 1× PBS for storage at 4 °C until processed for imaging as described below.

Table 2.1. Composition of hydrogel solution to create polyacrylamide framework. Modified from Chung *et al.*, 2013<sup>78</sup>.

Component	Working Concentration	Source	Product #
40% acrylamide	4%	Bio-Rad	161-0140
2% bisacrylamide	0.1%	Bio-Rad	161-0142
VA-044 initiator	0.25%	Wako	VA-044
10x PBS	1x	Invitrogen	10010
Deionized water	–	–	–

### 2.3.3 Fluorescent labeling of ECM

After PFA fixation, decellularized and control samples were incubated in blocking buffer [10% donkey serum diluted in 1× PBS with 1% Triton X-100 (PBST) and 0.02% sodium azide] for 16 h at 4 °C to increase the ability of antibody stains to permeate through the sample and to block non-specific binding. Samples were then incubated with primary antibodies (**Table 2.2**) diluted in blocking buffer, and gently rocked at 4 °C for 48 h. Samples were rinsed 3 × 30 min with 1% PBST at 25 °C, and then incubated with secondary staining reagents (**Table 2.2**) diluted in blocking buffer, placed in a lightproof container, and gently rocked at 4 °C for 48 h. Samples were rinsed 3 × 30 min with 1% PBST at 25 °C and stored in 1× PBS at 4 °C until imaged.

Table 2.2 Antibodies and stains used for fluorescent labeling of embryonic ECM.

Antibody or stain	Type	Dilution	Source	Product #
$\alpha$ -fibrillin-2	rabbit polyclonal	1:200	Dr. Robert Mecham	
$\alpha$ -fibronectin	mouse IgG1	1:100	Sigma	F7387
$\alpha$ -perlecan	rat	1:50	SCBT	sc33707
$\alpha$ -type VI collagen	rabbit polyclonal	1:200	Millipore	AB7821
$\alpha$ -tenascin-C	rat	1:50	R&D	MAB2138
$\alpha$ -rabbit AF647	donkey	1:500	ThermoFisher	A31573
$\alpha$ -mouse AF555	goat	1:500	ThermoFisher	A21422
$\alpha$ -rat DyLight 550	donkey	1:250	ThermoFisher	SA5-10027
DAPI		1:500	Biotium	40011
WGA AF488		1:100	ThermoFisher	W11261

### 2.3.4 Clearing of control tissues

To confirm that ECM structure was maintained after decellularization, tissues were cleared following (Ke *et al.*, 2013). D-(-)-fructose (JT Baker, Center Valley, PA) was dissolved in milliQ water with 0.5%  $\alpha$ -thioglycerol (Sigma-Aldrich St. Louis, MO) to generate fructose solutions of varying concentrations (20%, 40%, 60%, 80%, 100% and 115% wt/vol). Tissues were equilibrated to increasing concentrations of fructose by incubating in each formulation under gentle rocking at room temperature, following the timeline defined in Ke *et al.*<sup>79</sup>.

### 2.3.5 Cryosectioning of control tissues

To visualize the fibrillar structure of ECM within intact tissues, freshly harvested E14.5 forelimbs were embedded in Optimal Cutting Temperature compound (Sakura Finetek), frozen with dry ice-cooled isopentane and stored at 80 °C. 17  $\mu$ m-thick cryosections were collected on His-bond glass slides (VWR) and processed following Calve *et al.*<sup>86</sup> using the antibody concentrations defined in **Table 2.2**. Sections were imaged at 25 $\times$  using a Zeiss LSM 880 confocal.

### 2.3.6 Imaging

Decellularized and control samples were imaged using one of the following confocal microscopes: 1) an inverted Zeiss LSM 710 confocal using either a 10 $\times$  Plan-Neofluar (NA = 0.3) or a 25 $\times$  multi-immersion LD LCI Plan-Apochromat (NA = 0.8) objective (**Fig. 2.2; 2.3A, B**), 2) an upright Zeiss LSM 800 confocal using either the 10 $\times$  Plan-Neofluar (NA = 0.3), a 20 $\times$  water immersion Plan-Apochromat (NA = 1.0) objective or a 63 $\times$  water immersion C-Apochromat (NA = 1.2) (**Figs. 2.6A, D; 2.7**) or 3) an inverted Zeiss LSM 880 confocal using either the 10 $\times$  EC-Plan-NeoFluar (NA = 0.3), 25 $\times$  multi-immersion LD LCI Plan-Apochromat (NA = 0.8) or a 40 $\times$  water immersion C-Apochromat (NA = 1.2) objective (**Figs. 2.3C, D; 2.4; 2.6B, C, E, F**). Widefield images were acquired using a Leica M80 stereo microscope.

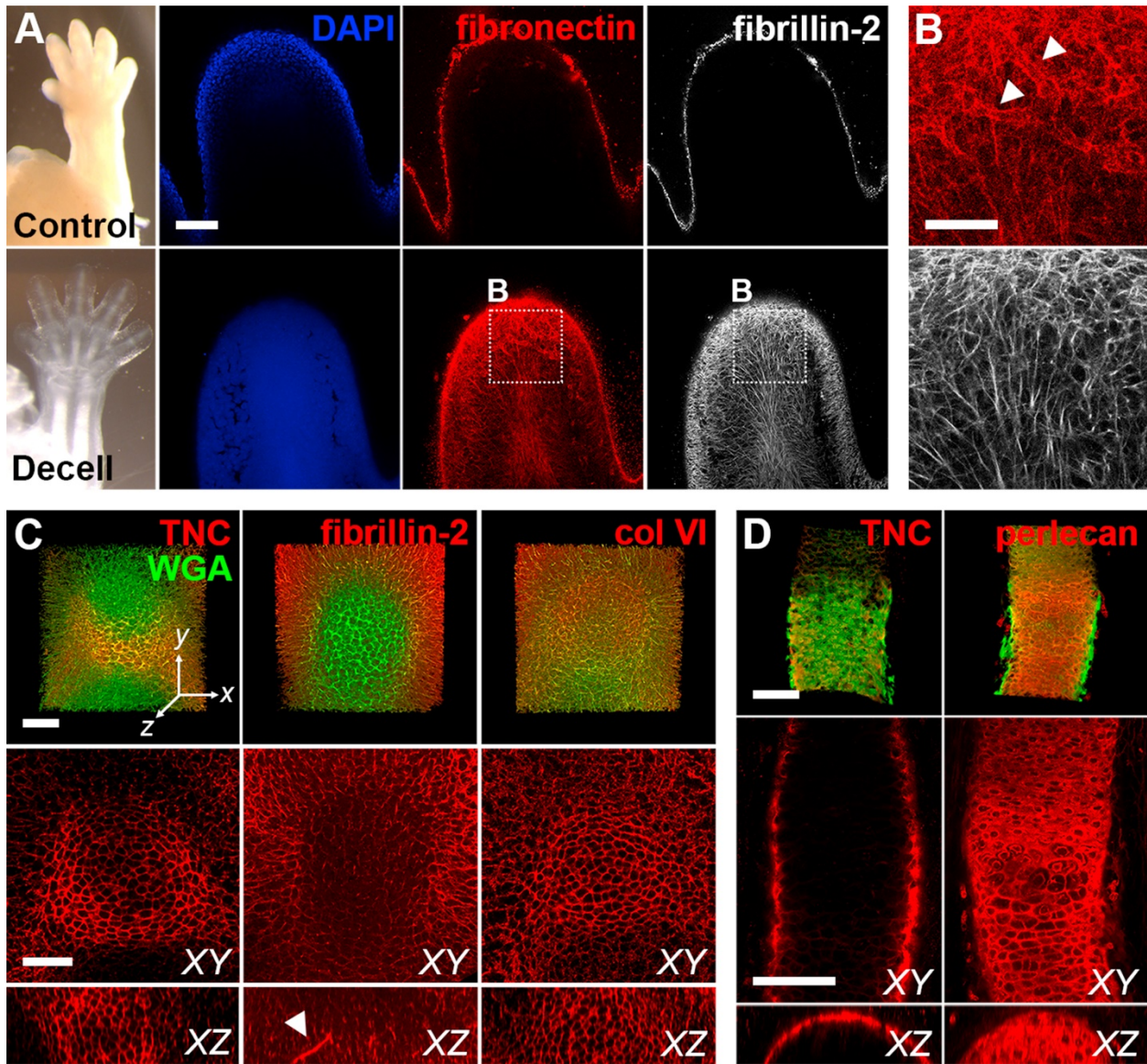


Figure 2.3 Decellularization increases matrix visibility and retains independent networks. (A) E14.5 control and decellularized forelimbs were stained for fibronectin (FN; red) and fibrillin-2 (FBN2; white) and digit tips were imaged using confocal microscopy (blue = DAPI). Bar = 100  $\mu$ m. (B) Higher magnification view of A reveals FN and FBN2 maintain independent, interpenetrating networks after removal of cells with SDS. Arrowheads show FN+ blood vessels. Bar = 50  $\mu$ m. (C, D) The native distribution of different ECM was maintained in developing cartilage and bone in decellularized E14.5 forelimbs. Tenascin-C (TNC, red) expression was restricted to the periphery of the developing cartilage (left). FBN2 (red) was localized to fibrils within the cartilage (middle). YZ section shows extended FBN2-expressing microfibril (arrowhead). Type VI collagen (col VI, red) was found throughout the developing cartilage (right). Green = WGA. Bars = 50  $\mu$ m. Dimensions of stacks in C: 237  $\times$  237  $\times$  78  $\mu$ m (x  $\times$  y  $\times$  z). (D) TNC (red, left) was restricted to the perichondrium/periosteum in the developing long bone, whereas perlecan (red, right) was found throughout the tissue. Green = WGA. Bars = 100  $\mu$ m, axes oriented as in C. Dimensions of stacks in D: 242  $\times$  338  $\times$  69  $\mu$ m.

### 2.3.7 Image processing

Confocal stacks were rendered in 3D using FIJI (NIH). Background antibody staining in some images was reduced using the despeckle algorithm in FIJI (**Figs. 2.3C, D; 2.4; 2.6**), which uses a  $3 \times 3$  median filter to decrease noise. Due to the attenuation of signal when imaging deeper within tissues, some images were processed using the Enhance Local Contrast (CLAHE) plugin to equalize large variations in intensity across tiled image stacks (**Figs. 2.4A'; 4A, D**). For cryosections, image stacks were processed into maximum z- projections using FIJI (**Fig. 2.9**). Figures were assembled by taking snapshots of 3D-rendered image volumes or selecting 2D slices from stacks and were arranged using Adobe Photoshop and Illustrator.

### 2.3.8 Ultrasound quantification of embryo swelling

A high frequency small animal ultrasound system (Vevo2100; FUJIFILM VisualSonics, Toronto, ON, Canada) was used to quantify the change in embryo dimensions during decellularization. Embryos were imaged immediately after polymerization and again after completion of decellularization (3–7 days). Embryos were placed in an agarose bed and covered with ultrasound transmission gel. A 50 MHz center frequency transducer with an axial resolution of  $30 \times 75 \mu\text{m}^2$  and an elevation resolution of 0.154 mm was positioned perpendicular to the embryo (**Fig. 2.1C**). Similar to previous work<sup>87</sup>, sequential transaxial brightness mode (B-mode) images were combined to create ultrasound volumes (0.19 mm step size). Images were analyzed with Vevo LAB software (FUJIFILM VisualSonics) to obtain area and volume measurements by manually segmenting the embryonic head and whole body (**Fig. 2.1C**). Area measurements in the sagittal, transverse, and coronal planes were used to determine if tissue expansion was isotropic (**Fig. 2.5**).

### 2.3.9 Statistical analyses

Percent change during decellularization was calculated by subtracting the area and volume after decellularization from the initial measurements. Tukey-Kramer HSD was performed on the percentage area change in the transverse, coronal, and sagittal planes (**Fig. 2.5**) at E12.5, E13, and E14.5 ( $n = 4$ ) for statistical significance using JMP. Similarly, the percentage change in whole

embryo and head volumes at these embryonic stages ( $n = 4$ ) were analyzed with Tukey-Kramer HSD for statistical significance. Confidence quantile alpha was set at 0.05.

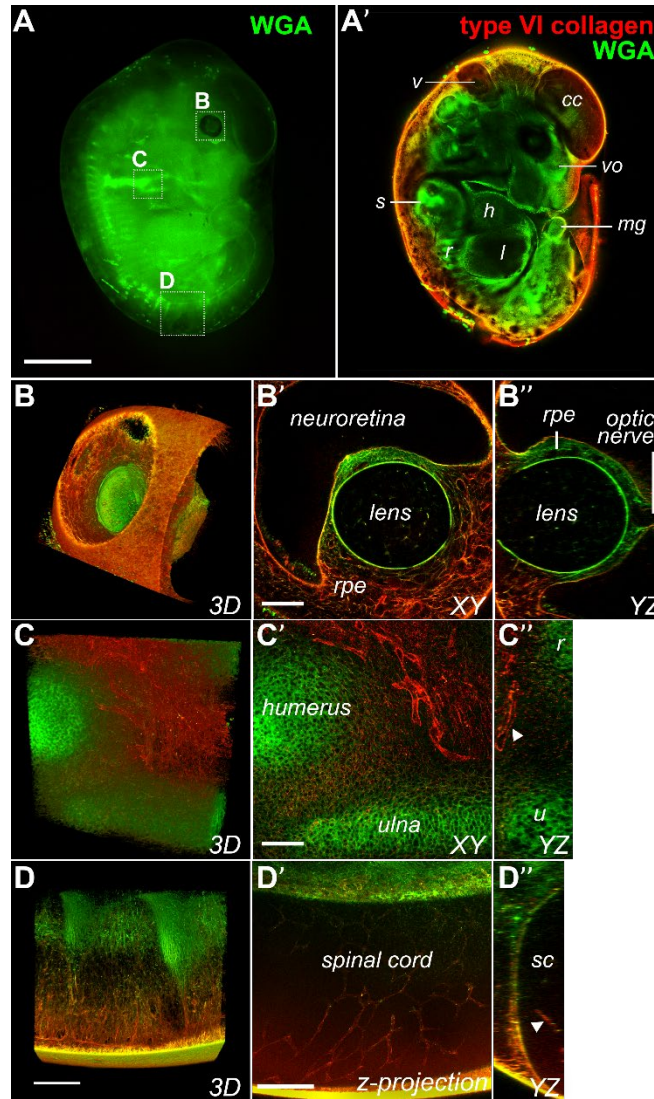


Figure 2.4 3D visualization of ECM in E12.5 embryo. (A) Widefield view of WGA-stained E12.5 decellularized embryo. (A') Virtual confocal section of E12.5 embryo stained with WGA (green) and type VI collagen (red).

Various structures can be identified including the 4th ventricle of the brain (v), future cerebral cortex (cc), vomeronasal organ (vo), scapula (s), midgut (m), liver (l), heart (h) and ribs (r).  $10\times$ , bar = 2 mm. (B-B''): 3D rendering of the eye at  $25\times$  ( $567 \times 567 \times 395 \mu\text{m}$ ;  $x \times y \times z$ ). The vascularization of the vitreous body (vb) can be visualized (B') and the lens and optic nerve can be clearly resolved in a YZ projection of the image stack. Bars =  $100 \mu\text{m}$ . (C-C'') 3D rendering reveals dense vascular network around the elbow ( $567 \times 567 \times 186 \mu\text{m}$ ). Comparison of XY (C') and YZ planes (C'') revealed that blood vessels remained patent.  $25\times$ , bars =  $100 \mu\text{m}$ . (D-D'') 3D rendering of developing spinal cord at  $10\times$  ( $850 \times 850 \times 251 \mu\text{m}$ ). Z-projection of 12 slices ( $70 \mu\text{m}$ ) shows maintenance of spinal cord vascularization (D') and intact blood vessel in the YZ projection (arrowhead; D''). Bars =  $200 \mu\text{m}$ .

## 2.4 Results and Discussion

### 2.4.1 Decellularization increases embryo transparency

To enhance the visibility of the developing matrix, freshly harvested embryonic tissues were decellularized following standard detergent- based methods formulated for adult tissues<sup>81</sup>, but we observed that the tissues did not maintain their macroscopic morphology and were easily damaged. Instead, we found that by removing the paraformaldehyde from the hydrogel utilized in the CLARITY method<sup>78</sup>, a hydrogel framework was formed that did not cross-link to biomolecules and retained the 3D organization of the insoluble matrix (**Fig. 2.1**). Hydrogel-based protocols tend to surround samples with an excess of solution, which generates superficial hydrogel after polymerization that needs to be removed prior to imaging<sup>78,88</sup>. Unlike stiffer adult tissues, fragile embryonic samples can be damaged during this process. To address this problem, excess hydrogel solution was removed before polymerization and the embryos were placed in mineral oil, which is immiscible with the aqueous acrylamide-based hydrogel. After polymerization, there was minimal hydrogel on the surface of the specimen that could interfere with confocal imaging. Additionally, the hydrogel increased tissue rigidity, making the samples easier to handle and less susceptible to damage during staining and imaging.

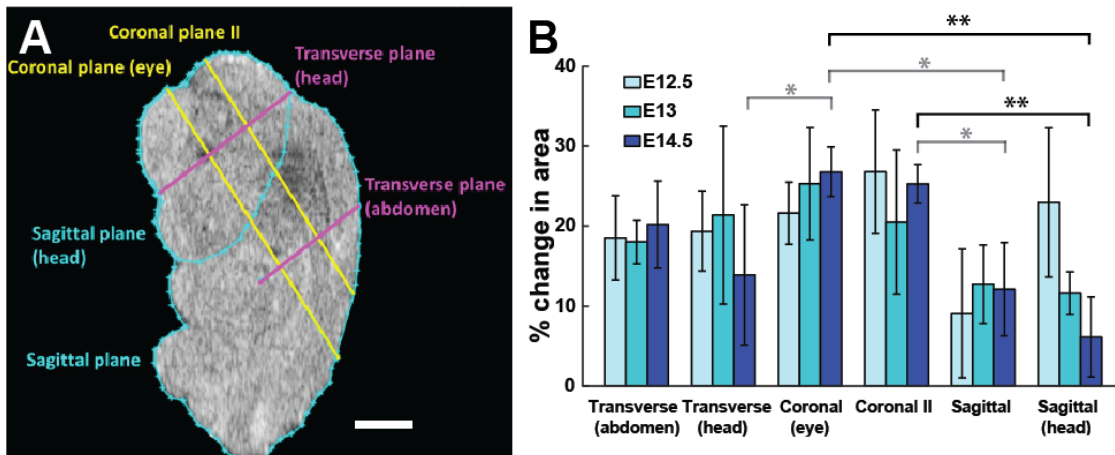


Figure 2.5. No significant differences in embryo swelling at earlier stages of development. (A) Location of the area measurements taken before and after decellularization to quantify expansion from 3D segmentations. Scale bar=2 mm. (B) Percentage change in areas in different anatomical imaging planes. The percentages of change in different planes are only statistically significant at E14.5, suggesting swelling is isotropic at the earlier stages (n=4; \*p<0.05; \*\*p<0.005; error bars = SD).

Since the nascent embryonic ECM is likely to be less stable than ECM found in adult tissues, preliminary studies to determine the minimal concentration of sodium dodecyl sulfate (SDS) that increased tissue transparency, while also preserving ECM architecture, were conducted. Network visualization was greatly enhanced after treatment with 0.05% SDS in PBS (**Fig. 2.2**). Staining for nucleic acids (DAPI, blue) indicated that tissues were not fully decellularized (**Figs. 2.2, 2.3A**); however, the primary goal of this study was to increase matrix visibility and not to create scaffolds devoid of cellular components for implantation where DNA and proteins can promote an immune response. Since the ability to resolve ECM architecture was greatly enhanced even with the presence of residual DNA, further optimization of the decellularization process was not conducted to minimize disruption of ECM network architecture.

Removal of soluble components greatly increased embryo transparency; however, noticeable swelling occurred (**Fig. 2.1B**). Swelling was attributed to removal of cellular links between matrices and/or from the inherent swelling properties of polyacrylamide<sup>89</sup>. To assess if swelling was isotropic, changes in embryo volume were quantified using ultrasound before and after incubation in 0.05% SDS. Swelling caused by decellularization remained constant across all time points investigated and was generally isotropic (**Fig. 2.1B**). Expansion in the direction of the sagittal plane tended to be lower than in other directions but was only significant at E14.5 (**Fig. 2.5**). Significant differences between changes in area at E14.5 were also observed between coronal, transverse and sagittal planes, which was attributed to swelling constraints brought upon by the formation and connection of cartilage elements in the developing skeleton, particularly the vertebral column (**Fig. 2.5**). Sample expansion is not typically considered detrimental to the 3D study of native tissue and has been documented during the implementation of techniques such as CUBIC<sup>90</sup>, CLARITY<sup>78</sup>, and PACT<sup>85</sup>. Indeed, tissue swelling has been used to enhance the resolution of smaller samples as demonstrated with expansion microscopy in which a hydrogel framework swells to 4.5× the original size and does not negatively influence cellular architecture<sup>91</sup>.

#### **2.4.2 Independent ECM networks are maintained after cell removal**

To demonstrate that our method increases ECM visibility and maintains independent protein networks, control and decellularized E14.5 digit tips were imaged at approximately the same depth. The structure of FN and FBN2 within control tissue could not be visualized beyond the surface (**Fig. 2.3A**). In contrast, independent and interpenetrating networks of FN and FBN2 were clearly

resolved in the decellularized samples (**Fig. 2.3B**). FN was widely distributed and outlined the blood vessels (arrowheads; **Fig. 2.3B**), consistent with the proposed role for FN during vasculogenesis<sup>92,93</sup>. FBN2 was arranged in a dense network of microfibrils, similar to what has been shown in mouse hindlimb<sup>94</sup>.

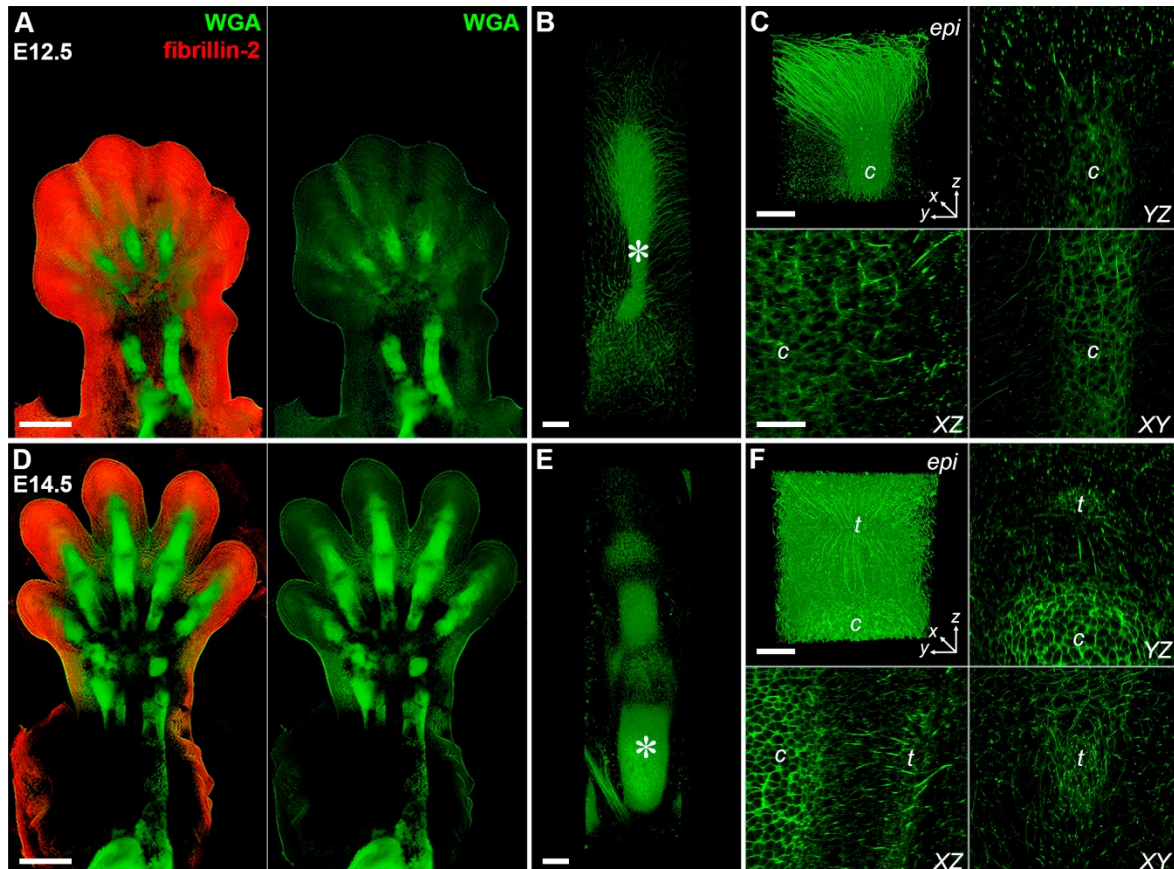


Figure 2.6. Multiscale imaging of the musculoskeletal system in the developing forelimb. E12.5 (A – C) and E14.5 (D – F) forelimbs were decellularized and stained with WGA (green) and an antibody against fibrillin-2 (FBN2, red). Dorsal view. (A, D) Cartilage elements of the autopod and zeugopod were easily resolved with WGA. FBN2 became more restricted with time. 10 $\times$ , bar = 500  $\mu$ m. (A: 2471  $\times$  3599  $\times$  600  $\mu$ m; D: 2799  $\times$  4733  $\times$  450  $\mu$ m; x  $\times$  y  $\times$  z) (B, E) 3D rendering of digits showed a network of WGA+ fibrils radiating from the cartilage as well as staining of joint tissues and the extensor tendons. 25 $\times$ , bar = 100  $\mu$ m. (381  $\times$  1364  $\times$  289  $\mu$ m). (C, F) Higher magnification of digits in B, E (\*) revealed WGA+ fibrils extended from dorsal epidermis (epi) to cartilage (c) at E12.5 and at E14.5 fibrils appeared to connect the extensor tendons (t) to the epidermis and cartilage. 40 $\times$ , bars = 50  $\mu$ m, (213  $\times$  213  $\times$  227  $\mu$ m).

To confirm SDS treatment did not interfere with the spatial organization of ECM at the tissue level, E14.5 forelimbs were stained for proteins with known differential distributions in developing cartilage and images were collected of the distal phalanx and long bones in the zeugopod. Samples were counterstained with AF488-conjugated wheat germ agglutinin (WGA; green), which binds

to proteoglycans containing sialic acid and N-acetylglucosamine and provides a global label for musculoskeletal tissue ECM<sup>95</sup>. As expected, tenascin-C expression (TNC; red) was restricted to the periphery of the cartilage condensation (**Fig. 2.3C**), which persisted during ossification (**Fig. 2.3D**)<sup>12,96,97</sup>. FBN2 (red) was distributed as discrete microfibrils within cartilage and was present at a higher density in the surrounding mesenchyme (**Fig. 2.4C**)<sup>98</sup>. In contrast, type VI collagen (col VI) and perlecan were found throughout the entire cartilage (**Fig. 2.4C,D**). While col VI and perlecan are associated with the pericellular ECM in adult cartilage, both are widely distributed during the early stages of chondrogenesis and gradually become restricted to the periphery of the chondrocytes as development progresses<sup>14</sup>. In addition, perlecan is highly expressed during the transition from cartilage to bone<sup>99</sup>.

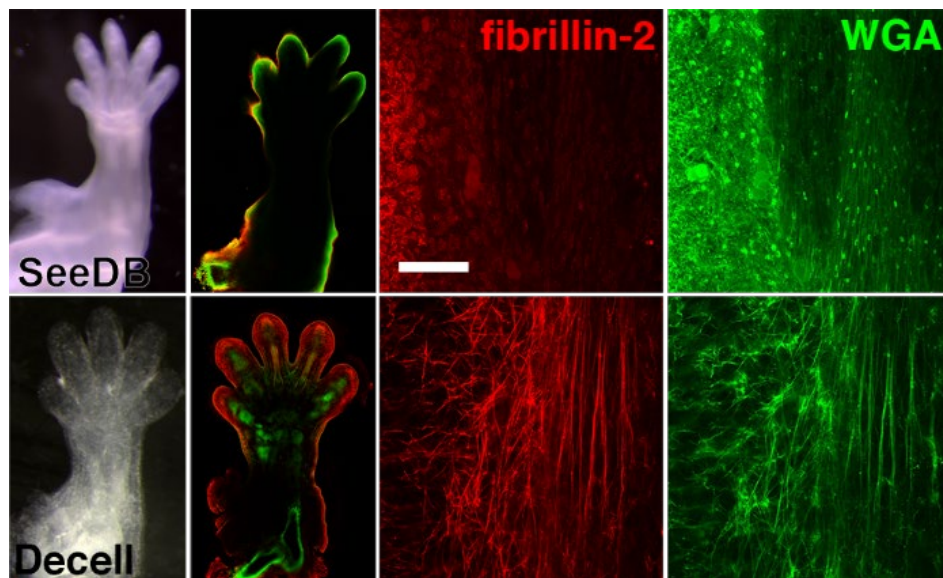


Figure 2.7. SeeDB is not effective for visualization of ECM within the developing embryo. E14.5 forelimbs were either cleared with SeeDB or decellularized and stained for fibrillin-2 or WGA. Virtual cross-sections at 10× demonstrate that staining in SeeDB samples is mostly restricted to the periphery. Higher resolution imaging (63×) of a tendon within the zeugopod reveals minimal penetration of FBN2 antibody and WGA into SeeDB sample (epidermis is to the left of the image).

The ability of our method to resolve matrix architecture was compared with SeeDB. FBN2 (red) and WGA (green) visualization was greatly enhanced in decellularized samples (**Fig. 2.7**). The ECM of a tendon within the zeugopod was intensely stained in the decellularized tissue, whereas little to no FBN2 signal was observed in the same tendon in the limb cleared with SeeDB, which was attributed to limited antibody penetration in the denser SeeDB sample.

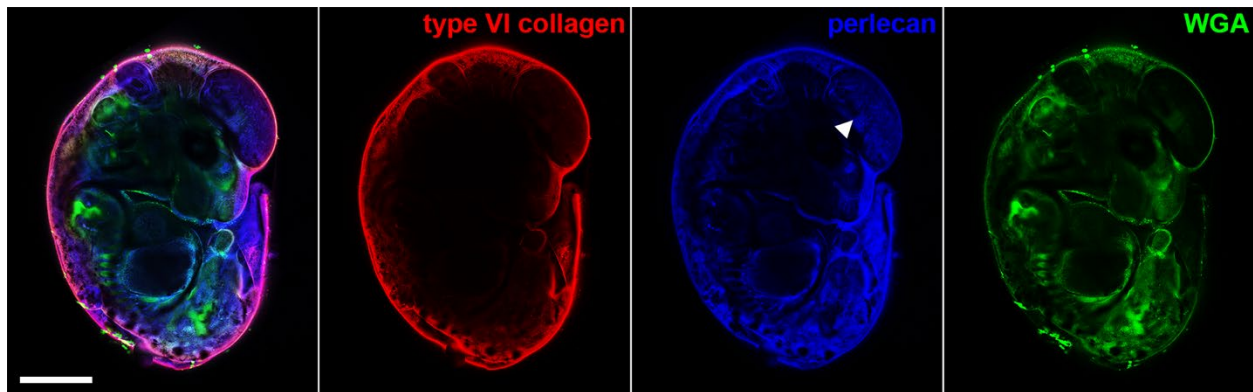


Figure 2.8. Differential penetration of antibodies into decellularized embryos. Anti-perlecan (blue) showed substantial more penetration into the decellularized E12.5 embryo from Fig. 3 than anti-type VI collagen (red), suggesting antibody penetration is limited by concentration rather than diffusion. For example, perlecan in the blood vessels of the corpus callosum (arrowhead) were labeled at least 1mm deep. 10 $\times$ , bar = 2 mm.

### 2.4.3 Intact embryos can be visualized at multiple scales

To demonstrate the macroscopic structure of developing tissue was maintained, E12.5 embryos were stained with WGA (green) and an antibody against col VI (red; **Fig. 2.4**). Skeletal elements of the forelimbs and ECM supporting the dorsal root ganglia along the developing spinal cord were easily resolved under a dissecting microscope (**Fig. 2.4A**). Sagittal confocal slices enabled the identification of internal organs and tissues within the embryo, including the 4th ventricle of the brain (*v*), future cerebral cortex (*cc*), vomeronasal organ (*vo*), scapula (*s*), midgut (*m*), liver (*l*), heart (*h*) and ribs (*r*; **Fig. 2.4B**). WGA (MW = 38 kDa) diffused through the entire specimen, whereas the antibody against col VI (MW = 150 kDa) could only be imaged to a depth of 150–200  $\mu$ m. The limited depth of staining can be attributed to a large number of type VI epitopes in the surface tissues rather than a limitation in diffusion as an antibody against perlecan was able to penetrate further into the same sample (**Fig. 2.8**). We expect that increasing the concentration of anti-type VI collagen will enhance the depth of labeling. The developing eye could be clearly visualized at 25 $\times$ , wherein blood vessels of the vitreous body (*vb*) were outlined with col VI (**Fig. 2.4B**). In contrast, the predominantly cellular neuroretina and lens were devoid of signal. An orthogonal cross-section of the z-stack from **Fig. 2.4B** shows that lens architecture and stalk of the optic nerve were maintained (**Fig. 2.4B'B''**). Cartilage elements of the elbow were intensely stained with WGA and were surrounded by a col VI+ network of patent blood vessels

(arrowhead, **Fig. 2.4C-C''**). WGA staining formed an inverse pattern with the dorsal root ganglia along the developing spinal cord (**Fig. 2.4A, D**), which is likely made up of proteoglycans such as versican that inhibit neural crest and axon migration<sup>100</sup>. Notably, the intricate architecture of the vasculature within the spinal cord was maintained (arrowhead; **Fig. 2.4D', D''**), providing further evidence that our method can maintain the integrity of delicate networks.

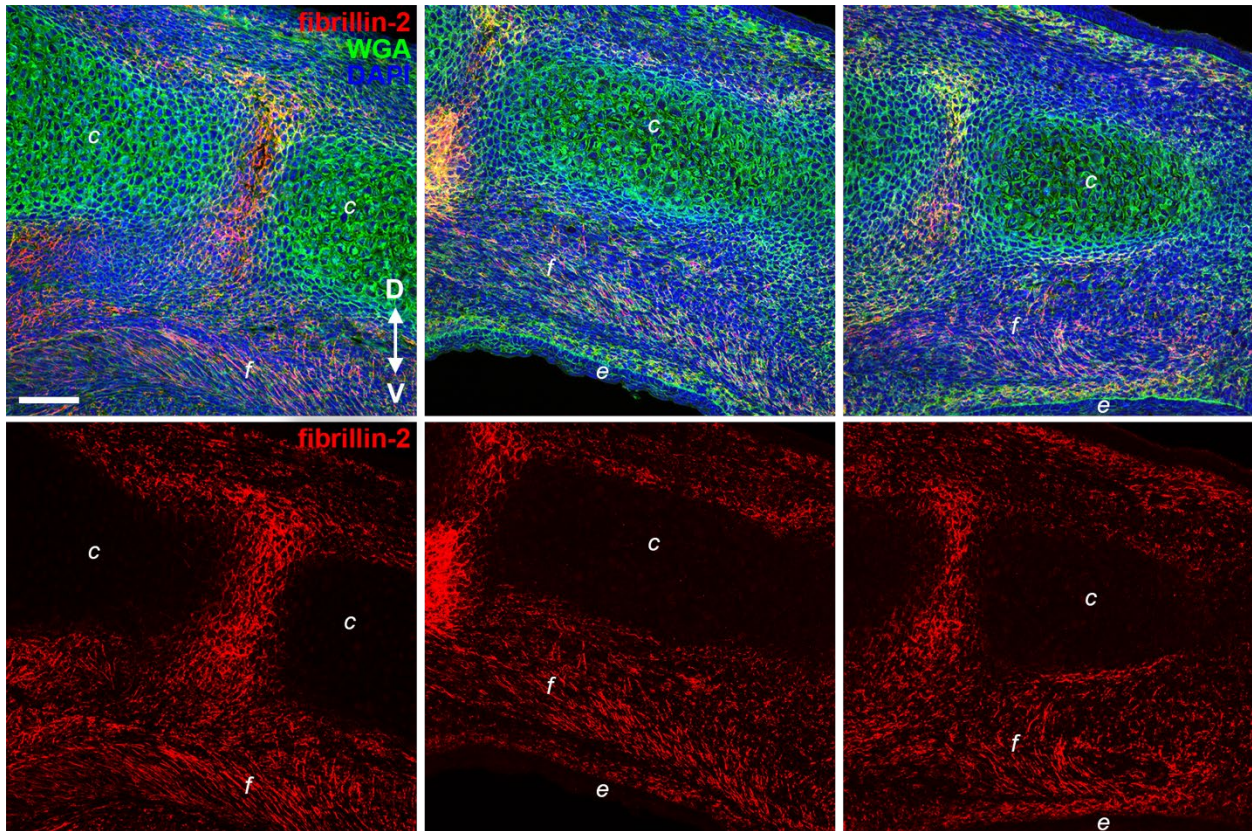


Figure 2.9. Presence of fibrillar networks within intact tissues. E14.5 forelimbs were sectioned and stained with WGA (green) and an antibody against fibrillin-2 (red). Fibrils (f) extending between the epidermis (e) and cartilage (c) were observed on the ventral side of the developing digit. Blue = DAPI, 25 $\times$ , bar = 50  $\mu$ m.

#### 2.4.4 The epidermis is linked to the underlying musculoskeletal tissues via proteoglycan-rich fibrils

Comparative analysis of the developing forelimbs between E12.5 and E14.5 revealed that FBN2 expression decreased between the time points (**Fig. 2.6A**), consistent with a decrease in FBN2 transcripts as a function of limb development<sup>94</sup>. The increase in the number of phalanges and articulation between the joints as development progresses was resolved by WGA labeling (**Fig.**

**2.6B, E**). Higher resolution imaging of the ECM in the digit revealed continuous proteoglycan-based fibrils extending from the epidermis (*epi*) to the developing cartilage (*c*), even after the formation of the extensor tendons (*t*; **Fig. 2.6C, F**). Cryosections of control E14.5 limbs show FBN2+ fibrils extending between the ventral epidermis and internal tissues (**Fig. 2.9**), indicating that the architecture visualized in **Fig. 2.6C and F** is likely not an artifact of the decellularization process. Recent genetic knockdown studies indicated that signals secreted by cartilage and epidermis, such as Wnts and Noggin, can influence the induction of autopod tendons<sup>101,102</sup>. The persistence of proteoglycan-rich connections between the epidermis and cartilage during tendon specification from E12.5 to E14.5, in combination with previous studies showing that elastic fibrils appear to anchor developing tendons to the perichondrium in the developing chick limb<sup>103,104</sup>, suggest that the matrix also plays a role in regulating extensor tendon development in the autopod.

## 2.5 Conclusions

The goal of this study was to establish a method that would enable us to visualize the ECM during the early stages of musculoskeletal development (E11.5 – E14.5). Our method will have limited application for intact embryos after E15.5 when the barrier function of the skin is acquired<sup>105</sup>, preventing the diffusion of the hydrogel solution into the tissues. Nevertheless, we expect that it should be feasible to process isolated tissues from most developmental stages. It may be necessary to increase the SDS concentration as the tissues become denser; however, by those stages, the stabilization of the geometry using the hydrogel will likely be unnecessary. Our future studies aim to investigate more finely resolved time points so that a clearer picture will emerge regarding the role the ECM plays during forelimb musculoskeletal assembly as well as all other organ systems within the developing embryo.

### 3. *IN SITU* MEASUREMENT OF NATIVE EXTRACELLULAR MATRIX STRAIN

Now that we have established a novel decellularization technique to enhance extracellular matrix (ECM) visualization during embryonic development, the next step is to quantify ECM strain after the application of load. By acquiring confocal images before and after compression, we are able to investigate the deformation of different ECM proteins and two tissue organizations, loose connective tissue and cartilage, in the developing digit tip. Decellularization and confocal imaging are coupled with image processing digital volume correlation algorithms to extract displacement and strain fields of ECM networks. The results presented here demonstrate the unique ability of our method to resolve and quantify 3D geometry-specific ECM deformation and strain. The content presented in this chapter is adapted from our work “*In situ* measurement of native extracellular matrix strain”, published in *Experimental Mechanics*. Minor edits to the formatting have been made, such as including the supplemental data for the published article in this chapter, to produce a cohesive dissertation. The published version of this chapter is available at the following link: <https://doi.org/10.1007/s11340-019-00499-y>.

#### 3.1 Abstract

Cells directly interact with the extracellular matrix (ECM) in their microenvironment; however, the mechanical properties of the networks at this scale are not well defined. This work describes a method to quantify ECM network strain *in situ* after the application of a known load. Visualization of the ECM in the native 3D organization is facilitated using murine embryos and a novel decellularization method. During embryonic development, the ECM architecture is less dense making it easier to visualize and manipulate. Briefly, E14.5 forelimbs were harvested and incubated in an acrylamide-based hydrogel mixture to maintain the 3D architecture of the ECM during decellularization. After decellularization, forelimbs were stained for fibrillin-2 and proteoglycans to visualize different networks. Samples were imaged, before and after the application of a static load, using confocal microscopy. A MATLAB-based fast iterative digital volume correlation algorithm was used to quantify network displacement fields by comparing the reference and compressed z-stacks. We observed that the amount of Green-Lagrange strain experienced by different proteins was dependent on whether the sub-region analyzed was located within cartilage or the adjacent connective tissue. The combination of these experimental and computational methods will enable the development of constitutive equations that describe the

material behavior of ECM networks. In the future, this information has the potential to improve the fabrication of physiologically relevant scaffolds by establishing mechanical guidelines for microenvironments that support beneficial cell-ECM interactions.

### 3.2 Introduction

The evolution of the extracellular matrix (ECM) enabled the advent of multicellular organisms and plays a large role in defining the mechanical properties of biological tissues<sup>106</sup>. The proteins, proteoglycans and glycosaminoglycans that constitute the ECM are arranged into higher-level structures through a combination of self-assembly into fibrils or networks and cell-mediated organization. The local composition and architecture depend on the biomechanical requirements of the tissue of interest<sup>107</sup>. Conversely, ECM stiffness and composition combine to influence cellular behaviors including migration<sup>13</sup>, proliferation<sup>13</sup>, durotaxis<sup>108</sup>, and differentiation<sup>109</sup>. To decipher how cues from the extracellular environment regulate intracellular mechanisms that direct specific behaviors, hydrogels assembled *in vitro* have been used as experimental test beds<sup>110</sup>. Typically, these hydrogels are made out of artificial polymers or a single ECM component that likely do not recapitulate the mechanical properties of native ECM networks. Unfortunately, the precise mechanical properties that these hydrogels should emulate remain unclear.

The mechanical response of the ECM is easily measured at molecular and macroscopic scales; however, the material properties at the network/fibrillar (mesoscopic) level are not well defined. This can be attributed to the relative insolubility of ECM networks, which precludes the extraction of intact fibrils for mechanical testing. Researchers circumvent this problem by either generating fibrils *in vitro*<sup>111,112</sup>, or isolating single fibrils from the native environment<sup>113,114</sup>; however, these methods come with a number of constraints. Without cells and accessory ECM molecules to orchestrate proper assembly, networks synthesized *in vitro* will not have the same organization and material properties as those deposited *in vivo*. Furthermore, analysis of single fibrils will not provide information regarding the mechanics of the entire network.

Visualization of ECM architecture *in situ* is hindered by the composite nature of intact tissues. Resident cells induce light scattering, which prevents visualization of networks beyond the superficial surface layers<sup>65</sup>. Decellularization using mild detergents can remove cellular interference; however, most adult tissues are dense and individual networks remain difficult to resolve. To address this limitation, we developed a novel method to map the 3D organization of

ECM networks using murine embryos<sup>115</sup>. During development, the ECM architecture is less dense making it feasible to visualize discrete components of the ECM network, and provides an ideal system with which the material properties of native fibrils can be determined.

A critical component for characterizing the mechanics of the ECM at the mesoscale is to be able to reliably measure strain across large networks. Digital volume correlation (DVC) can be used to determine full field displacements from 3D images but is typically computationally intensive. To circumvent the large computational demands of DVC, a more efficient method, fast iterative digital volume correlation (FIDVC) was developed<sup>116</sup>. The FIDVC algorithm can evaluate non-linear deformations of a  $256 \times 256 \times 128$  voxel volume in roughly 5 min on a standard CPU by using an iterative deformation method similar to that used in particle image velocimetry<sup>116</sup>.

With our novel method to visualize the 3D geometry of the ECM, we have a unique opportunity to examine the material properties of networks in their native conformation. Forelimbs from embryonic day (E)14.5 murine embryos were decellularized as done previously<sup>115</sup> and stained to visualize fibrillin-2 and proteoglycans in the ECM. Samples were imaged using confocal microscopy before and after the application of a known load. ECM deformation was calculated using FIDVC and converted to strain. We found that the amount of strain experienced by different proteins appeared to depend on whether the sub-region analyzed was in cartilage or the adjacent connective tissue. Quantification of strain *in situ* is the first step towards identifying the material properties of different ECM networks. Since it is at the mesoscopic level that the rigidity of the local cellular environment is conferred, knowledge of the material properties of specific ECM networks can have a profound impact on future studies in mechanobiology

### 3.3 Experimental procedures

#### 3.3.1 Visualization of ECM fibril architecture in 3D

##### *Embryo harvest and decellularization*

All murine experiments were approved by the Purdue Institutional Animal Care and Use Committee (IACUC; protocol 1209000723). The Purdue IACUC ensures that all animal programs, procedures, and facilities at Purdue University adhere to the policies, recommendations, guidelines,

and regulations of the USDA and the United States Public Health Service in accordance with the Animal Welfare Act and Purdue's Animal Welfare Assurance. C57BL/6 mice were time-mated to generate E14.5 embryos. Dams were euthanized via CO<sub>2</sub> inhalation and cervical dislocation. Embryos were removed from the uterine horns, rinsed in chilled 1× phosphate-buffered saline (PBS), and the forelimbs were excised under a dissecting microscope (DFC450, Leica Microsystems) to avoid tissue damage.

After dissection, forelimbs were decellularized to enhance the visualization of the ECM. To maintain the native architecture, a 3D polyacrylamide framework was generated within the forelimbs as previously described<sup>115</sup>. After polymerization, each forelimb was gently rocked in 1 mL 0.05% sodium dodecyl sulfate (SDS) with 1× Halt protease inhibitor (PI, ThermoFisher) in 1× PBS. SDS-PI solution was replaced every 24 hours until decellularization was complete after 3-5 days (**Fig. 3.1**). The samples swelled slightly due to the decellularization process; however, the swelling was found to be isotropic and only led to a 20% increase in whole embryo volume across time points<sup>115</sup>. Upon decellularization, samples were rinsed in 1× PBS and fixed with 4% paraformaldehyde (PFA) for 1 hour at room temperature. After fixation with PFA, decellularized forelimbs were rinsed in 1× PBS and

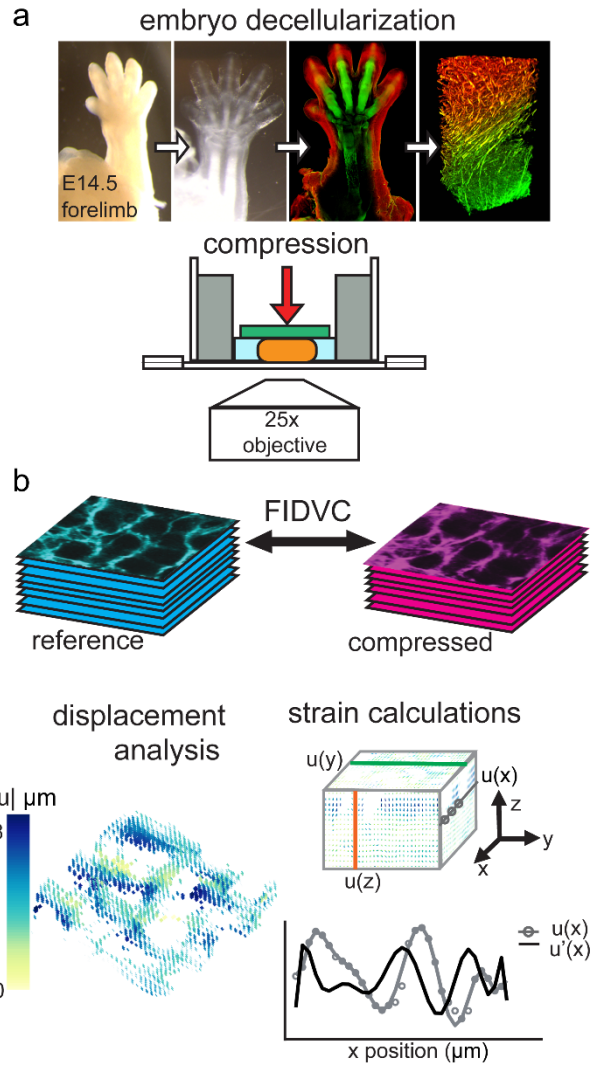


Figure 3.1. Experimental procedure. **a.** Decellularization of murine embryonic forelimbs allows the visualization of the extracellular matrix in its native conformation using confocal microscopy, after staining for ECM of interest. Decellularized forelimbs are imaged with an inverted confocal microscope while submerged in PBS. Embryo decellularization panels adapted from [12]. **b.** Volume images obtained before (cyan) and after load (magenta), corresponding to the same area of the digit, are correlated to extract displacements with fast iterative digital volume correlation (FIDVC). Displacements are analyzed and plotted in color as vector fields. Strain is calculated by fitting polynomial functions to each set of displacement values and then calculating their derivatives analytically, indicated by  $u(x)$  and  $u'(x)$ .

then incubated in blocking buffer [10% donkey serum (Lampire) diluted in 1× PBS with 0.1% Triton X-100 (PBST)] for 16 hours at 4°C to increase permeability and block non-specific binding. Samples were then incubated with a primary antibody against fibrillin-2 (FBN2; 1:200; donated by R. Mecham), diluted in blocking buffer at 4°C for 48 hours with gentle rocking. Samples were rinsed 3×30 minutes with 0.1% PBST at 25°C, then incubated with AF633 donkey anti-rabbit (1:500; ThermoFisher) to visualize anti-FBN2 and AF488-conjugated wheat germ agglutinin (WGA; 1:100; ThermoFisher) to visualize proteoglycans, diluted in blocking buffer, at 4°C for 48 hours. Samples were rinsed 3×30 minutes with 0.1% PBST at 25°C and stored in PBS at 4°C in a lightproof container until imaging.

### ***Image acquisition and load application***

Samples were imaged using an inverted Zeiss LSM 880 confocal microscope (Carl Zeiss Microscopy) using either a 10× EC-Plan NeoFluar (NA = 0.3) or a 25× multi-immersion LD LCI Plan-Apochromat (NA = 0.8) objective (**Figs. 3.1, 3.2**). A dish suitable for confocal microscopy (Ibidi, 80421) was coated with polydimethylsiloxane (PDMS; Sylgard 184; Dow Corning) and an 8mm diameter well was created using a biopsy punch. XY alignment of the weight and the forelimb sample was facilitated by the PDMS well since it minimizes user error when placing the weight. The dimensions of the loading wells were such that they allowed unconfined compression of the decellularized forelimb samples and kept both the sample and the weight within the center of the dish. Samples were surrounded with sufficient 1× PBS to keep the sample hydrated for the duration of the experiment (~2 hours), but without excess that would cause the sample to translate or float (**Fig. 3.1**).

The reference configuration was acquired by obtaining a 30-slice z-stack of images at 2048×2048 pixels from a 25× objective with a corresponding resolution of 0.23 μm/pixel ( $x, y$ ) and 1.23 μm/pixel ( $z$ ) (**Fig. 3.2**). After acquisition of the reference z-stack, a static load of 0.52 grams normal to the horizontal plane ( $-z$ ) was applied by placing a custom-made weight over the sample with minimal disruption of the original sample position. The weight was manually placed over the sample using tweezers. Samples were allowed to equilibrate for 10 minutes before imaging the compressed configuration using the same imaging parameters as above, after adjusting the starting position to account for z-translation based on distinct material landmarks. The shape of the weight and the use of a PDMS well ensured the weight remained perpendicular to the sample

during imaging. The reference and compressed configurations were acquired for five E14.5 forelimbs, all obtained from embryos from different litters, two of which are denoted as sample A and sample B.

### 3.3.2 Quantification of ECM displacement

#### *Image processing*

Both the reference and compressed z-stacks were processed as follows. To remove some of the optical distortion inherent to confocal microscopy, the Nearest Neighbor Deconvolution function within the ZenBlue software package (Carl Zeiss Microscopy) was applied. Two regions of varying morphology were investigated to test that our method could resolve region-specific differences in mechanical properties, corresponding to the cartilage of the distal phalanx and the surrounding loose connective tissue (LCT; **Fig. 3.2**). For two E14.5 forelimbs imaged (Samples A and B), sub-stacks of cartilage (n=3) and LCT (n=3) in both reference and compressed configurations were created, and the FBN2 and WGA channels were separated using FIJI (NIH). Landmarks located in the first (bottom) and last (top) slices of the reference z-stacks were used as guides to align  $22 \times 22 \times 15 \mu\text{m}^3$  sub-stacks of the same ECM location in both configurations (**Figs. 3.1, 3.2**). The dimensions of each sub-stack were resampled to be  $256 \times 256 \times 128$  voxels using the Resize function in FIJI, so the spacing of the grid of material points created during FIDVC was smaller than the features of interest (*e.g.* fibrils). The image intensity values for each pair of sub-stacks to be correlated were normalized using the Quantile Based Normalization plugin (FIJI). For each sub-stack the intensity values are ranked and divided into 256 quantiles. Then, each of the values in a quantile were replaced with the mean value of that quantile across all images in both z-stacks, resulting in a similar distribution of intensity values for both reference and compressed volume images.

Similarly, to investigate the deformation and strain for each protein network at a regional level, larger sub-stacks ( $188 \times 188 \times 15 \mu\text{m}^3$ ) were prepared for correlation and analysis, as described above. As shown with the dashed, white box in **Fig. 3.2a**, these larger sub-stacks included both cartilage and LCT in the digit. Sub-stacks from 5 different forelimbs were analyzed to investigate the variability of our method across samples, with the goal of also quantifying regional strain differences at a larger spatial scale. The dimensions of each larger sub-stack were resampled to be  $1920 \times 1920 \times 128$  voxels.

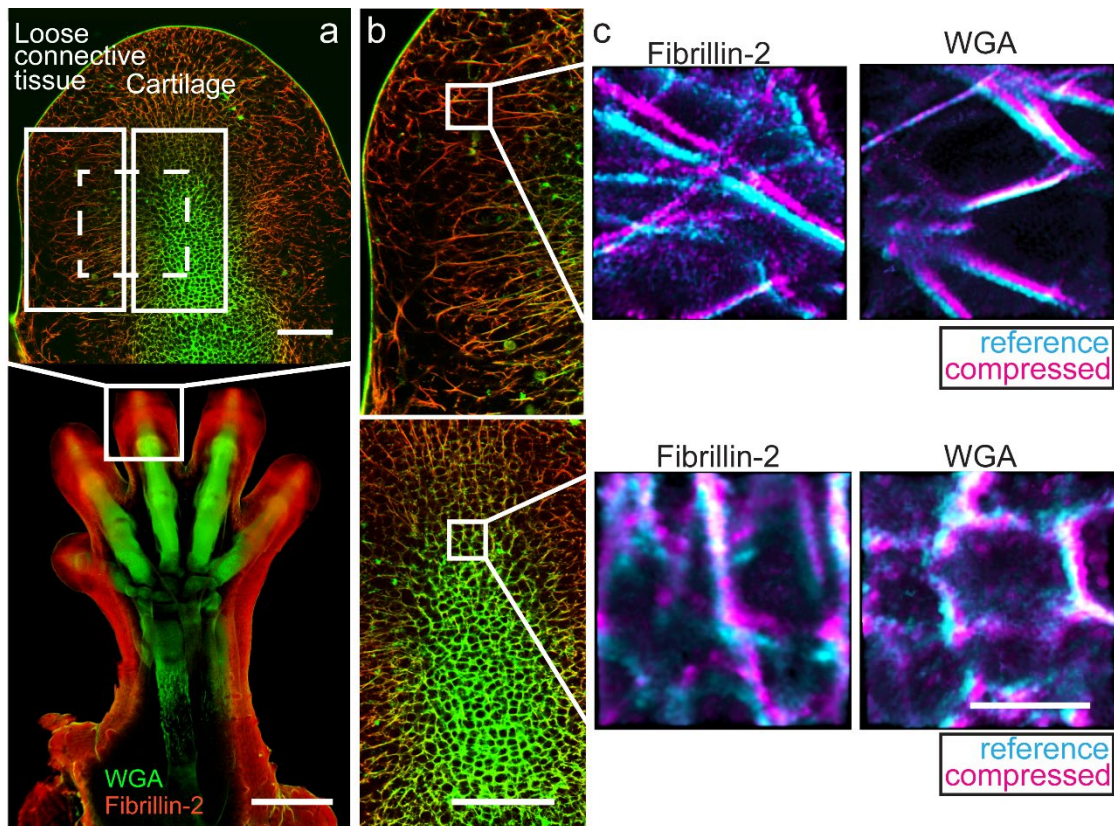


Figure 3.2. Representative confocal images of a decellularized murine forelimb. **a.** Global confocal image of the developing forelimb stained with wheat germ agglutinin (WGA; green) and for fibrillin-2 (red) at 10 $\times$  (bottom; scale bar = 500  $\mu$ m) and at 25 $\times$ , focusing on the distal phalange (top; scale bar = 100  $\mu$ m). The location of the cartilage and the adjacent loose connective tissue are boxed and labeled in white. Dashed box (white) represents the area analyzed when quantifying regional differences, including both cartilage and the adjacent loose connective tissue in the same sub-stack. **b.** Composite images of the loose connective tissue (top) and the cartilage (bottom), indicating the spatial distribution of fibrillin-2 (red) and WGA (green) (scale bar = 100  $\mu$ m). **c.** Composite images of a representative sub-stack in the loose connective tissue (top) and the cartilage (bottom) corresponding to fibrillin-2 (left) and WGA (right), showing an overlay of the reference (cyan) and compressed (magenta) (scale bar = 10  $\mu$ m).

### ***Digital volume correlation***

Image stacks were imported into MATLAB R2017b (MathWorks) as 3D arrays of 8-bit intensity values. The intensity arrays of the reference and compressed configurations were compared using the MATLAB-based FIDVC algorithm developed by Bar-Kochba *et al.*, to extract the displacement fields of the ECM networks<sup>116</sup>. Displacements components  $u_x$ ,  $u_y$ ,  $u_z$ , were calculated for a grid of material points evenly spaced every 8 pixels along XYZ, corresponding to voxels of  $0.68 \times 0.68 \times 0.94 \mu\text{m}^3$  for the  $22 \times 22 \times 15 \mu\text{m}^3$  sub-stacks, and  $0.78 \times 0.78 \times 0.94 \mu\text{m}^3$  for the larger  $188 \times 188 \times 15 \mu\text{m}^3$  sub-stacks. Voxels in the regional sub-stacks had a slightly lower

resolution due to the higher computational demands of processing these larger images. The features in the ECM networks of interest are  $<1 \mu\text{m}$  in diameter and thus the voxel dimensions of both regions remain smaller than the features we are trying to characterize. In addition to  $u_x$ ,  $u_y$ , and  $u_z$ , a cross correlation coefficient array was generated that quantitatively defined how well the intensity distribution mapped between the two configurations. Areas of low intensity, i.e. where there was no ECM, do not correlate well, leading to large erroneous displacements and small cross-correlation coefficients. The displacement arrays were processed using a 3D Gaussian filter, and then areas that had a cross-correlation coefficient lower than 0.001 were removed, to eliminate aberrant displacements.

### ***Displacement analysis***

Network displacements were analyzed by plotting the normalized number of fibril voxels as a function of displacement magnitude  $|u|$  to compare the distribution of displacements among proteins and geometries. Displacement was only considered in voxels corresponding to ECM based on the intensity profile of each pair of correlated images. This avoided the quantification of displacements in regions not corresponding to the ECM networks, since they often have low cross correlation coefficients and may correspond to erroneous displacements. Vector fields representing displacement components and magnitude were plotted in 3D using MATLAB, as a qualitative metric of ECM deformation (**Figs. 3.1, 3.3, 3.4**).

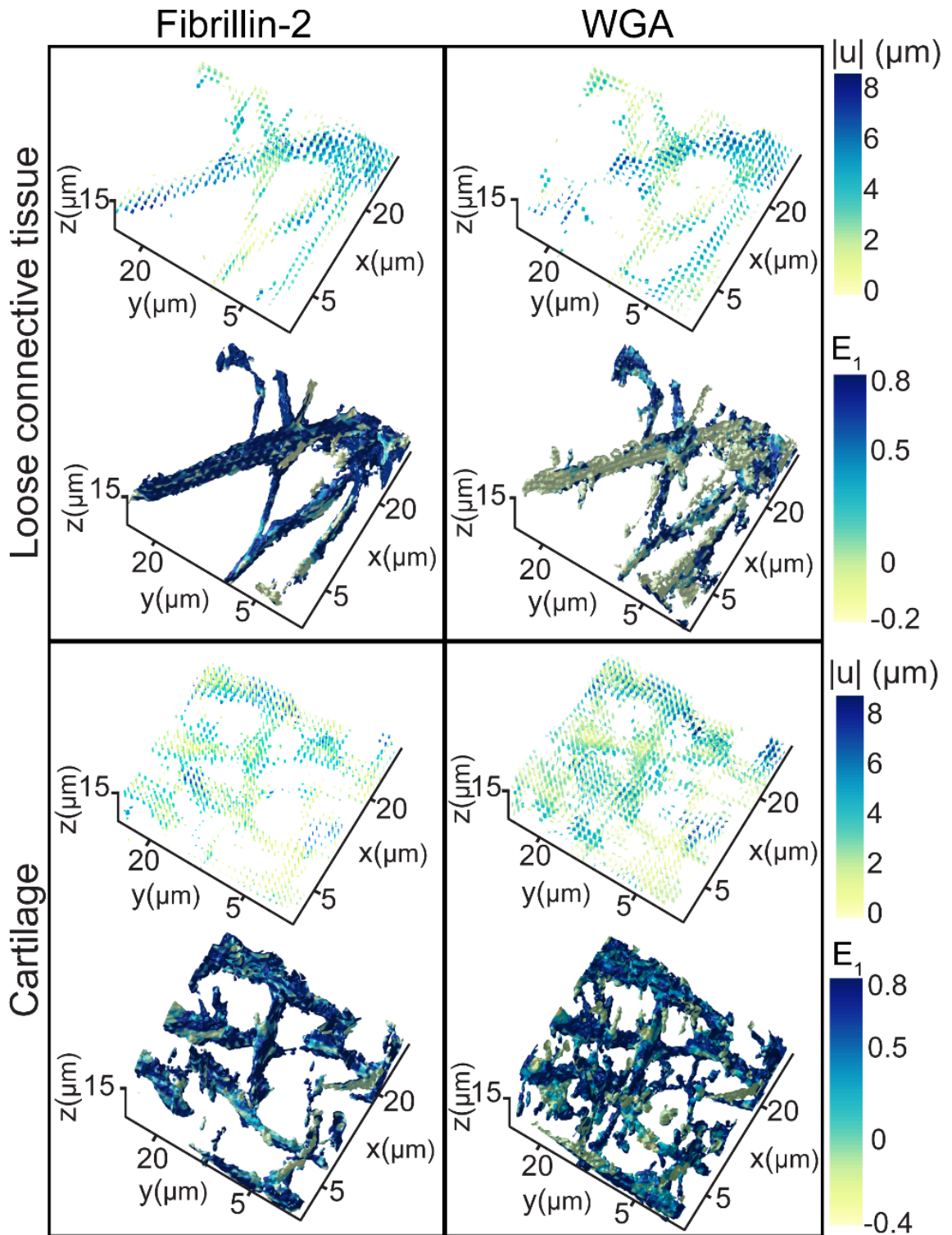


Figure 3.3. Representative deformation response from sample B for WGA and fibrillin-2 sub-stacks of  $22 \times 22 \times 15 \mu\text{m}^3$  in the cartilage and loose connective tissue. Displacements are represented as vector fields with color representing magnitude from 0 to 8  $\mu\text{m}$ . Maximum principal strain ( $E_1$ ) is shown on the surface of the segmented ECM networks with color representing magnitude ranging from -0.4 to 0.8.

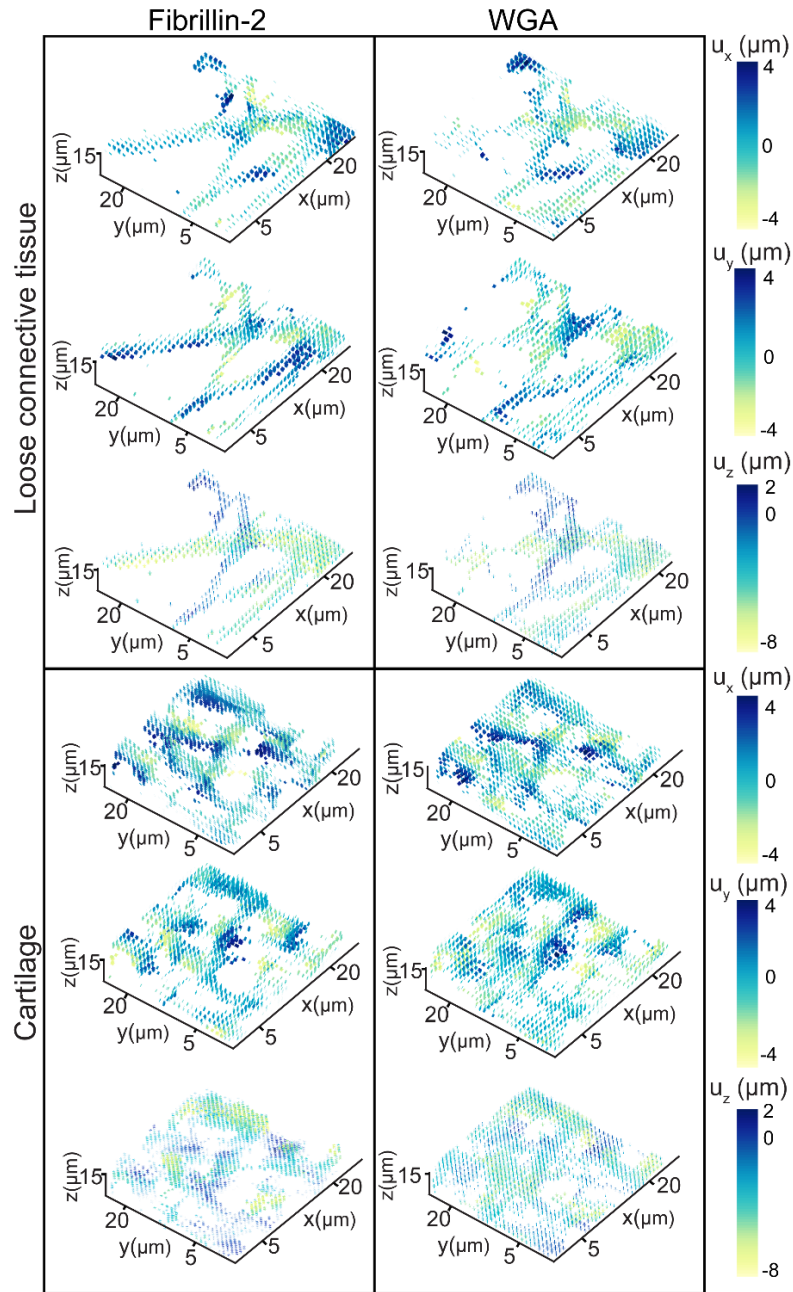


Figure 3.4. Displacement fields for representative ECM sub-stacks from sample B.  $u_x$ ,  $u_y$ , and  $u_z$  were plotted for FBN2 and WGA in the loose connective tissue (top) and the cartilage (bottom) regions with color indicating magnitude and directionality of displacement.

### 3.3.3 Validating fibril displacements

To confirm that random motion of the network does not influence displacement measurements, control samples without a load applied were imaged  $2\times$ , with 15 minutes in

between acquisition of each stack. The two pairs of z-stacks were compared with FIDVC as described above.

### ***Sample fabrication***

The compression-induced displacements of fluorescent particles in fibrin gels obtained with FIDVC were compared to those calculated using the *TrackMate* plug-in, as a control (FIJI)<sup>117</sup>. Fibrin gels were composed of human thrombin (Enzyme Research Laboratories), human fibrinogen (Enzyme Research Laboratories), AF488-conjugated fibrinogen (ThermoFisher), and Fluoro-Max Dyed Blue Aqueous Fluorescent Particles (ThermoFisher; diameter: 0.5  $\mu\text{m}$ ; concentration: 1% solids;). In brief, the fibrin gels were prepared by combining 5.7  $\mu\text{L}$  human fibrinogen (14.15 mg/mL stock in 20 mM sodium citrate-HCl/ pH 7.4), 20  $\mu\text{L}$  fluorophore-conjugated fibrinogen (1 mg/mL stock in 0.1 M sodium bicarbonate/pH 8.3), 1.0  $\mu\text{L}$  calcium chloride (2M in Milli-Q), and 73.3  $\mu\text{L}$  PBS. The solution was briefly vortexed, combined with 1  $\mu\text{L}$  of the fluorescent particle working solution (1:10 in PBS), then vortexed again for 1 second. Then, 5  $\mu\text{L}$  of thrombin solution (0.01 u/ $\mu\text{L}$  in Milli-Q) were added and the combined solution was again briefly vortexed. Approximately 100  $\mu\text{L}$  of the resulting solution were pipetted into three equally sized droplets of fibrin in a 50-mm glass bottom petri dish. In preparation for compression experiments and to facilitate the polymerization of the gels into a cylindrical shape, supports made of PDMS were placed on either side of the droplets and a circular glass coverslip was placed over them. Light pressure was applied to ensure the top of the gels adhered to the coverslip. The dish was then covered to protect the gels from light and left to polymerize for 10 minutes on the bench. To prevent the gels from drying out, PBS was gently added to their surrounding space.

### ***Image acquisition and analysis***

The fibrin gels were imaged using an inverted Zeiss LSM 880 confocal microscope using a 10 $\times$  EC-Plan NeoFluar (NA = 0.3) objective. An 850 $\times$ 850  $\mu\text{m}^2$  area was selected for imaging based on visibility and quality of fibrils and fluorescent particles. Reference z-stacks, composed of 12 slices with  $\Delta z = 5\mu\text{m}$ , were acquired. After the reference z-stacks were acquired, a weight of 27g was placed on the center of the glass plate and left to equilibrate for 15 minutes before imaging the compressed configuration. The z-stacks were then processed using FIJI to despeckle and remove outliers. The *Remove Outliers* feature was used to remove small bright pixels that

were significantly smaller than the fluorescent particle dimensions. *TrackMate* was used to analyze the images by calculating the  $u_{xy}$  displacement of the fluorescent particles before and after compression of the gel, based on particle size and track quality. The obtained data was exported into MATLAB and the displacement magnitudes ( $|u_{xy}|$ ) were plotted as vector fields. Volume images were also processed as described in the previous section and compared with FIDVC to extract the displacements of the fluorescent particles.

### ***Displacement error calculation***

The FIDVC displacement values corresponding to those of fluorescent particles tracked by *TrackMate* were used to calculate the absolute error, by subtracting the *TrackMate* displacements from those obtained with FIDVC (**Fig. 3.7**). The location of the displacements calculated with FIDVC was found using the MATLAB function *findpeaks*. For each of the 4 fibrin gel compression experiments conducted, the average and standard deviation of the absolute error values were calculated for both the upper and lower half of the analyzed volume images, to investigate if z-position in the sample influenced the absolute displacement error. Further, the displacement field of the fluorescent particles and the fibrin fibrils in a sample were plotted (**Fig. 3.7c**). The difference between the FIDVC displacements of fibrils and fluorescent particles within the same volume was calculated to compare how well the algorithm tracked components of different geometries (**Fig. 3.7d**).

### **3.3.4 Calculation of the Green-Lagrange strain tensor**

The components of the Green-Lagrange strain tensor were calculated for the image volume from the FIDVC displacement components  $u_x$ ,  $u_y$ ,  $u_z$ , for a grid of material points evenly spaced based on the image resolution. The deformation gradient and the Green-Lagrange strain tensors at each grid point were calculated as:

$$\mathbf{F} = \begin{bmatrix} 1 + u_{x,x} & u_{x,y} & u_{x,z} \\ u_{y,x} & 1 + u_{y,y} & u_{y,z} \\ u_{z,x} & u_{z,y} & 1 + u_{z,z} \end{bmatrix} \quad (3.1)$$

$$\mathbf{E} = \frac{1}{2}(\mathbf{F}^T \mathbf{F} - \mathbf{I}) \quad (3.2)$$

where  $\mathbf{I}$  is the identity tensor. The partial derivatives of the displacement components were calculated by fitting a polynomial across  $x$ ,  $y$ , and  $z$  (**Fig. 3.1**) and analytically evaluating the derivative<sup>118</sup>. Here, displacement components included all values prior to elimination of those corresponding to low correlation coefficients and noise, in order to keep the interpolation functions from operating over large regions of blank space. The polynomial order was selected based on the norm of the residuals corresponding to polynomials orders 2-15. The 12<sup>th</sup> order polynomial provided the optimal fit, and a comparison of representative displacement components and the corresponding polynomial functions is shown in **Fig. 3.9**. The maximum principal strain,  $E_1$ , was calculated by determining the eigenvalues of  $\underline{\mathbf{E}}$  in MATLAB. ECM strain was calculated in three sub-regions ( $22 \times 22 \times 15 \mu\text{m}^3$ , each) within LCT and cartilage as well as in the larger network sub-stacks ( $188 \times 188 \times 15 \mu\text{m}^3$ ) for each protein. For visualization purposes, representative sub-stacks were segmented in MATLAB, based on the image intensity array, and the networks were rendered in 3D using a colorimetric scale to represent the magnitude of  $E_1$  across the volume (**Figs. 3.3, 3.5**). Information on the ECM geometry was used to selectively segment regions corresponding to continuous structures in the LCT or cartilage and a threshold was set to prevent the 3D segmentation of small floating elements<sup>94,119–121</sup>.

### ***Strain analysis and statistics***

Average ECM network strain for each  $22 \times 22 \times 15 \mu\text{m}^3$  sub-stack was calculated to compare the response of different proteins and regions to the applied load. The average maximum principal strain was used a metric to compare across proteins and geometries (LCT-FBN2; LCT-WGA; cartilage-FBN2; cartilage-WGA) since the 3D reconstructions are unable to show the internal strains, are subject to visual interpretation, and only represent the values at the surface. Therefore, the average maximum principal strains are a more representative and informative metric of the ECM network deformation across proteins and tissue types. Prior to the calculation of their average, strain values were subjected to a 3D Gaussian filter. Strain values greater than 1 or less than -1 were not included in the average calculation since these outliers represented <2% of each component of the Green-Lagrange strain tensor. Further, strain values corresponding to small, floating elements were not included in the ECM network segmentations.

Averages and the corresponding standard deviations were calculated using MATLAB and then plotted with GraphPad Prism 7.03 (GraphPad Software). A two-way ANOVA was performed

using GraphPad Prism,  $\alpha=0.05$ , to determine if the normal components of the Green-Lagrange strain tensor,  $E_{xx}$ ,  $E_{yy}$ ,  $E_{zz}$ , and  $E_1$  significantly vary as a function of protein and region. A post-hoc Tukey HSD test was used to identify significant differences between groups. The same approach was taken in analyzing  $E_1$  corresponding to the ECM networks in the  $188 \times 188 \times 15 \mu\text{m}^3$  sub-stacks. Average regional (LCT, cartilage)  $E_1$  were calculated for each protein (FBN2, WGA). Then,  $E_1$  averages were combined by group (LCT-FBN2; LCT-WGA; cartilage-FBN2; cartilage-WGA) across 5 samples by calculating their mean and standard deviation (**Fig. 3.5b**). A two-way ANOVA was performed using GraphPad Prism,  $\alpha=0.05$ , to determine if  $E_1$  significantly varied as a function of protein and region.

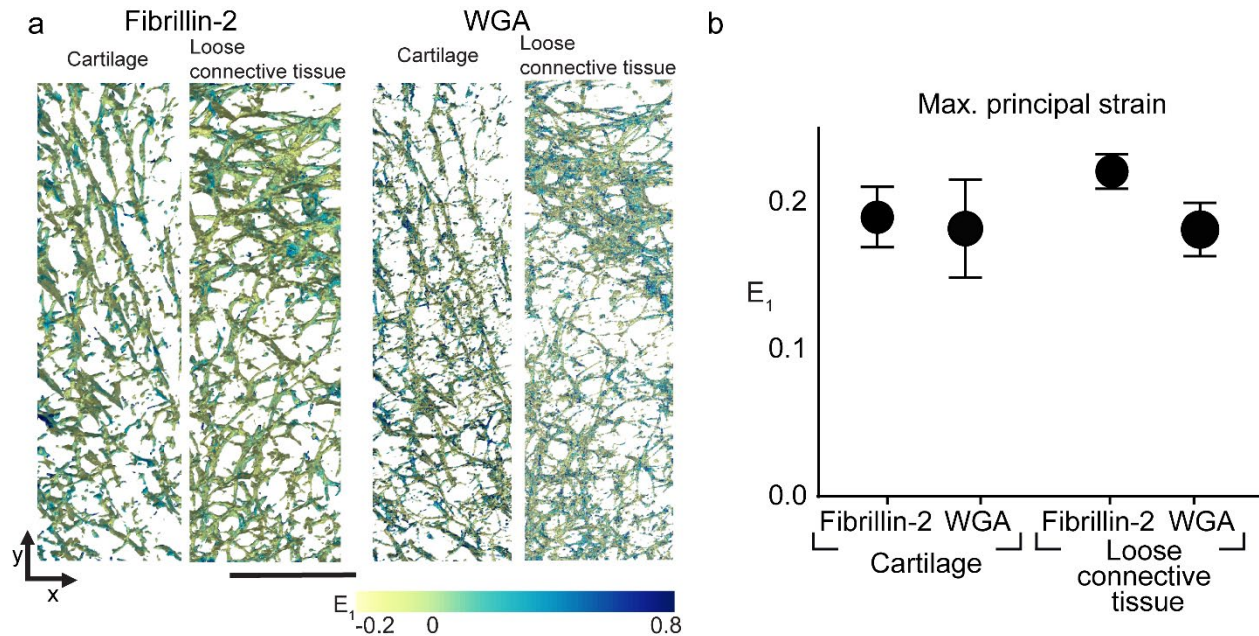


Figure 3.5. Comparison of maximum principal strain ( $E_1$ ) from large ECM networks. **a**. Representative ECM networks fibrillin-2 (left) and WGA (right) segmented in 3D with color representing the magnitude of  $E_1$  (scale bar=50  $\mu\text{m}$ ). **b**. Average  $E_1$  for each protein in each region from the large ECM networks across 5 different embryonic samples is dependent on protein ( $p \leq 0.032$ , two-way ANOVA). Tukey post-hoc comparison did not show significant differences between individual groups ( $n=5$ ; bar =S.D.).

## 3.4 Results

### 3.4.1 Fibril deformation

Our method presents an opportunity to investigate and define the material behavior of the ECM in the native 3D configuration. By first decellularizing embryonic tissues and maintaining their structural integrity, we can visualize the 3D geometry of independent ECM networks, before and after loading. E14.5 embryonic forelimbs were stained for FBN2, an ECM component that is found in microfibrils and elastin. Samples were counterstained with fluorophore-conjugated WGA, a lectin that selectively binds to n-acetyl glucosamine and sialic acid, labeling a subset of proteoglycans in the ECM. For brevity, the two networks are referred to as FBN2 and WGA.

Correlation of the reference and compressed configurations using FIDVC showed that the displacements of the ECM networks were heterogeneous in both the cartilage and LCT (**Fig. 3.3**). Since similar displacements are seen across samples, only those corresponding to sample B are shown as representative displacement fields (**Figs. 3.3, 3.4**). In both samples, displacements were the greatest in the direction of load ( $-z$ ). However, displacements of the same order of magnitude were seen in the  $xy$  plane in the opposite direction, due to the Poisson effect (**Fig. 3.4**). In the cartilage region, the displacement components ( $u_x$ ,  $u_y$ ,  $u_z$ ) and the displacement magnitude ( $|u|$ ) for FBN2 and WGA had similar distributions (**Figs. 3.3, 3.4**). The locations of maximal displacement varied between FBN2 and WGA; potentially due to differences in the spatial distribution of each ECM network's fibrillar structures, how these structures are interacting with each other, crosslinks between them, and chain entanglement. On the contrary, FBN2 and WGA in LCT exhibited different deformation profiles (**Figs. 3.3, 3.4**). Greater displacements were seen in the FBN2 fibrils than the WGA-stained proteoglycans (**Fig. 3.3**), potentially related to the length between the components of the two networks.

### 3.4.2 Fibril strain

#### *ECM sub-regions*

After correlation of the reference and compressed image volumes with FIDVC, ECM strain in situ was obtained by calculating the partial derivatives of the displacement components. Similar trends in maximum principal strain,  $E_1$ , and the normal strains of  $\mathbf{E}$  were observed in the two different samples (**Figs. 3.6, 3.8**). Sample B had slightly higher maximum principal strains than

Sample A, which might be due to slight differences in ECM spatial distribution and z-location of the analyzed  $22 \times 22 \times 15 \mu\text{m}^3$  sub-regions between samples. The heterogeneous geometry of the forelimb might also be causing these differences. For Sample A, both protein ( $0.0021 < p \leq 0.032$ ) and region (*i.e.* LCT, cartilage) ( $0.0002 < p \leq 0.0021$ ) had a significant effect on the average  $E_1$ , as found by two-way ANOVA. Protein composition significantly influenced  $E_1$  in the cartilage sub-regions ( $0.0021 < p \leq 0.032$ ). In LCT, FBN2 had a significantly higher  $E_1$  than WGA ( $0.0002 < p \leq 0.0021$ ) (**Figs. 3.3, 3.6**). For Sample B, only the protein was found to have a significant effect on  $E_1$  ( $p \leq 0.0002$ ) and similar trends were observed for both  $E_1$  and the normal strains (**Figs. 3.6, 3.8a**). The region of interest had a significant effect on the average  $E_{xx}$  and  $E_{yy}$  ( $p \leq 0.032$ ; **Fig. 3.8a**).  $E_{zz}$  was larger than  $E_{xx}$  and  $E_{yy}$  in both samples, which is consistent with  $u_z$  being greater than  $u_x$  and  $u_y$  regardless of protein and region (**Figs. 3.4, 3.8a**). The shear strains of both samples were lower than the normal strains and  $E_1$ , ranging from -0.014 to 0.018, for both samples (**Fig. 3.8b**). This indicates that the predominant mode of loading was axial since the ECM is not undergoing large shear distortion in any two directions.

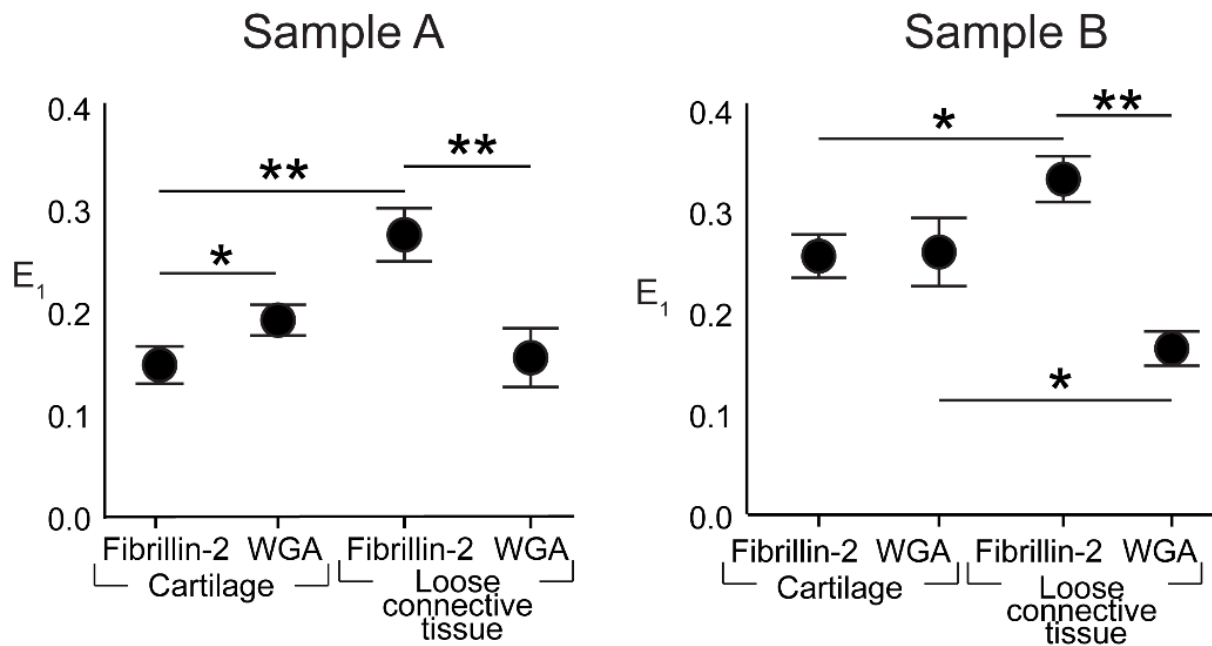


Figure 3.6. Comparison of independent samples reveals similar trends in ECM strain profiles. Maximum principal strain ( $E_1$ ) for sample A (left) and sample B (right) was dependent on both protein and region ( $p \leq 0.0021$ ;  $p \leq 0.032$ , respectively, two-way ANOVA). Tukey post-hoc comparison showed significant differences between individual groups ( $*0.0021 < p \leq 0.032$ ;  $**0.0002 < p \leq 0.0021$ ) ( $n=3$ ; bars = S.D.).

### ECM networks

To minimize any bias introduced via the sub-region selection process, larger areas encompassing both cartilage and LCT were analyzed. Similar trends were observed as in the smaller sub-regions, though the differences between protein and tissue type were attenuated. The regional  $E_1$  averages for each protein (FBN2, WGA) from large ECM network sub-stacks ( $188 \times 188 \times 15 \mu\text{m}^3$ ) across 5 different embryonic samples, showed similar trends (**Fig. 3.5**). Protein type was found to significantly affect the average  $E_1$  ( $p \leq 0.032$ ). Notably, FBN2 in LCT had a substantially, but not significantly, higher  $E_1$  average than WGA ( $p = 0.0564$ ), consistent with the sub-region analysis. Small standard deviations in the strain values across samples, indicate the repeatability of this technique.

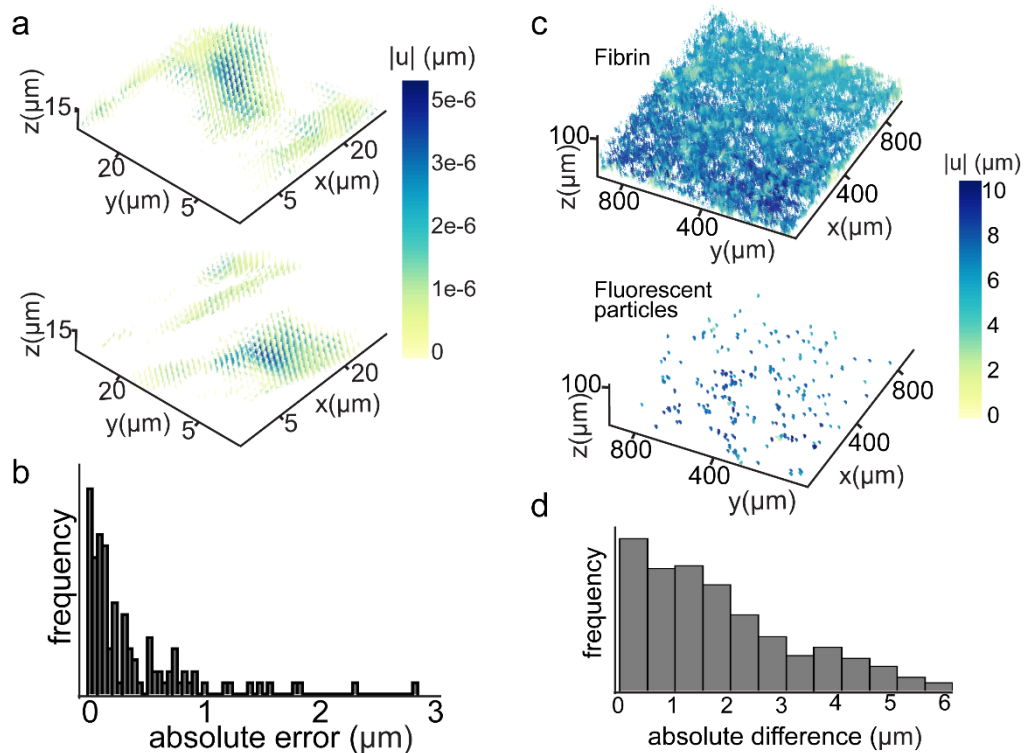


Figure 3.7. Error quantification and analysis. **a**. Representative displacement vector field resulting from the fast-iterative digital volume correlation (FIDVC) of the same configuration imaged twice, without the application of load for WGA (top) and FBN2 (bottom). Displacement magnitude (in the order of picometers) is shown with color in the vector field. **b**. Representative absolute displacement error distribution for fibrin gel compression experiment and FIDVC. **c**. Displacement fields of the fibrils (top) and the fluorescent particles (bottom) in the fibrin gels generated for FIDVC displacement validation. **d**. Representative absolute difference between the FIDVC-calculated displacement of fluorescent particles and the adjacent fibrils.

### 3.4.3 Displacement error

After imaging control samples without a load applied  $2\times$ , the displacements resulting from FIDVC indicate that there is minimal noise in our system (**Fig. 3.7a**). The *TrackMate* plug-in (FIJI) was used as a control to validate the displacements obtained with FIDVC. *TrackMate* and FIDVC lead to similar vector fields, however, there are significantly fewer data points in the field resulting from *TrackMate*. This is potentially due to the tracking parameters we have established and the particle size we have selected as a target. There are many fluorescent particles that are not tracked by *TrackMate*, yet they are accounted for with FIDVC. For instance, there were only 117 particles tracked by *TrackMate*, while FIDVC leads to 295 non-zero displacement magnitudes in a representative sample. Nonetheless,  $>90\%$  of the absolute error values are less than 10% of the maximum displacement ( $10\ \mu\text{m}$ ), while the average displacement was  $6.67\ \mu\text{m}$ . Displacement magnitudes ( $xy$ ) calculated with FIDVC appeared to be an overestimate of those calculated with *TrackMate*. The average for the absolute error across compression experiments seems to be consistent (**Fig. 3.7b**). Standard deviations remain in the same order of magnitude as the absolute error average across samples (**Table 3.1**). Furthermore, the z-position of the tracked displacements appears to influence the absolute displacement error values, as shown in **Table 3.1**. In addition, the displacement of both particles and fibrils in the same sample were calculated with FIDVC, showing good agreement between components of different geometries (**Figs. 3.7c, 3.7d**).

## 3.5 Discussion

The results presented here demonstrate the unique ability of our method to resolve and quantify 3D geometry-specific ECM deformation and strain. Characterizing ECM network deformation is possible through confocal microscopy of immunostained, decellularized embryonic tissues before and after mechanical loading. During embryonic development, the ECM architecture is less dense, making it easier to visualize and manipulate compared to most adult tissues that are denser with individual networks that are difficult to resolve. Image processing and FIDVC algorithms were used to extract the displacement and strain fields of 3D networks. This allowed us to resolve geometry-specific strains of independent ECM when a load was applied to the entire tissue sample. There are some key limitations to the presented method and its resulting conclusions.

Nevertheless, the development of a methodology to quantify strain is a critical first step towards characterizing the material behavior of different ECM networks *in situ*.

The steps taken to visualize the 3D geometry of the ECM may influence the mechanical properties of the samples. Treatment with SDS has been confirmed to not interfere with the spatial organization of the ECM. However, detergents may disrupt these fibrillar structures if delicate embryonic samples are decellularized for too long. Since visual inspection is subjective, it is best to limit the time that the samples are submerged in detergents to 3-5 days. Although the tissues were fixed with PFA, which might increase intrafibrillar crosslinking, previous work showed that the bulk tissue mechanics were not significantly altered. Furthermore, the presence of a polyacrylamide framework likely influences ECM deformation since it increases the overall rigidity of the embryonic tissue and may deform differently. Unfortunately, the 3D organization and spatial distribution of the polyacrylamide framework could not be resolved, confounding our ability to elucidate potential interactions with the ECM structures we characterized. Future work will analyze ECM strain in decellularized embryonic tissues without the polyacrylamide support to quantify the influence of this framework.

Several imaging parameters should be considered when calculating compression induced ECM strain. First, a suitable z-resolution must be allowed by selecting a z-step size that is smaller than the features of interest. In this work, the individual ECM fibrillar structures were  $<1\ \mu\text{m}$  in diameter, whereas, the step size between z-slices was  $1.23\ \mu\text{m}$ . This discrepancy could lead to an overestimation of the ECM dimensions in the z-direction resulting in an underestimation of strain. Further, the values obtained for displacement and strain could have been influenced by the z-position of the imaging planes within the E14.5 forelimb due to the heterogeneous spatial distribution of the ECM in the developing cartilage and its adjacent connective tissue. The consistent selection of ECM features to use as landmarks for imaging of the reference and compressed configurations was crucial for obtaining comparable results. Future work will generate datasets with smaller step sizes to determine the effect of z-resolution on compressive strain distribution. Additionally, a sensitivity analysis will be needed to ensure strain values are independent of imaging parameters, particularly in the z-direction.

The heterogeneous geometry of the forelimb challenged the application of a normal load that remained perpendicular during imaging. This was solved by using a PDMS loading well that constrained the weight from moving and potentially translating the samples. To minimize the

effect of biological variability might have on forelimb dimensions, all litters were harvested at noon to obtain samples at a consistent stage of embryonic development (E14.5). All samples were oriented dorsal side up and the same region of the distal phalanx of the third digit was imaged on all forelimbs. Despite potential sample to sample variability, the maximum principal strain averaged over 5 different biological replicates showed similar trends and a significant difference in  $E_1$  between ECM (**Fig. 3.5**). The heterogeneous and spatially dependent distribution of the ECM in the developing forelimb was the basis for the selection of this tissue, given our objective to resolve quantitative differences in the strain experienced by different proteins as a function of tissue type (*e.g.* cartilage, LCT). Since the proteins have different 3D organizations, the observed stiffness, or resistance to deformation, is likely related to both variations in geometry and material behavior; however due to the heterogeneous geometry of the samples, stress was not calculated in this study. Without thorough characterization of the geometry variability across both tissue samples and the ECM protein networks themselves, it was not possible to quantify the geometric effect from the strain differences due to material behavior. Future studies will focus on resolving these effects by utilizing samples with more homogenous geometries.

Confocal microscopy allowed for the acquisition of high-resolution images and to distinguish independent 3D networks. Small  $22 \times 22 \times 15 \mu\text{m}^3$  sub-stacks were selected to have greater control over the region and location of the investigated ECM components (*e.g.* fibrils) and their strain and deformation. The selection of small sub-stacks led to some drawbacks in data analysis, one of which was the up-sampling of data through image processing prior to FIDVC. As outlined in the Methods section, the number of pixels corresponding to these volume images was adjusted in FIJI through the *Resize* function, which resized images by interpolating pixel intensities. This interpolation resulted in more relevant image arrays than those created by repeating individual intensity values to adjust size. However, this can lead to sub-stacks consisting of primarily interpolated data, depending on where in the volume images they were selected. To mitigate the effect of small sub-stack location, larger sub-stacks of ECM networks across  $188 \times 188 \times 15 \mu\text{m}^3$  were analyzed. Notably, similar trends in protein and region strain were observed between the different sized data sets, indicating that our method of deriving strain from displacement worked on both small homogenous and larger heterogeneous geometries. The calculated strains suggest that WGA is stiffer than FBN2 in the LCT, while both proteins have similar stiffness in the cartilage configuration (**Fig. 3.6**). Alternatively, the differences in displacement distributions

between the cartilage and LCT could be due to the heterogeneous ECM organization, leading to region-dependent displacements. Future work will be needed to identify the ideal z-step size needed to more accurately calculate displacements without interpolation.

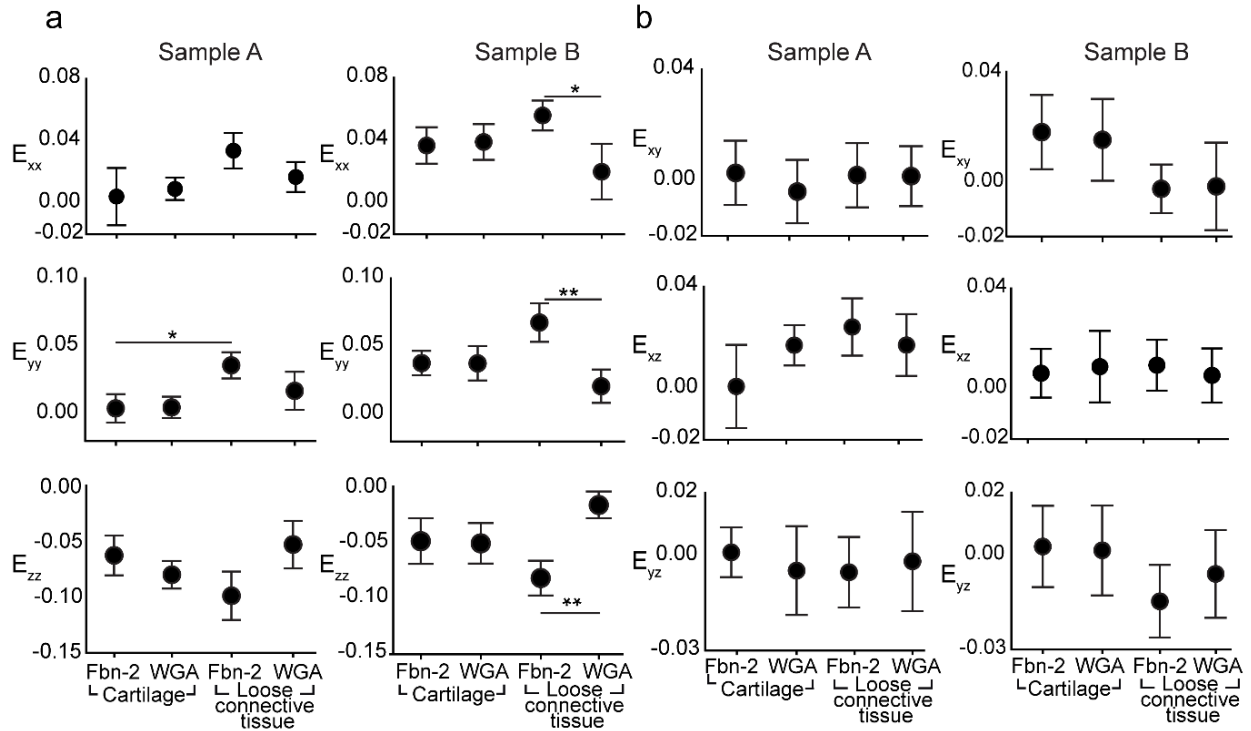


Figure 3.8. Comparison of Green-Lagrange strain components across independent samples. a. Significant differences between normal strains ( $E_{xx}$ ,  $E_{yy}$ ,  $E_{zz}$ ) across proteins and regions for sample A (left) and sample B (right) identified via a two-way ANOVA post-hoc Tukey test comparison are shown ( $*0.0021 < p \leq 0.032$ ;  $**0.0002 < p \leq 0.0021$ ) ( $n=3$ ; bars = S.D.), revealing similar trends in ECM strain profiles. b. Shear strain components ( $E_{xy}$ ,  $E_{xz}$ ,  $E_{yz}$ ) for sample A (left) and Sample B (right) ( $n = 3$ ; bars = S.D.).

Due to the nature of this fibrillar material, accurate measurement of individual strain tensor components using displacements derived from FIDVC will be challenging since these will be affected by fibril translation and specimen orientation. Representation of strain using invariants (e.g. principal strains) circumvents this issue and enables the comparison of the response of different ECM components to loading. However, to definitively determine if the displacements observed are due to changes in fibril length or simply network reorganization or translation, analysis of larger volumes that include features that can be used as fiduciary markers will be essential. These features, such as intra/inter-network cross-links, will be ECM and tissue dependent and will require high-resolution imaging over multiple time steps to identify if changes

in geometry are due to reorganization/translation or material deformation. Alternatively, artificial landmarks can be imposed on the fibrils by using techniques such as photobleaching. If uncertainty in determining variations in strain of individual fibril components persists even with high-resolution imaging, we will instead use overall network features to map tissue deformation and strain.

In accordance with Nyquist criterion, any analysis or calculations based on DVC should have voxel dimensions smaller than the features of interest in the images<sup>118,122,123</sup>. The individual ECM fibrillar structures in this work were  $< 1 \mu\text{m}$  in diameter. Given the tradeoff between imaging time, the resolution and working distance of the objectives used, and our computational capabilities, the study was limited by our image processing resources and the step size between z-slices was  $1.23 \mu\text{m}$ . The discrepancy between z-step and fibril dimensions could lead to an overestimation of ECM dimensions in the z-direction resulting in an underestimation of strain. Now that we established the feasibility for this pipeline to track fibrils within heterogeneous tissues before and after loading, our future studies will expand to include submicron-resolution analysis of large, full-field network images ( $\sim 400 \times 400 \times 100 \mu\text{m}^3$ ) with supercomputing resources. Additionally, a sensitivity analysis will be needed to ensure displacement values are independent of imaging parameters, particularly in the z-direction.

The choice of displacement as an intermediate step to calculate strain has a direct effect on the results. In this study, quantification of displacement allowed for the calculation of strain through polynomial fitting and the evaluation of analytical derivatives in as a function of  $xyz$  position (**Fig. 3.9**). As shown when plotting the FIDVC data and the displacement polynomial fit, the quality of the fits varies but overall showed a good representation of the data. Non-fibril displacements were included in the data the polynomial functions were fitted to due to a couple of reasons. First, there is an intensity gradient present between the ECM fibrils (bright) and the non-fibril space (dark). The changes in intensity between the bright fibrils and the dark non-fibril space varied depending on fibril geometry, orientation, and network 3D organization, in combination with the imaging parameters that might also be responsible for this gradient-like border defining the ECM fibrils. Therefore, eliminating the displacements on non-fibril spaces would potentially eliminate fibril displacements that are just below the threshold but are still relevant. More importantly, eliminating non-fibril displacements can introduce discontinuities when plotting the data and lead to a further interpolation between fibril displacements.

Table 3.1. FIDVC absolute displacement error

	$ u_{xy} $ ( $\mu\text{m}$ ) (upper half)	$ u_{xy} $ ( $\mu\text{m}$ ) (lower half)
<b>Fibrin gel compression 1</b>	$0.673 \pm 0.586$	$0.331 \pm 0.517$
<b>Fibrin gel compression 2</b>	$0.458 \pm 0.649$	$0.159 \pm 0.123$
<b>Fibrin gel compression 3</b>	$0.363 \pm 0.409$	$0.129 \pm 0.121$
<b>Fibrin gel compression 4</b>	$0.462 \pm 0.240$	$0.170 \pm 0.185$

Given the relationship between displacement and strain, it was of interest to validate displacements obtained with FIDVC and quantify the error pertaining to our imaging procedure (Fig. 3.7). By using fluorescent particles in a fibrin gel, we measured the displacement error related to FIDVC. The average absolute errors obtained were approximately an order of magnitude smaller than displacement due to compression; similar to previously reported FIDVC displacement errors. There appeared to be an influence of z-position in the absolute FIDVC error. This might be due to the nature of the compression experiments; the upper half of the fibrin gel was closer to the applied load, potentially leading to greater particle movement or making it more challenging for *TrackMate* to successfully track all present particles. The calculation of absolute error was limited to only the particles *TrackMate* could successfully track, and it did not involve displacement in the z-direction. Therefore, this meant that over half of the FIDVC displacements were not involved in the calculation of absolute error. Further, the FIDVC z-displacement error and its reliability are yet to be quantified in our hands.

The greatest displacement component was  $u_z$ , while the greatest strain component was  $E_{zz}$ , both of which correspond to the direction of the applied load (-z) (Figs. 3.3, 3.4). The results of FIDVC indicate a maximum displacement of  $8 \mu\text{m}$  in the direction of the load (Fig. 3.4). During imaging, landmarks used as guides for alignment were observed to also displace roughly  $6\text{-}8 \mu\text{m}$  due to compression. Discrepancies in the visual representations of displacement and strain were observed, potentially due to the choice of segmentation algorithm used to reconstruct ECM fibrillar network structures and visualize strain in 3D. These discrepancies might also depend on the number of material grid points fit to the polynomials. Further work will be conducted to fully characterize the effects of the number of material grid points and the segmentation algorithm.

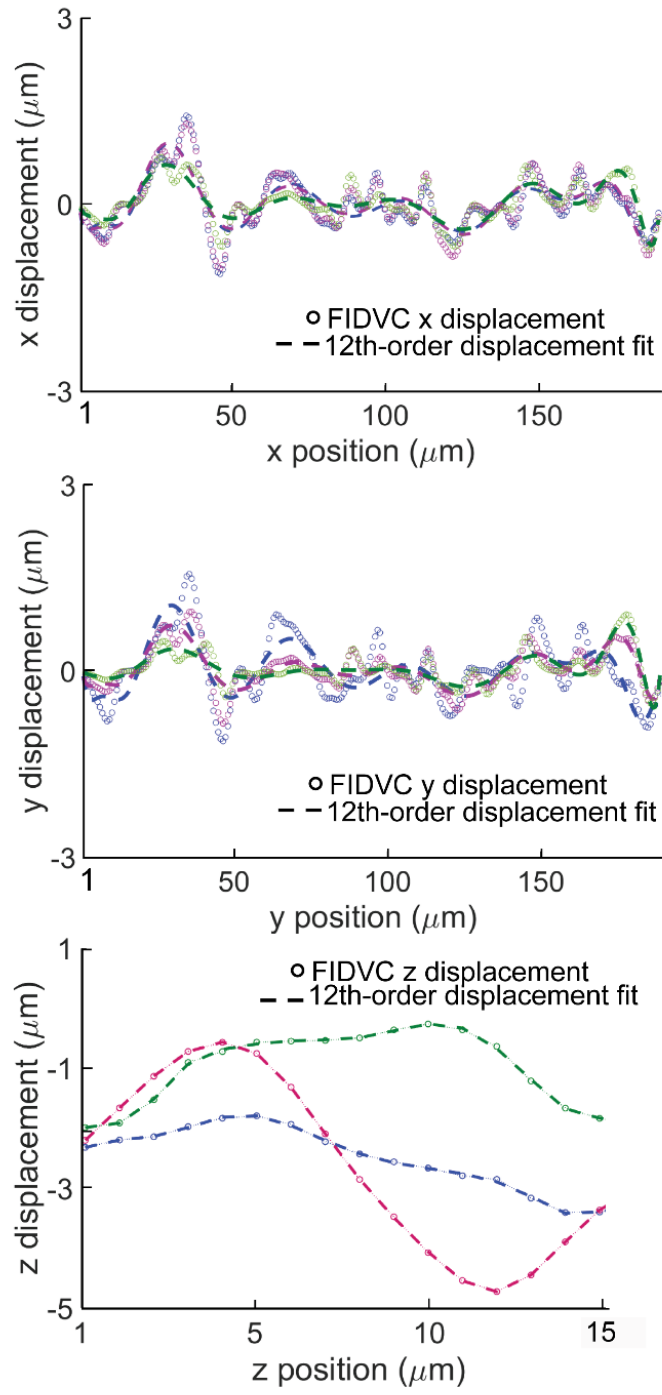


Figure 3.9. Gaussian filtered FIDVC displacement components at 3 representative positions (indicated by different colors) in sample B, including their corresponding polynomial fit. Negative z-displacements are in the direction of the applied load.

## 4. DESIGN AND VALIDATION OF A MODULAR MICRO-ROBOTIC SYSTEM FOR THE MECHANICAL CHARACTERIZATION OF SOFT TISSUES

This chapter is a draft of a manuscript currently in preparation for publication.

### 4.1 Abstract

Characterizing the mechanical properties of tissues is of interest to scientists looking to engineer tissues capable of restoring functionality. Tissues are primarily comprised of cells and the extracellular matrix (ECM), a dynamic network of macromolecules that regulates cellular behavior and provides a substrate for tissue structure and organization. Interactions between cells and the ECM contribute to the mechanical functionality of tissues. Mechanical characterization of tissues is vital for understanding the cellular microenvironment and defining design parameters for scaffolding with applications in regenerative medicine. When characterizing tissues that are loaded in tension *in vivo*, uniaxial loading is the appropriate and physiologically relevant modality. The mechanical characterization of soft and small tissues is challenging due to difficulties in manipulating samples with small dimensions and resolving forces of low magnitudes. There are few to no instruments able to test at the scale of nano (nN) and micronewtons ( $\mu\text{N}$ ). To address this gap, our goal was to develop a system that can perform tensile testing to characterize mechanical properties of soft biomaterials and small tissues. The modularity and adaptability of this system allowed us to couple it with a dissecting microscope in order to visualize tissue deformation during mechanical testing and thus facilitating the calculation of optical strain. Our data demonstrate the capability of the micromanipulator and spring system to resolve the force contribution of a sample of interest. This system can resolve a variety of mechanical responses and accommodate for several biologically relevant geometries and stiffnesses. Lastly, our system was used to investigate tendon mechanics, and was able to resolve an increase in tangent moduli as a function of development. This instrument can be further utilized to mechanically characterize

soft biomaterials and small tissues and provide physiologically-relevant design parameters for scaffolding that seek to emulate native tissue mechanics.

## 4.2 Introduction

Biological tissues perform a myriad of functions and vary broadly in composition and mechanical properties. Tissues are comprised of cells and the extracellular matrix (ECM), a dynamic network of macromolecules that regulates cellular behavior and provides a substrate for tissue structure and organization<sup>2</sup>. Interactions between cells and the ECM contribute to the mechanical functionality of tissues. Mechanical forces are among important factors that drive cellular function and organization. The mechanical properties of tissue change significantly with age and under different disease states and the identification of the mechanical properties of tissues on the macroscopic scale can be used in assessing the functionality of a soft tissue<sup>124–126</sup>. Therefore, the ability to uniaxially load tissues while taking force measurement is instrumental to probe material properties. The small size and susceptibility to damage of soft embryonic tissues and biomaterials limit the use of tensile testing instruments otherwise used for adult soft tissues. Further, there is difficulty in preparing and fixing samples of a few millimeters in length. Alternatively, AFM can be used to characterize tissues mechanically. We previously developed a novel technique to measure cell and ECM stiffness of viable developing tissues at the mesoscale using atomic force microscopy; yet, compression is not always a useful mode of testing tissues that undergo tensile loading *in vivo*<sup>2,14</sup>. Compression is the suitable testing modality for hydrogels and other biomaterials designed to withstand compressive forces, for instance, when seeking to recapitulate cartilage. However, connective tissues such as tendon are cyclically loaded in tension for the transfer of load from muscle to bone. Under compression, fibrils tend to buckle and are considered to have a negligible contribution to compressive tissue stress<sup>127–129</sup>. Further, cells exert tensile forces onto their surrounding microenvironment and thus ECM networks and fibrils are frequently uniaxially loaded *in vivo*<sup>7</sup>.

For the application of uniaxial loading, the mechanism used to securely grab the sample, the calculation of strain, and the resolution of the force sensor are important considerations depending on the size and stiffness of the samples to be tested. Examples of attachment techniques include serrated clamps, adhesives, suturing or winding with wire or thread depending on the tissue type<sup>71,130,131</sup>. Techniques used to fix soft tissues for mechanical testing can be grouped into the

following categories: modifying the clamp interface geometry, incorporating additional materials such as an adhesive, or modifying the specimen's mechanical properties in the clamped region for a better mechanical attachment<sup>130</sup>. Attaching soft biological samples via clamps or winding can be difficult due to low friction which can lead to slipping<sup>130,132,133</sup>. Further, small (~2 mm) samples may pose a challenge for some conventional attachment techniques like clamping, suturing and winding, if the equipment that is readily available is not sufficiently small for practical application. Besides sample attachment, strain calculation is another variable to consider. Strain is commonly calculated by measuring the displacement of the mechanical system itself, or by tracking the displacement of the sample of interest using optical surface markers<sup>134–136</sup>. One advantage of using optical markers (*e.g.* blue microspheres, graphite) is that the deformation of the sample is directly observed, avoiding errors attributed to the sample slipping out from its attachments. Digital image correlation algorithms are frequently used to track these optical markers and automate strain calculation during mechanical testing<sup>74</sup>. Alternatively, grip-to-grip strain is often calculated but cannot capture regional sample variations and is subjected to error in the case of slipping at the interface between tissue and the grips. In terms of force measurements and sample dimensions, biomaterials and soft tissues tested have ranged from 500  $\mu\text{m}$ <sup>137</sup> for a self-assembled biomaterial to 20 mm for adult rat Achilles and tail tendon fascicles<sup>135</sup>, for instance. The force threshold and resolution for uniaxial tensile tests can range from 11 nN<sup>137</sup> to 0.0025 N<sup>138</sup>, depending on the material properties and geometry of the tissue of interest.

The mechanical characterization of soft and small tissues is challenging due to difficulties in manipulating samples with small dimensions and resolving forces of low magnitudes. Further, mechanical interactions between cells and the ECM at the network scale contribute to the development and function of tissues at the macroscale<sup>1,139</sup>. However, the mechanical properties of multifunctional ECM polymers, like type I collagen, fibrin and fibronectin, and the mechanical influence of these polymers during tissue growth and remodeling is not completely understood. Mechanical characterization of tissues and ECM is vital for understanding the cellular microenvironment during growth and development and for defining design parameters for scaffolding with applications in regenerative medicine. To address this gap, our goal was to develop a system that can perform uniaxial tensile tests to characterize mechanical properties of soft biomaterials and small tissues by recording force measurements and visualizing samples for the calculation of optical strain. We adapted a commercially available micromanipulator system

using custom 3D printed springs and frames fabricated to accommodate a range of sample geometries and stiffness. Our system was able to resolve a variety of mechanical responses and assess tendon mechanics as a function of development. Embryonic tendons provide an ideal tissue to test with our system, given their loading *in vivo* and that they have the correct aspect ratio for uniaxial loading. Additionally, embryonic tendons are highly cellular and include low density ECM networks that we are interested in eventually characterizing.

### 4.3 Materials and Methods

#### 4.3.1 Development of a modular tensile testing system

A commercially available micromanipulator system (FT-RS1002, FemtoTools) and force sensing probes (FT-S10'000 and FT-S100'000, FemtoTools) were adapted for uniaxial loading of small, soft biological tissues and biomaterials. The micromanipulator system maneuvers in  $x$ ,  $y$ , and  $z$  directions with a displacement range of 5nm-26mm, and the microforce sensing probes resolve forces from 5nN – 100mN. In order to mechanically test a variety of soft tissues, custom springs and frames were designed and fabricated to accommodate a range of samples with varying geometries and stiffnesses (**Fig. 4.1**). Frames were drawn in Adobe Illustrator (Adobe Inc) and laser cut out of 100 $\mu$ m-thick polyethylene terephthalate (PET) using a Universal Laser VLS3.50. PET frames kept the samples in a static configuration and minimized damage while staining, processing and mounting onto the 3D printed springs. The spring and micromanipulator assembly were securely mounted onto an optical table using custom-built fixtures to avoid undesired part movement during testing and consequent system damage (**Fig. 4.1**). A dissecting microscope (M80, Leica Microsystems) was also mounted onto the optical table in order to visualize the sample during set-up and minimize damage, as well as for the calculation of optical strain.

Springs were designed using SolidWorks (Dassault Systèmes), 3D printed (ProJet MJP 2500) using UV curable plastic (M2R-CL, VisiJet), and post-processed following the manufacturer's guidelines. A liquid-retention basin incorporated into the spring design kept samples hydrated with PBS (**Fig. 4.1C**). The spring was connected to the micromanipulator system via a pillar that vertically offsets the microforce sensor, away from the PBS, to minimize risk of damaging electronics, serving as an interface between the rest of the hardware and the sample. The resolution on the 3D printer was not sufficient to create an interface with the desired dimensions

onto which the hook at the end of the microforce sensor probe could attach. Therefore, a small PET hook-interface was laser cut and adhered onto the Spring at the top of the pillar using Loctite Super Glue Gel Control. The PET hook interface was designed to facilitate attachment to the hooked probe at the end of the sensor. The SolidWorks simulation tool was used to perform finite element analyses to inform how geometric design changes would impact the function of the spring in order to expedite design iterations for new biological samples. Static simulations were executed to observe the stress and displacement responses to an applied force load. Assembly constraints were treated as bonded contact sets, material properties were defined for assembly components, and an external force load was applied to simulate the microforce sensor pulling on the spring (**Appendix A**). Simulations were run with and without a roller-slider fixture that would prevent the spring from moving out of the *XY* plane. Assembly components were treated as linear elastic isotropic materials with the following elastic moduli: frames and hook-interface [PET, 2,960 MPa], and microforce sensor [AISI 1035 Steel (SS), 205,000 MPa]. The elastic modulus for the 3D printing polymer, M2R-CL, listed by the manufacturer were 1,500-2,000 MPa. The elastic modulus of the M2R-CL 3D printed spring was calculated using the SolidWorks simulation tools and empirical data.

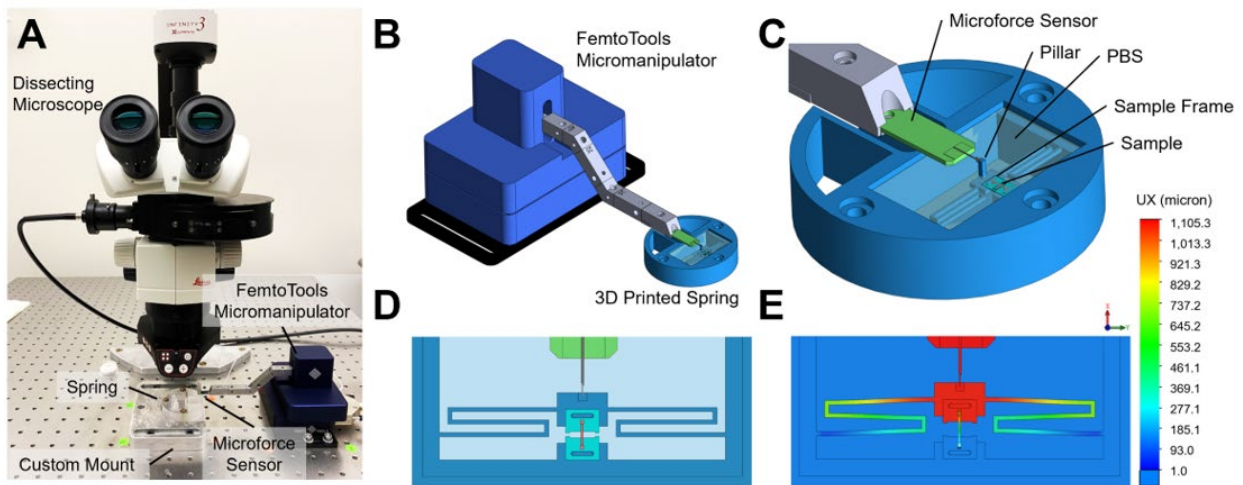


Figure 4.1. Schematic of mechanical resting set-up. **A.** Dissecting microscope and mechanical testing assembly **B.** FEMTOOLS micromanipulator and spring assembly. **C.** The microforce sensor has a custom probe that connects the micromanipulator to the spring, enabling the samples to remain hydrated in PBS. Samples are glued onto frames and loaded onto the spring. SolidWorks model of sample before **D** and during **E** tensile testing.

### ***Mechanical Testing Protocol***

PET frame-sample units were manually loaded onto the spring and cut with angled scissors prior to mechanical testing allowing the sample to extend freely during uniaxial loading. The length of each sample was measured optically to determine the appropriate speed to achieve the desired strain rate based on actuator displacement. Custom LabVIEW programs were written to control the movements of the micromanipulator and to automate testing by prescribing the direction, magnitude, and speed of displacement. Force measurements were recorded at 100Hz. The dissecting microscope magnification was adjusted to enable visualization of sample throughout testing. A camera (INFINITY3-3URC, Lumenera) was coupled to the scope for simultaneous video acquisition and mechanical testing. For  $2.5\times$  magnification, the region of interest (ROI) during video acquisition was  $6.2\times 4.7\text{ mm}^2$  and  $1936\times 1456$  pixels. The exposure time was adjusted for each sample to optimize contrast between the sample and fiducial lines using the camera's software package (INFINITY ANALYZE 6.5, Lumenera). Frame rate was dependent on exposure time and ranged from 3.4 to 7.2 frames per second. The contribution of the spring, or baseline, was measured prior to every test by recording the force vs. displacement of the spring in the system without a sample.

### ***Data analysis***

After tensile testing was completed, the baseline force readings (*i.e.* spring alone) were subtracted from the force recorded for each sample to isolate the force contribution of the material of interest. To calculate stress, the isolated force for each sample was divided by the cross-sectional area. The FIJI (NIH) *getSplineCoordinates* macro was modified and used to manually draw segmented polylines over the fiducial lines on each frame from the recorded video, each polyline was converted into a smoothed spline, and the  $x$  and  $y$  position of each point along the splines was output as an array on a .txt file. A custom MATLAB (MathWorks) algorithm was written to import the output arrays from FIJI and calculate the average distance between fiducial lines for each frame from the recorded video using the  $x$  and  $y$  coordinates from the FIJI output. Optical strain was calculated using the equation  $(L_i - L_0)/L_0$ , where  $L_0$  is the average distance between fiducial lines for the first frame of the video, and  $L_i$  is the average distance between fiducial lines for each subsequent frame (**Fig. 4.2**).

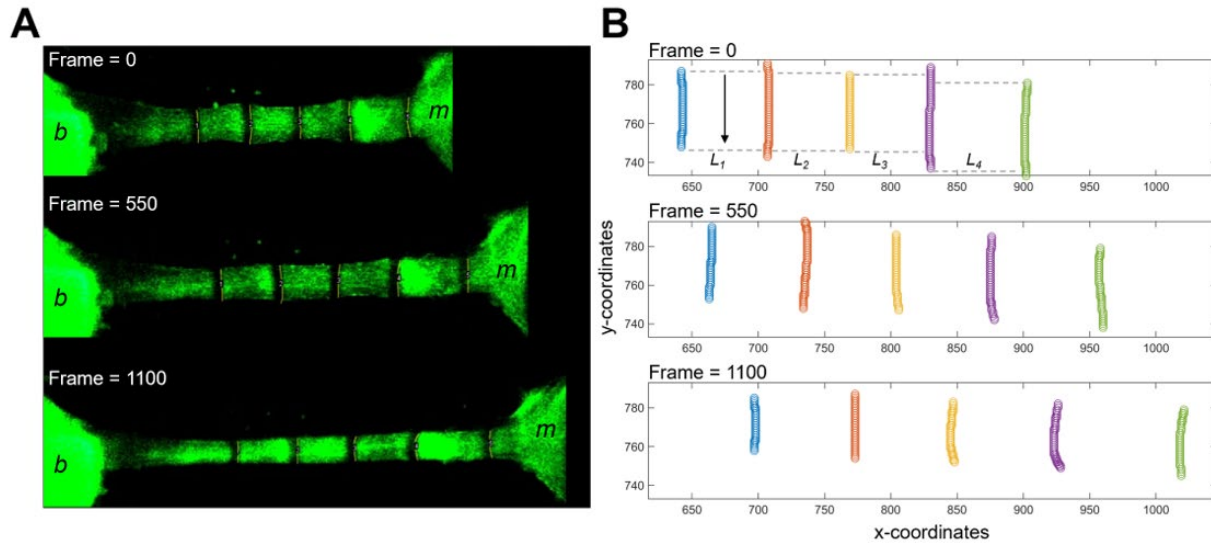


Figure 4.2. Strain calculations. **A.** A FIJI macro is used to manually trace the fiducial lines from frames of the recorded videos, and the X and Y coordinates of each manually drawn line is returned ( $b$ =bone insertion attached to the fixed end,  $m$ =muscle insertion attached to the movable end of the system). **B.** A MATLAB algorithm is used to measure the average horizontal distance between fiducial lines for each selected frame. Strain is calculated relative to the initial distance between fiducial lines.

An appropriate sampling rate (*i.e.* frame step size) for strain was selected based on the test's strain rate and video acquisition parameters. Since the acquisition rate for stress and strain data differed, the timestamps for both datasets were used to align stress with corresponding strain values. Briefly, using the video information, a time array corresponding to the strain datapoints was generated. The values in this array were then located in the stress time array to match stress and strain values, therefore, only stress values that aligned temporally with strain values were used. The stress and strain data were plotted, and curve fitting algorithms were used to describe it via a polynomial function.  $R^2$  values between second-degree and fourth-degree polynomial functions were compared, and the highest  $R^2$  value was selected as the most appropriate polynomial fit for the data. The derivative of the polynomial function at a selected strain value was used to calculate the tangent moduli at a specific strain value.

### 4.3.2 Sample preparation

#### *Developing tendons*

All murine experiments were approved by the Purdue Animal Care and Use Committee (PACUC; protocol 1209000723). PACUC ensures that all animal programs, procedures, and facilities at Purdue University adhere to the policies, recommendations, guidelines, and regulations of the USDA and the United States Public Health Service in accordance with the Animal Welfare Act and Purdue's Animal Welfare Assurance. C57BL/6 mice were time-mated to generate embryonic day (E)16.5, and E18.5 embryos, as well as postnatal day (P)0 pups. Dams were euthanized via CO<sub>2</sub> inhalation, which was confirmed using cervical dislocation. Embryos were removed from the uterine horns, rinsed in chilled 1× phosphate-buffered saline (PBS) and the hindlimbs were excised at the hip joint. Pups were euthanized by decapitation and the hindlimbs removed and placed in ice cold PBS. Tibialis anterior (TA) muscle-tendon-bone units were dissected by removing the skin with tweezers and then the surrounding connecting tissue with a blade under a dissecting microscope (DFC450, Leica Microsystems) to avoid tissue damage. The bone and muscle insertions were

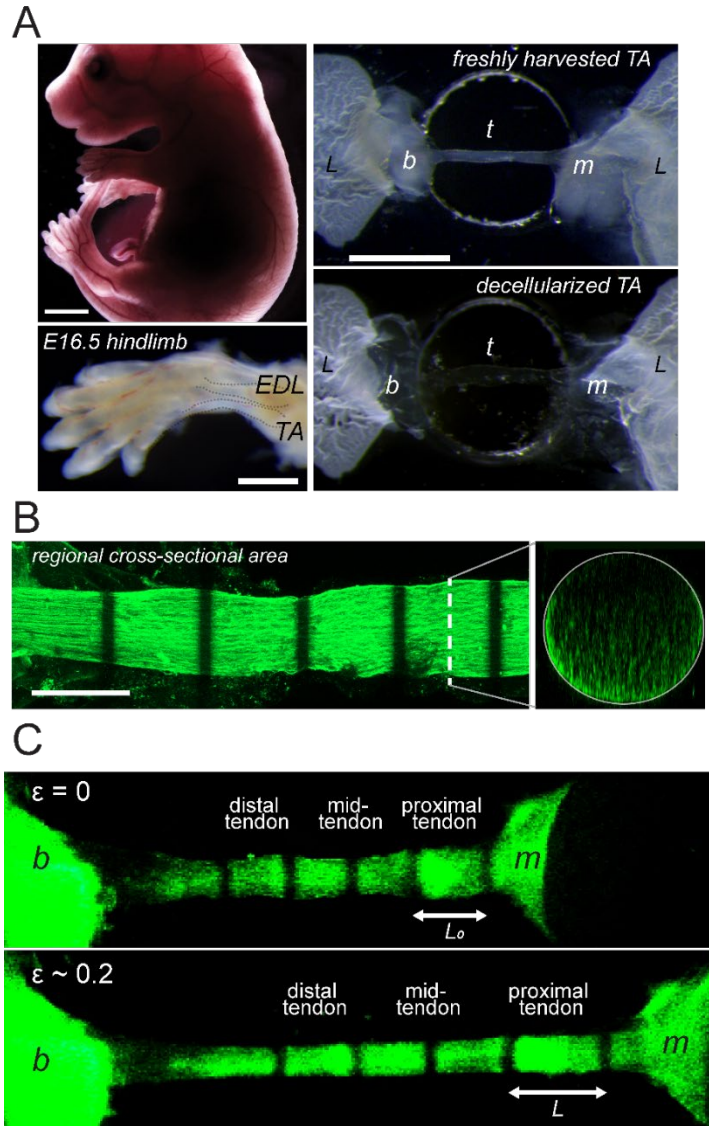


Figure 4.3. Experimental methods shown with an E16.5 embryo and tendon. **A.** Tendons were removed excised from hindlimb by first removing the skin and exposing the tibialis anterior (muscle-tendon-bone unit; TA) and the extensor digitorum longus (EDL). Then the TA was carefully dissected using fine tweezers and an 11-blade to separate the surrounding connective tissue. In order to minimize damage to the tendon (t) during decellularization, staining, handling, as well as to attach them to the 3D printed spring part during mechanical testing, TAs were glued onto PET frames using Loctite (L) from the muscle (m) and the bone (b) insertions (bars = 1mm). **B.** Z-projection of z-stack (Zeiss 800 WGA, 488, 10x) showing how the cross-sectional area of E16.5 tendon was obtained using orthogonal views (bar = 200  $\mu$ m). **C.** Macroscopic imaging of E16.5 decellularized TA during tensile testing showing the muscle (m) and bone (b) insertions and the regions investigated.

maintained to keep the physiologically relevant boundary conditions of the tendons and to aid in sample handling for mechanical testing. Tendons were adhered directly to laser-cut PET frames at the bone and muscle insertions using Loctite Super Glue Gel Control (**Fig. 4.3**), taking care to avoid the tendon and was immediately immersed in a large volume of PBS. Samples were either stained immediately as follows or decellularized as described below. Tendons were rinsed in  $1\times$  PBS and stained with AF488-conjugated wheat germ agglutinin (WGA; ThermoFisher) to visualize proteoglycans, diluted 1:50 in blocking buffer [10% donkey serum (Lampire) in  $1\times$  PBS with 0.1% Triton X-100 (PBST)] for 1h at room temperature.

Samples were imaged using an upright Zeiss LSM 800 confocal microscope (Carl Zeiss Microscopy) and a  $10\times$  Plan-Neofluar (NA = 0.3) objective. Equidistant lines between the muscle and bone insertions were photobleached onto the samples as fiduciary markers for the calculation of regional engineering strain. Briefly, a region of interest of 20  $\mu\text{m}$  in width was drawn along sample width using the Zen software's *Crop* feature. The 488 laser power was set to 100% and by acquiring a z-stack through the sample thickness in 10  $\mu\text{m}$  increments, a line was photobleached into the AF488 WGA stained tissue (**Fig. 4.3**). After all photobleached lines were generated, a z-stack of the entire tendon was acquired. The unloaded regional cross-sectional area was measured from the z-stack acquired using the ZenBlue software package (Carl Zeiss Microscopy). E16.5 tendons were tested using 4mm  $\times$  6mm frames and spring 1. E18.5 and P0 tendons were tested using 4mm  $\times$  7.65mm frames and spring 2. Tensile test to failure was conducted at  $0.01\text{s}^{-1}$  strain rate without preconditioning.

### ***Decellularization of tendons***

TA muscle-tendon-bone units were incubated in 8mL 0.05% sodium dodecyl sulfate (SDS) with  $1\times$  Halt protease inhibitor (PI, ThermoFisher) in  $1\times$  PBS and gently rocked overnight for decellularization. Decellularization of embryonic samples was completed overnight and SDS-PI solution was replaced every 24h for 7 days until decellularization of the postnatal samples was complete. Completion of decellularization was determined by subjective visual inspection of samples and when ECM visualization was enhanced after immunostaining<sup>115</sup>. Upon decellularization, samples were rinsed in an excess of  $1\times$  PBS for 1h and stained and imaged prior to mechanical testing as previously described. Tensile testing to failure was conducted at  $0.01\text{s}^{-1}$  strain rate without preconditioning.

### ***Fibrin gels***

Porous polyethylene blocks were adhered onto 6mm × 12.5mm frames using Loctite Super Glue Gel Control and used as anchor points for 2mg/mL fibrin gel. A custom mold was used to align the frame and to control the shape of fibrin gel as it polymerized so that a rectangular gel would form between the two porous polyethylene blocks. 14.15mg/mL human fibrinogen (FIB3, Enzyme Research Laboratories) and 1mg/mL Alexa Fluor 488 conjugated human fibrinogen (F-13191, Molecular Probes) were thawed in a 37°C water bath, mixed at a 1:10 fibrinogen content ratio, and diluted in PBS to achieve a 2mg/mL fibrinogen solution. 1μL 2M CaCl<sub>2</sub> was added to the fibrinogen solution. 3.54mg/mL, 3046 NIH units/mg of human alpha thrombin (HT 1002a, Enzyme Research Laboratories) was thawed, diluted to 1 Thrombin units (UT)/μL, and introduced to the 2mg/mL fibrinogen solution at a concentration of 0.0004 UT/mg fibrinogen to initiate the fibrin gel polymerization. Fibrin gel frames were loaded onto Spring 3 for uniaxial loading. Tensile test was conducted at 0.01s<sup>-1</sup> strain rate loading and unloading to a 1000μm displacement.

### ***Fibronectin***

Polydimethylsiloxane (Sylgard 184, Dow Corning) was cured at 10:1, manually cut into blocks, adhered onto 6mm × 12.5 mm frames using Loctite Super Glue Gel Control, and coated with fibronectin (FN) matrix as previously described<sup>140,141</sup>. FN-coated frames were stained with Alexa Fluor 488-conjugated WGA (ThermoFisher), diluted 1:100 in 1× PBS + 0.2% bovine serum albumin + 0.02% sodium azide for 24 hours at 4°C, then rinsed with 1× PBST at room temperature for 30 minutes. Fiducial lines were photobleached using the 488 laser line on a confocal microscope (Zeiss LSM 800), as previously described. FN-coated frames were loaded onto Spring 3 for uniaxial loading. Cyclic loading and unloading was performed at a 0.04s<sup>-1</sup> strain rate up to 400μm for 10 cycles. Tensile test to failure was conducted at 0.04s<sup>-1</sup> strain rate until 5,000μm displacement or material failure.

### ***Solaris (reference material)***

System validation was performed by testing Solaris (Smooth-On, Inc.), a platinum-cured silicone, and comparing data from our set up with that acquired using a commercially available bulk tensile tester (TA.XTPlus Connect, Texture Technologies). Solaris was selected because the

material properties can be modulated to have similar stiffness as the biological samples of interest. Solaris was prepared per manufacturer's instructions and cut to size manually with a blade. A mixture of equal parts Solaris Part A and Part B was prepared in a 20mL scintillation vial followed by degassing with a vacuum desiccator. Thin film samples for mechanical testing on the FemtoTools system were prepared by spin coating (Laurell Technologies Corporation WS-650-23B) 2g of uncured Solaris on a 75mm × 25mm microscope slide coated with polyacrylic acid. Samples were spin coated at 3000 RPM for 30 seconds then placed in an oven at 70°C to cure for 3 hours. The films were  $117 \pm 4.2\mu\text{m}$  (average  $\pm$  S.D.) thick and were easily floated off the microscope slide onto reverse osmosis purified water due to dissolution of the intermediate polyacrylic acid layer. To generate samples with the optimal aspect ratio for tensile testing, the thin films were cut using a laser-etched grid and a scalpel. Samples tested with spring 1 were  $2645 \pm 471.4\mu\text{m} \times 216.4 \pm 42.3\mu\text{m}$  and samples tested with spring 2 were  $3514 \pm 420.6\mu\text{m} \times 308.1 \pm 82.5\mu\text{m}$  (L × W). Samples for bulk testing were prepared by filling a 75mm × 50mm × 4mm glass mold with uncured Solaris and leaving it to cure in an oven at 70°C for 5 hours. The dimensions of samples tested on the bulk tensile tester were  $15.29 \pm 0.48\text{mm} \times 6.32 \pm 1.5\text{mm} \times 3.85 \pm 0.04\text{mm}$  (L × W × H).

Solaris thin films were adhered directly to PET frames using Loctite Super Glue Gel Control. Tensile tests were performed using the FemtoTools micromanipulator and spring system described above. The cross-sectional area and length of Solaris samples was measured optically, and actuator displacement data was used to calculate strain. The tangent modulus of Solaris was calculated from the stress-strain response of samples tested using two different configurations of the spring (springs 1 and 2) as well as the TA.XTPlus Connect. For bulk testing, Solaris samples were gripped at each end using the TA.XTPlus clamps, and tensile tests were performed while force and displacement data were recorded through the TA.XTPlus Connect system.

## 4.4 Results

### 4.4.1 Spring design

Springs 1, 2, and 3, and their respective frames, were designed to accommodate various sample geometries, as described in the methods. The spring coil design for Springs 1-3 was the same, however, the area between the frame attachment sites were modified to accommodate the geometry of the different frames and biological samples. The force contribution from the three different spring designs, or baseline, was similar (**Fig. 4.4**). The baseline from the spring during uniaxial tensile testing was lower than the force contribution from the samples of interest. Therefore, the force contribution from the spring was subtracted to isolate the force contribution from the sample of interest (**Fig. 4.5**). Additionally, we observed that the force contribution of spring 1 remained constant, with minimal fatigue, after use. A SolidWorks assembly was constructed to perform finite element model simulations to inform how design changes would influence the mechanical properties of the springs. Initially, the elastic modulus value for the M2R-CL polymer provided by the manufacturer, 1500-2000 MPa, was used for the simulations. However, there were significant differences between the force-displacement results from the simulation and empirical data from the springs (**Appendix A**). Empirical force-displacement data from spring 1 was used to calculate the stiffness of the M2R-CL 3D-printed spring, approximately 20 MPa. Since the material properties of the M2R-CL polymer may vary depending on the 3D-printing orientation and post-processing methods, the stiffness calculated from empirical data was used over the value provided by the manufacturer. Using 20

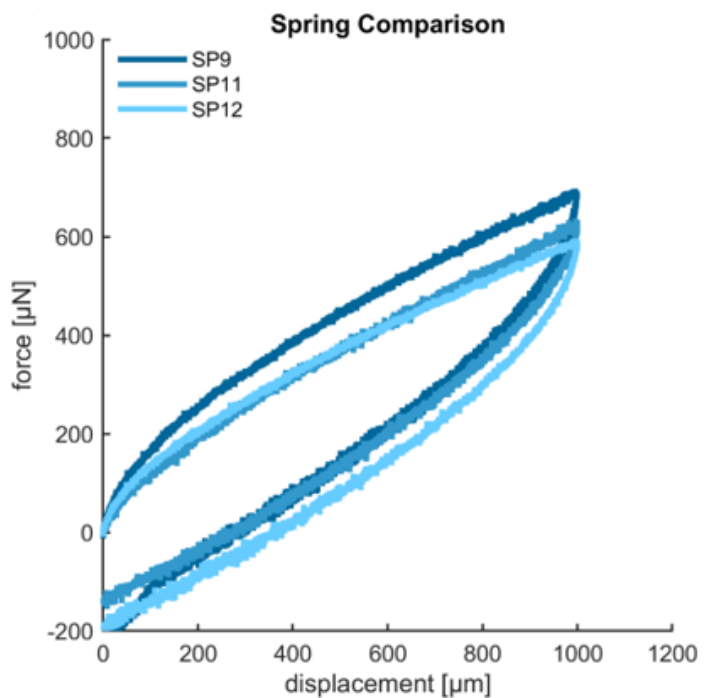


Figure 4.4. Mechanical contribution of three different 3D printed springs (SP9 is later referred as spring 1; SP10 is later referred to as spring 2).

MPa for the elastic modulus of the M2R-CL polymer resulted in finite element model simulation results that more closely aligned with empirical results (**Appendix A**). Simulations were run with and without a roller-slider fixture that would prevent the spring from moving out of the  $XY$  plane (**Appendix A**). Simulations run without the roller-slider fixture show that there is a rigid body rotation of the spring and pillar during tensile testing. The rigid body rotation results in differences between the displacement prescribed by the micromanipulator and the moving end of the sample during tensile testing and causes the sample to move out of the imaging plane (**Appendix A**).

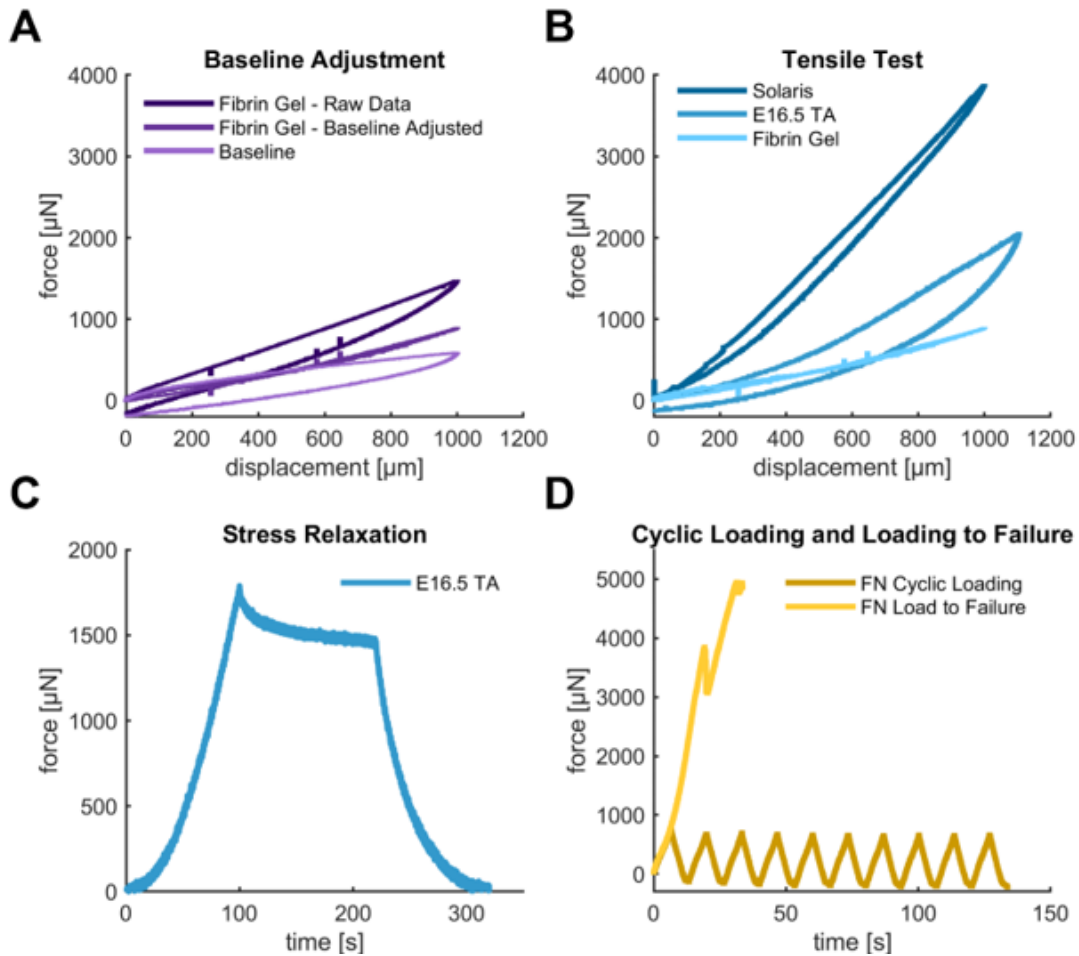


Figure 4.5. Baseline adjustment (**A**) and testing modalities (**B-D**). **A**. Fibrin gel raw data, baseline, and baseline-adjusted fibrin gel. **B**. Force-displacement curves of Solaris, E16.5 TA, and fibrin gel. **C**. Stress relaxation test for E16.5 TA. **D**. Cyclic loading and tensile loading to failure for FN matrix.

#### 4.4.2 Spring-micromanipulator system comparison to bulk tensile tester

Comparison of the system to a commercially available instrument was completed with the testing of Solaris samples using both systems. Furthermore, two different spring configurations were used to investigate their influence on the material properties obtained. Stress – strain curves for Solaris testing with all 3 different setups were plotted and the tangent moduli at physiologically relevant strain values were compared (**Fig. 4.6**). Representative curves show the similarities among the curves, with the bulk material curve having a slightly higher slope at lower strain values (local). When considering the global linear slope, both FemtoTools curves greatly overlap, while the bulk material curve diverges from them at lower strain values and remains parallel to the other curves at strain values greater than 0.15 (**Fig. 4.6A**). This divergence is also exemplified by the tangent moduli at strain=0.1 where the tangent moduli of Solaris samples tested with FemtoTools are significantly different than those samples testing with the TA.XTPlus system (**Fig. 4.6B**). Testing Solaris with two different spring configurations (*i.e.* spring 1, spring 2) with the FemtoTools system does not lead to significantly different tangent moduli for this material. At strain values of 0.15, 0.2 and 0.25, there are no significant differences in the tangent moduli obtained for Solaris with all 3 different testing configurations.

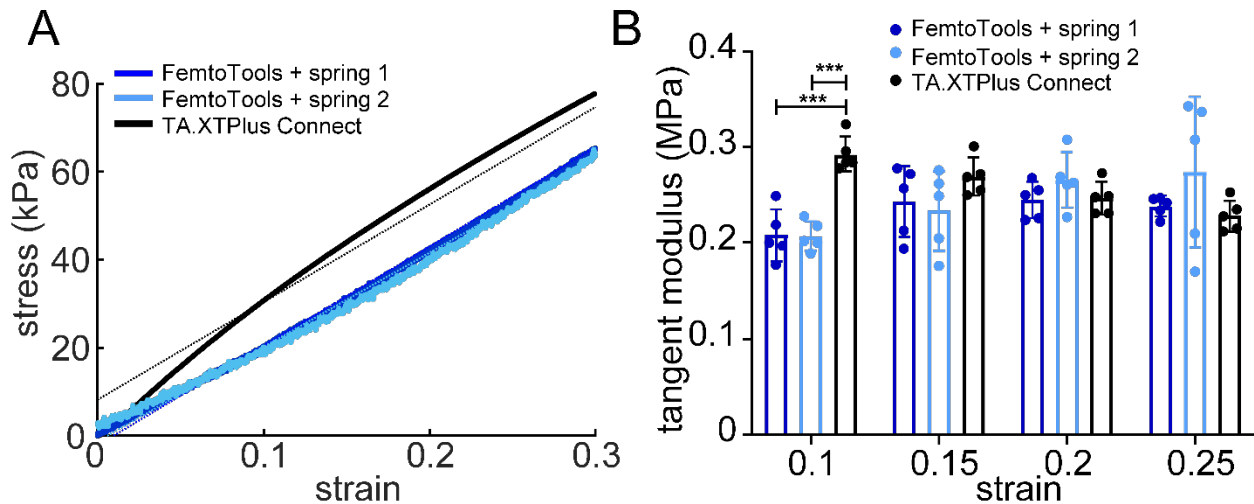


Figure 4.6. Comparison of FemtoTools system to bulk material testing. **A.** Representative stress - strain curves of Solaris samples tested. **B.** Comparison of the tangent moduli of Solaris tested two spring configurations in the FemtoTools system (blue, magenta) and with bulk material testing instrument (black) (FemtoTools + spring 1 (n=5), FemtoTools + spring 2 (n=5), bulk material (n=5); error bars = std. dev.; \*\*\* $p < 0.0002$ , \*\*\*\* $p < 0.0001$ ).

### 4.4.3 Uniaxial loading of various materials

Preliminary tests demonstrated the capability of the system to perform standard mechanical tests on a variety of soft biomaterials and small tissues. The force-displacement response of different samples can be clearly resolved after subtracting the contribution of the spring (**Fig. 4.5**). Our system was able to resolve a variety of mechanical responses. For example, Solaris and E16.5 TA tendon displayed viscoelastic properties, as observed by the hysteresis in tensile test and stress relaxation curves (**Fig. 4.5**). In contrast, the fibrin gel was elastic (**Fig. 4.5**). The representative FN matrix sample displayed the ability of the system to perform cyclic loading and loading to failure (**Fig. 4.5**). Stress – strain curves showed dramatic differences between actuator (based on the imposed displacement) and optical strain (based on the calculated distance between fiducial markers) for E16.5 and E18.5 tendons and FN (**Fig. 4.7**).

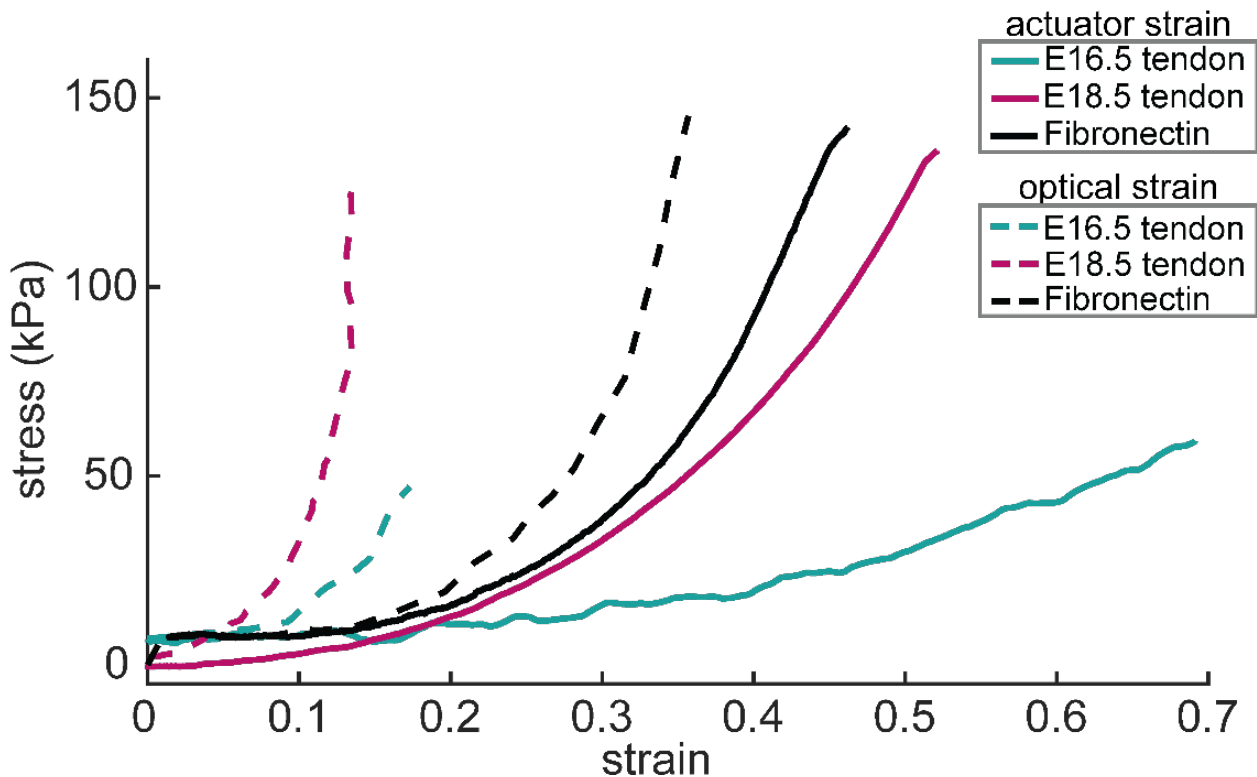


Figure 4.7. Comparison of actuator strain (solid lines) and optical strain (dashed lines) for representative E16.5 and E18.5 tendons and fibronectin. Actuator strain is based on the imposed displacement and the initial sample length. Optical strain is calculated from the change in distance between photobleached lines.

The evaluation of embryonic and postnatal decellularized tendons showed an increase in stiffness as a function of development. Regional stress - strain data points were averaged to obtain one representative curve for each sample and compare the mechanical behavior at these two embryonic timepoints (**Fig. 4.8**). Stress - strain datapoints were fitted to polynomial functions for the calculation of the tangent moduli at relevant strain values. The  $R^2$  values determined the appropriate polynomial fit for each curve. Embryonic tendon data sets were fitted to a second degree polynomial (**Fig. 4.8**). The tangent moduli for each sample (**Table 4.1**) were plotted along with the average and standard deviation for each developmental timepoint (**Fig. 4.8**). A two-way ANOVA showed significant differences between E16.5 and E18.5 at strain values greater than 0.1.

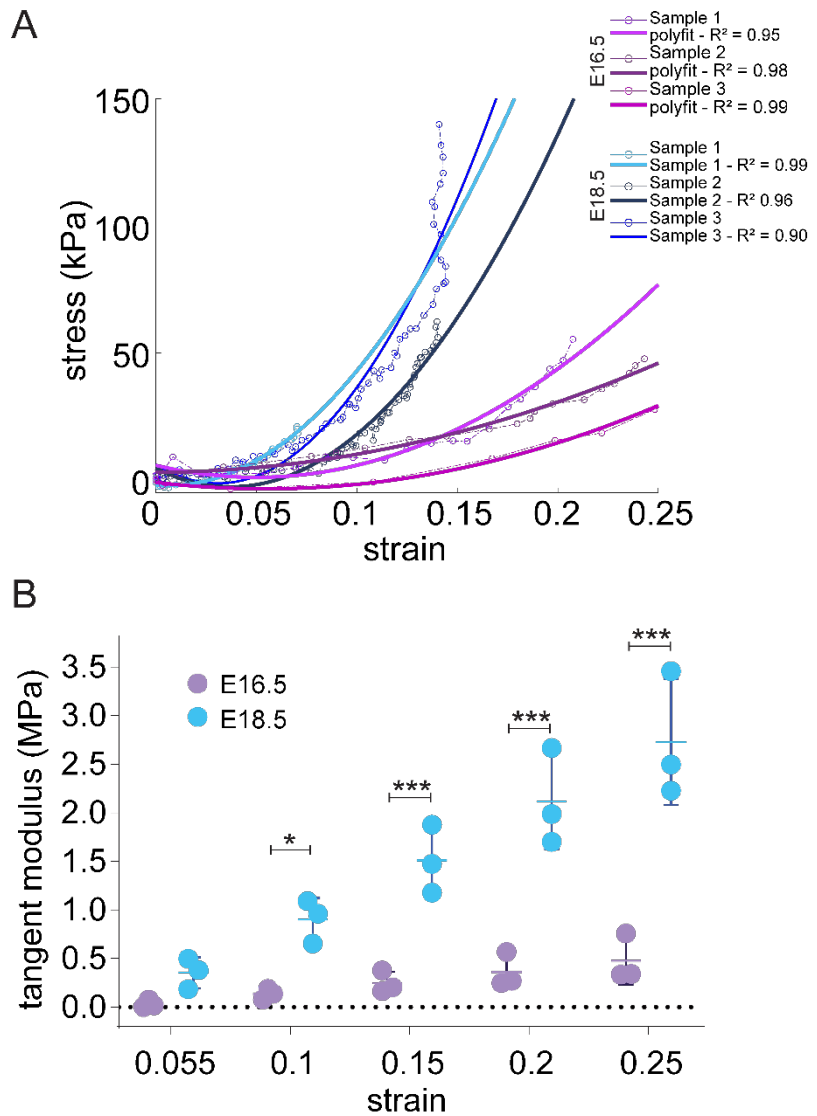


Figure 4.8. Mechanical behavior of decellularized embryonic tendons. **A.** Calculated stress - strain curves for E16.5 (purple) and E18.5 (blue) samples, along with their fitted polynomial. **B.** Sidak multiple comparisons showed significant differences in the tangent modulus between E16.5 and E18.5 tendons (\* $0.0021 < p \leq 0.0332$ ; \*\* $0.0002 < p \leq 0.0021$ , \*\*\* $0.0002 < p \leq 0.0001$ , \*\*\*\* $p < 0.0001$ ;  $n = 3$ ; bars = S.D.).

Further, regional variability in strain was observed for E16.5 decellularized tendons, indicated by the greater distance between photobleached lines in the proximal tendon resulting from tension. The stress - strain response indicated the stiffness of the tendon at the distal region was greater than the mid and proximal ends (**Fig. 4.9**). Two-way ANOVA indicated both strain

value and region along the tendon had a significant effect on the tangent moduli of E16.5 decellularized TA, indicating nonlinear behavior (**Fig. 4.9**). Similarly, regional strain variability was observed for P0 and E18.5 TA tendons. Stress - strain curves showed the mechanical variations along the tendon and an increase in tangent moduli as a function of development. The tangent moduli of the distal regions were greater than proximal regions for both the E18.5 and P0 tendons (**Fig. 4.10**).

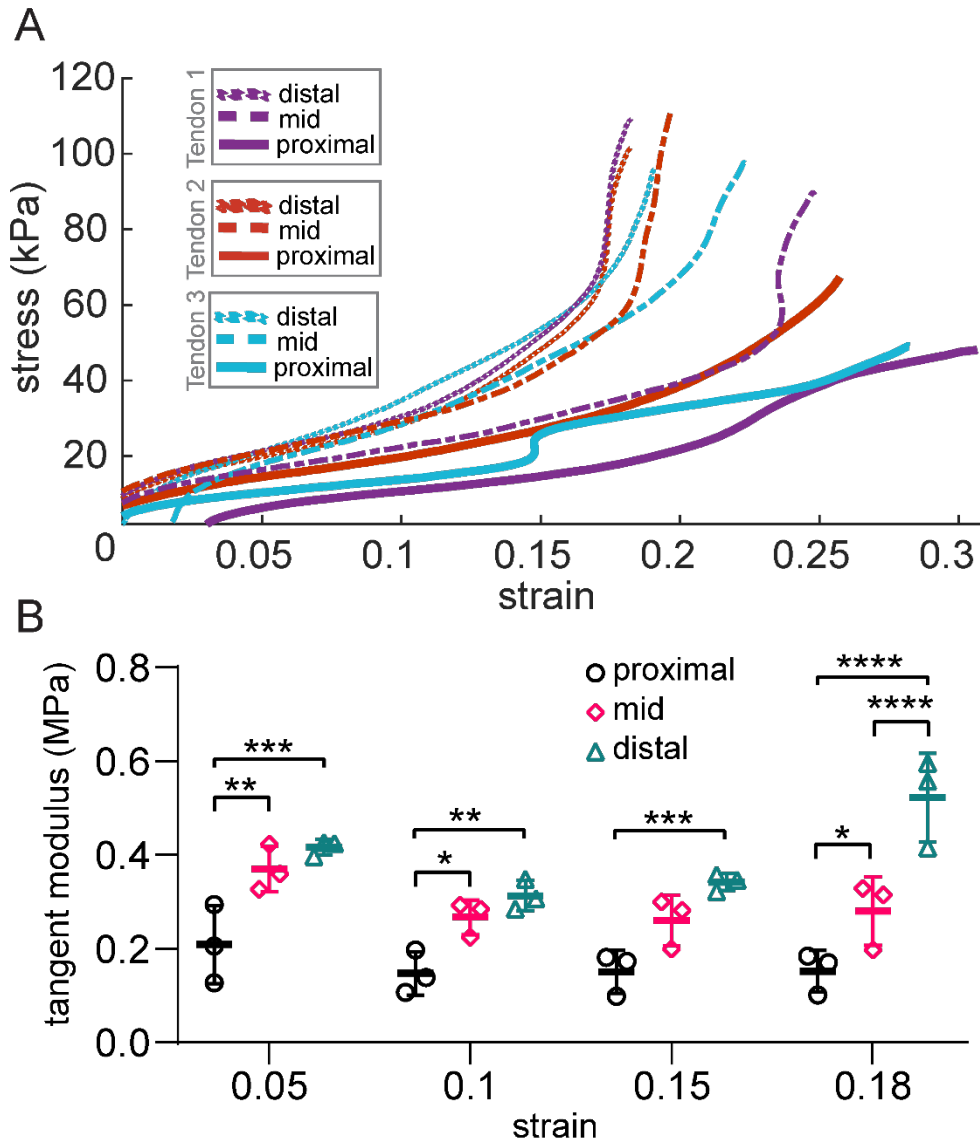


Figure 4.9. **A.** Regional stress - strain curves of decellularized E16.5 TA. **B.** Tukey multiple comparisons showed significant differences in the tangent modulus between individual groups (\* $0.0021 < p \leq 0.032$ ; \*\* $0.0002 < p \leq 0.0021$ , \*\*\* $0.0002 < p \leq 0.0001$ , \*\*\*\* $p < 0.0001$ ;  $n = 3$ ; bars = S.D.).

## 4.5 Statistical methods

All the statistical analyses were conducted using GraphPad Prism 8.4.2 (GraphPad Software). A two-way ANOVA and Tukey's post hoc test were performed to evaluate differences in the mean tangent moduli among Solaris samples tested with different instruments (*i.e.* custom FemtoTools system and TA.XTPlus Connect). For the evaluation of tendon mechanics as a function of development, a two way ANOVA with Sidak multiple comparisons was conducted on the mean tangent moduli at each stage. For the evaluation of regional stiffness in E16.5 tendons, a two-way ANOVA and Tukey multiple comparisons test was performed.

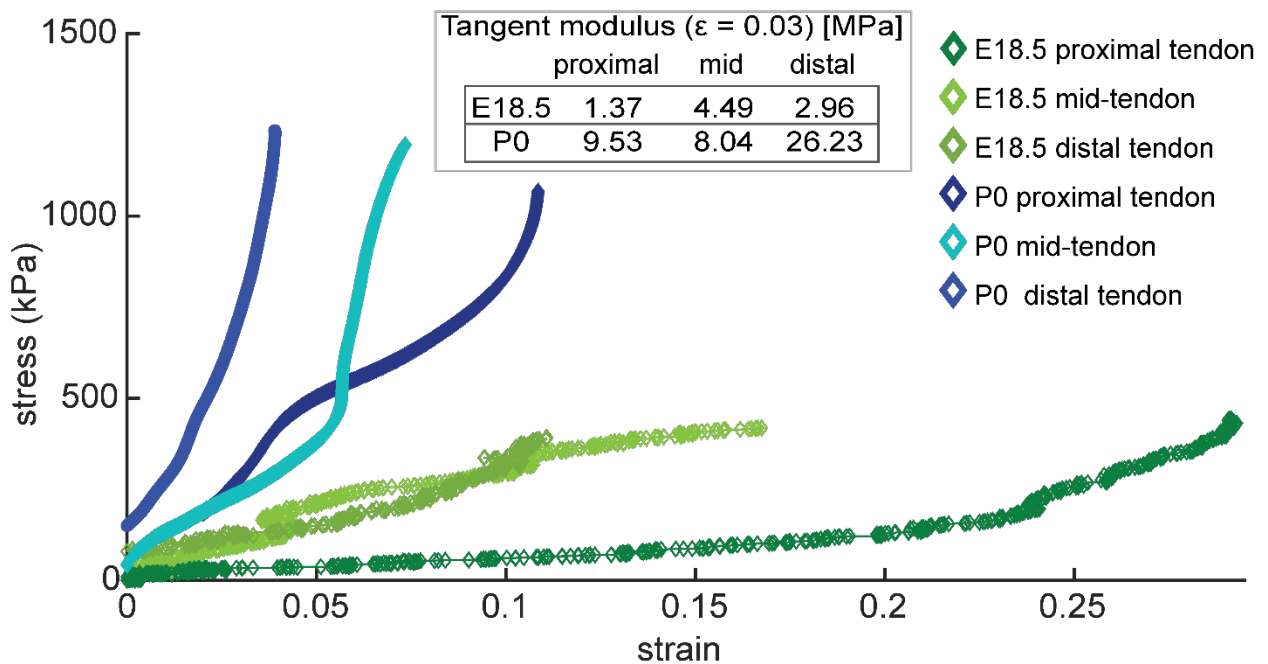


Figure 4.10. Stress - strain curves show regional mechanical variations and an increase in tangent moduli as a function of development when comparing E18.5 (green) and P0 (blue).

## 4.6 Discussion

In this study, we designed a novel device that is capable of assessing the mechanical behavior of soft tissues and biomaterials and showcased the ability of the system to interrogate biological questions. We customized a commercially available micromanipulator with a force resolution of 5 nN and a displacement sensing range starting at 5 nm, facilitating the application of displacements on small samples while recoding force. Briefly, using a custom spring system

biological samples are coupled to the microforce sensors of the micromanipulator preventing sample dehydration during testing while also protecting the electronics from water damage. Further, the modularity and low footprint of the system allowed testing under a dissecting microscope for the calculating of optical strain throughout the test. Our data demonstrate the capability of the FemtoTools micromanipulator and spring system to resolve the force contribution of a sample of interest by subtracting the force contribution of the spring. Using this strategy, the system correctly characterized a reference material Solaris of known material properties similar to those of the tissues and biomaterials we are interested in characterizing. This provides assurance that the system can be used to measure the mechanical properties of materials of unknown properties. The study evaluated the mechanical response of FN matrix, fibrin gels, and embryonic and postnatal tendons. Characterization of the mechanical properties of small embryonic tissues is crucial for understanding the role of mechanics in tissue formation. We showed that the spring design can be modified to accommodate various biologically relevant sample geometries and stiffnesses.

Our modular system can be used to mechanically characterize soft biomaterials and small tissues to help provide physiologically-relevant design parameters for scaffolding that seek to emulate native tissue mechanics. The modularity of the system allowed us to test tissues of different stiffnesses and sizes. Further, force and displacement curves show minimal noise and drag in unfiltered data (**Fig. 4.5**), minimizing the need for processing through filtering and noise-reducing algorithms. The appropriate 3D printed spring, micromanipulator arm length, microforce sensor are selected according to the tissue size and stiffness estimated before the collection of empirical data. When selecting and developing a testing system, the force resolution and maximum force capacity, as well as the gauge dimensions, will determine the tissues that can be tested with the system. In order to test developing tissues that are changing in dimensions as a function of development the adaptability of the system and the force resolution are critical. Adapting to larger or smaller samples has proven feasible given the ease of fabrication through 3D printing of springs and laser cutting of PET frames. The modularity of the system also enable multiscale studies given that the micromanipulator system can be couple with the microscope of choice to investigate the desired scale. For instance, by coupling to a dissecting scope we assess the tissue scale, but the system has the potential to be compatible with a variety of imaging and microscopy platforms through the adaptation of custom fixtures.

The results obtained for the elastomer Solaris are similar to those reported by others and by the manufacturer<sup>142,143</sup>. However, differences in the synthesizing and curing protocols for the samples fabricated both for FemtoTools and bulk material testing could explain the discrepancies in the calculated tangent moduli at 0.1 strain, where the bulk material testing system led to a greater modulus (**Fig. 4.6**). Solaris samples were fabricated with a relevant cross-sectional area for each testing modality, in order to test the same material with two different systems and force sensors. For a uniform thickness, samples tested with the micromanipulator system were fabricated via spin coating, potentially causing shear stress to align Solaris chains thus influencing the stress – strain response. Future experiments need to test samples that are synthesized and cured under the same conditions using both instruments. Independent of fabrication differences, our instrument identified similar tangent moduli for Solaris tested with a bulk material tester. The material behavior recorded for FN matrix and fibrin gel are similar to those previously published<sup>140,141</sup>. Fibrin gels have a nonlinear elastic behavior while FN matrices are viscoelastic<sup>51,63</sup>.

Tendons are responsible for transferring the force produced by the muscle to the skeleton with high fidelity while avoiding musculoskeletal injury. Uniaxial tensile testing is most commonly used to characterize the bulk mechanical properties of adult tendon. Connective tissues, such as tendon, are mostly made of extracellular matrix proteins, with only few cells embedded at their adult stage. On the other hand, embryonic tendons are highly cellular and are comprised of a sparse microenvironment. Embryonic tendons are challenging to test using the instrumentation designed to handle larger, stiffer tissues. Instruments developed to evaluate adult tendon mechanics are oftentimes not appropriate for these much smaller and softer tissues. Tangent moduli calculated for embryonic and postnatal tendons show an increase in stiffness as a function of development, as others have reported when investigating rat and mouse tendons<sup>132,144</sup>. Stress – strain curves showed a positive relation between tangent moduli and strain. As expected, tendons show viscoelastic behavior, as seen with stress relaxation and hysteresis. These data demonstrate our experimental and computational methods can be reliably used to investigate the regional mechanics of the ECM in small developing tissues. Given the challenges in mechanically testing embryonic murine tendons, tendon development is often studied using chick models and measuring the indentation modulus at the nano and microscales<sup>145,146</sup>. The novelty and capabilities of our system allow the characterization of embryonic tendon mechanics in mice as a function of development based on uniaxial loading and optical strain.

The different stress – strain curves among samples within a developmental timepoint could be due to biological variability, as well as related to the video quality during testing. Further, the process of attaching tendons to PET frames could also affect the measured mechanical behavior if glue was to cure onto the tendon surface. Moreover, the presence of glue hinders the visualization of proteoglycans on the surface, and consequently affects the tracking of photobleached lines. This grip mechanism might need to be further evaluated, since most of the samples tested failed at the muscle insertion and slipping was often observed by dips in the force measurements recorded during testing<sup>130</sup>. Often, criteria for clamping success includes failure at the mid-substance as opposed to at the attachment points<sup>132</sup>. The interface between the muscle and the glue might be tearing during testing, leading to a gradual decrease in force prior to detachment. The interface between the muscle and the glue might be tearing during testing, leading to a gradual decrease in force prior to detachment. On another note, the decellularization conducted could also add to the observed variability between samples. Decellularization was conducted to enhance the quality of the video recorded for the calculation of optical strain, enhancing the contrast between photobleached lines and the rest of the sample. E16.5 and E18.5 tendons were processed with the same concentration of detergent overnight. However, to better understand the effect of this treatment in the composition and mechanics of embryonic tendons, a proteomic analysis will be needed in the future, as well as mechanically testing freshly harvested tendons. From the data presented here (**Fig. 4.8, Table 4.1**) and preliminary force - displacement curves for freshly harvested and decellularized tendons, we expect to obtain similar trends across timepoints, with an increase in stiffness as a function of development.

Table 4.1. Tangent moduli of E16.5 and E18.5 tendons

<b>Strain</b>	<b>tangent modulus [MPa]</b>					
	<i>E16.5</i>			<i>E18.5</i>		
0.055	0.078	0.019	0.001	0.38	0.185	0.5
0.1	0.138	0.189	0.078	1.09	0.656	0.961
0.15	0.205	0.379	0.164	1.879	1.18	1.474
0.2	0.273	0.568	0.249	2.669	1.703	1.987
0.25	0.34	0.758	0.335	3.458	2.227	2.499

Further design optimization and validation testing is needed to fully evaluate and address the limitations of the system. Although the mechanical contribution of the spring has been shown

to not change over time, it is still important to adjust for the spring contribution based on data collected the same day as mechanical testing to account for potential variations. The material properties of the 3D printed material might be affected by post-processing of each 3D printed part, as well as spring dimensions. Empirical data showed the mechanical properties of the 3D printed spring are orders of magnitude away from those properties reported of the manufacturer. This discrepancy needs further investigation to determine the effect of post-processing and printing orientation. Additionally, the compliance of the 3D spring and the PET frame limit the stiffness of samples that we be tested with our system. When tendons at a later postnatal stage were tested (P3), the 3D printed pillar rotated and deflected, along with undergoing rigid body motion. Deflection keeps the tendons from being loaded uniaxially and could lead to force readings that do not correspond to the stiffness of the tendon. Pillar rotation also leads to additional error in optical strain since the fiducial markers go out of imaging plane during testing.

Taken together, these data show the ability of our system to characterize a variety of biomaterials and small soft tissues with different material properties. Uniaxially loading tissues while taking force measurement is instrumental in that characterization needed to probe material properties. The small size and susceptibility to damage of soft embryonic tissues and biomaterials limit the use of tensile testing modalities otherwise used for adult soft tissues. Our modular system can be used to mechanically characterize soft biomaterials and small tissues and provide physiologically-relevant design parameters that guide the design of scaffolding that seek to recapitulate native tissue mechanics and facilitate cell-ECM interactions.

## 5. CHARACTERIZATION OF EXTRACELLULAR MATRIX NETWORKS UNDER TENSION

### 5.1 Abstract

Cellular behavior is affected by the stiffness of the microenvironment and influenced by the composition and organization of the extracellular matrix (ECM). Mechanosensing of ECM stiffness occurs by cells at the fibrillar, mesoscale between the single molecule and the bulk tissue scales. The *in situ* characterization of fibrillar mechanics is hindered by the presence of cells and a dense ECM in adult tissues. We previously demonstrated, using a combination of decellularization and confocal microscopy, that ECM networks in less dense embryonic tissues, can be easily visualized<sup>115</sup>. The objective of this work was to investigate ECM network strain after uniaxial loading to characterize the individual components of the cellular microenvironment in the native conformation. Preliminary data was collected by mounting decellularized and immunostained tendons on a custom-made translating stage. Tendons were imaged at 10× using a confocal microscope and 5 lines were photobleached onto the samples as markers for the calculation of engineering strain. The coordinates for the center of each photobleached line were obtained and used to calculate the *in situ* engineering strain between two lines, using the average horizontal distance between lines across individual z-stacks. Prescribed and residual strain were calculated. Fibronectin appeared to be more extensible by having lower residual strain after loading. Next, we implemented a micro-robotic system to conduct uniaxial loading by recording force and displacement while imaging ECM protein networks. These data demonstrate our experimental and computational methods can investigate ECM networks mechanics *in situ*. Quantifying the material properties of the ECM will provide design parameters for physiologically relevant scaffolds that can direct cell behavior *in vitro* (fundamental for mechanobiology) and *in vivo* (essential for regenerative medicine).

## 5.2 Introduction

Cellular behavior is affected by the stiffness, composition, and 3D organization of the surrounding extracellular matrix (ECM). Mechanosensing of ECM stiffness occurs by cells at the fibrillar level, or the mesoscale between the single molecule and the bulk tissue scales. The *in situ* characterization of fibrillar mechanics is hindered by the presence of cells and a dense ECM in adult tissues<sup>68</sup>. Mechanical testing of the ECM at the mesoscale is challenging due to the difficulty in extracting these relatively insoluble networks from dense connective tissues. To bypass these challenges, methods to isolate intact type I collagen and fibrillin fibrils from biological tissues have been developed<sup>113,114,135</sup>. To isolate and constrain these fibrils, samples are oftentimes dried and rehydrated<sup>135,147</sup>. These processing steps along with testing conditions (*e.g.* fully hydrated, air dried) of the fibrils can affect their mechanical response<sup>147</sup>, and lead to significantly different material properties. Additionally, the boundary conditions are disrupted, meaning these fibrils are not tested in the native network configuration. The stiffness of ECM networks can also be regulated by post-translational modifications, such as the hydroxylation of proline and lysine. For example, type I collagen fibril assembly and stability is dependent on the formation of hydroxyproline (stabilize the triple helix) and hydroxylysine (form cross-links)<sup>148,149</sup>. Variations in reconstituting *in vitro* and testing protocols has led to a wide range of reported material properties<sup>54,150,151</sup>. Alternatively, researchers tested the mesoscale mechanics of single ECM proteins assembled *in vitro*. Yet, without cells or accessory molecules to orchestrate ECM network assembly it is unlikely that these networks have the necessary cues for the correct formation of ECM architecture.

Given that *in vitro* approaches usually cannot thoroughly recapitulate networks synthesized *in vivo*, we capitalize on the sparsity of the ECM in embryonic tissues to study mesoscale mechanics. During development, the ECM architecture is less dense than in adult tissues, making it feasible to visualize discrete components and providing an ideal system to determine the material properties of native networks. We previously demonstrated, using a combination of decellularization and confocal microscopy, that ECM networks in less dense embryonic tissues, can be easily visualized<sup>115</sup>. Using this technique, we then visualized ECM deformation before and after compression of E14.5 forelimbs, enabling the quantification of significant differences in maximum principal strain<sup>152</sup>. However, compression is not the ideal testing modality for characterizing network mechanics. Cells exert tensile forces on their

microenvironment, interacting locally with both parallel and perpendicular fibrils (**Fig. 1.1**)<sup>7</sup>. Therefore, it is important to look at tissues that are physiologically loaded in tension when seeking to investigate ECM mesoscale mechanics. For tensile testing, it is important to consider the specimen size and aspect ratio. Others have reported error in the transverse direction when samples do not have an appropriate aspect ratio; in other words, when the ratio of the short and long axis is not large enough<sup>153,154</sup>. We therefore selected tendon, specifically the tibialis anterior, as the tissue to investigate ECM network strain *in situ*. The tibialis anterior tendon (TA) not only has the ideal aspect ratio, but it can also be easily dissected along with the muscle and bone insertions, keeping boundary conditions unperturbed during mechanical testing.

The objective of this work is to investigate ECM network strain after uniaxial loading to characterize discrete components of the cellular microenvironment *in situ* at the mesoscale, using developing tendons. First, we developed experimental and computational methodologies to apply tension to tissues while concurrently visualizing ECM networks to investigate ECM deformation. Our findings indicate that fibronectin networks are more extensible than type I collagen, fibrillin-2, and proteoglycans networks successfully recover after uniaxial loading. These data indicate that mesoscale ECM network deformation can be investigated when loading the tissue at the macroscale. Next, with our novel FemtoTools micro-robotic system we have a unique opportunity to test the mechanics of soft tissues and, by adapting it to a confocal microscope, characterize networks in their native conformation with a physiologically relevant testing modality. Lastly, we investigated the ultrastructure of embryonic and postnatal tendons, given that the length and diameter of type I collagen fibrils have been reported to change with age and are known to influence tissue mechanics<sup>155</sup>.

The geometry of some networks may change during growth and remodeling. However, given that the same components are present in embryonic and adult tissues, we expect to be able to extrapolate these results and relate them back to the ECM of adult, healthy tissues, since the material properties of these networks, regardless of the dimensions, are likely consistent. Collectively, these tools and studies set the foundation for the mesoscale characterization of the native ECM. Defining the material properties of specific ECM networks can have a profound impact by providing design parameters for physiologically relevant scaffolds that can direct cell behavior *in vitro* and *in vivo*.

## 5.3 Materials and Methods

### 5.3.1 Tendon decellularization for enhanced ECM visualization

All murine experiments were approved by the Purdue Animal Care and Use Committee (PACUC; protocol 1209000723). C57BL/6 mice were time-mated to generate embryonic day (E)16.5, and E18.5, as well as postnatal day (P)0 pups. The murine gestational period is 19 to 21 days, with P0 being the day pups are born. For the dissection of embryonic tendons, dams were euthanized via CO<sub>2</sub> inhalation, which was then confirmed using cervical dislocation. Embryos were removed from the uterine horns, rinsed in chilled 1× phosphate-buffered saline (PBS) and the hindlimbs were excised at the hip joint. Pups were euthanized by decapitation and the hindlimbs removed and placed in ice cold PBS. Under a dissecting microscope (DFC450, Leica Microsystems), tibialis anterior (TA) muscle-tendon-bone units were dissected by first removing the skin with fine-tipped tweezers. After removing the skin, it is possible to visually locate the TA from the innermost digit of the foot to the tibialis anterior muscle (**Fig. 5.1**). Then, the surrounding connective tissue was separated from the tendon and the bone and muscle insertions with an 11-blade. The outermost digits and the proximal end of the muscle were cut with spring scissors to excise the muscle-tendon-bone unit. The bone and muscle insertions were maintained to keep the physiologically relevant boundary conditions of the tendons and to aid in sample handling, minimizing tissue damage. Tendons were adhered directly to laser-cut polyethylene terephthalate (PET) frames at the bone and muscle insertions using Loctite Super Glue Gel Control (**Fig. 5.1**), taking care to avoid the tendon and was immediately immersed in a large volume of chilled PBS. It was important to do so quickly in order to keep the glue from wicking onto the tendon. This is particularly critical when dissecting tendons at embryonic timepoints (*e.g.* E16.5) given their small size (~1 mm in length; **Fig. 4.3**). Gluing the tendon shortly after dissection minimized sample damage from handling and changing solutions along the decellularization and immunostaining processes.

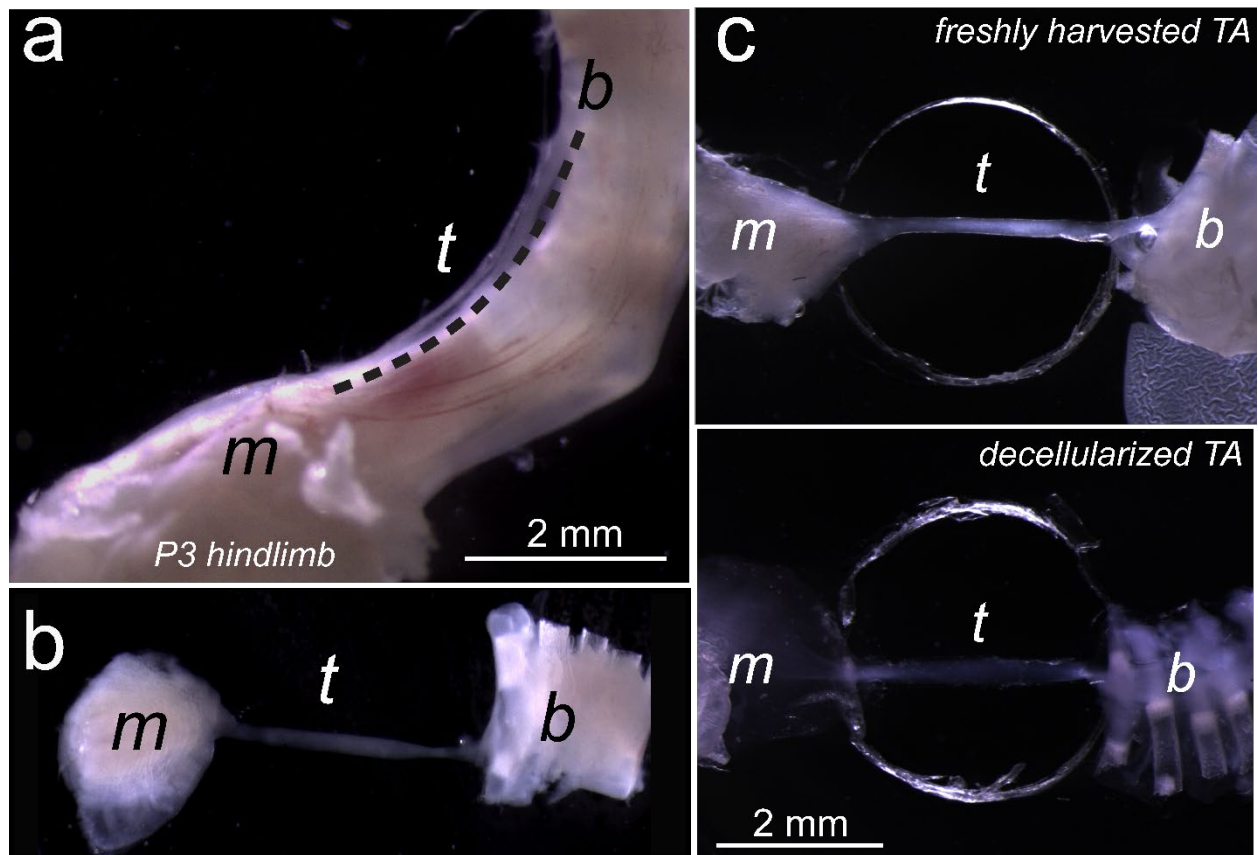


Figure 5.1. Harvesting P3 tendons. **a.** Location of tibialis anterior (TA) in the P3 hindlimb showing the muscle (m) – tendon (t) – bone (b) units before and **b.** after dissection. **c.** Freshly harvested units fixed to clear vinyl frames and after decellularization using 0.05% SDS in PBS.

In order to enhance ECM visualization, tendons were decellularized as follows. Embryonic TAs were incubated in 8mL 0.05% sodium dodecyl sulfate (SDS) with 1× Halt protease inhibitor (PI, ThermoFisher) in 1× PBS and gently rocked overnight for decellularization. The optimal decellularization protocol of postnatal was determined based on the enhancement of ECM visualization in a confocal microscope after immunostaining. The number of days, the SDS concentration (0.05% and 0.1%), and type of PI were the variables investigated. Based on confocal images of P0 and P3 tendons acquired after these treatments and the same immunostaining protocol, decellularizing of postnatal tendons was performed by incubating samples in 8mL 0.05% SDS with 1× Halt PI and SDS-PI solution was replaced every 24 h for 7 days (**Fig. 5.12**). Completion of decellularization was determined by subjective visual inspection of samples and when ECM visualization was enhanced after immunostaining (**Fig. 5.2**)<sup>115</sup>. Upon decellularization,

samples were rinsed in an excess of 1× PBS for 1 hr and then incubated in blocking buffer [10% donkey serum (Lampire) diluted in 1× PBS with 0.1% Triton X-100 (PBST)] for 16h at 4 °C to increase permeability and block non-specific binding. Samples were then incubated with a primary antibody against fibronectin (FN, 1:100; Sigma) and fibrillin-2 (FBN2; 1:200; donated by R. Mecham) or type I collagen (1:200; Millipore) diluted in blocking buffer at 4 °C for 48h with gentle rocking. Samples were then rinsed 3×30 minutes with 0.1% PBST at room temperature, then incubated with AF633 donkey anti-rabbit (1:500; ThermoFisher) to visualize either anti-FBN2 or anti-type I collagen, AF555 goat anti-mouse (1:500; ThermoFisher), and AF488-conjugated wheat germ agglutinin (WGA; 1:100; ThermoFisher) to visualize proteoglycans, diluted in blocking buffer, at 4 °C for 48h. Next, samples were rinsed 3 × 30 min with 0.1% PBST at room temperature and stored in PBS at 4 °C in a lightproof container until imaging. Preliminary confocal imaging on an inverted Zeiss 880 confocal showed successful visualization of independent networks along the entire E16.5 tendon showing the spatial distribution of type I collagen, FBN2, FN, and proteoglycans (**Fig. 5.2**).

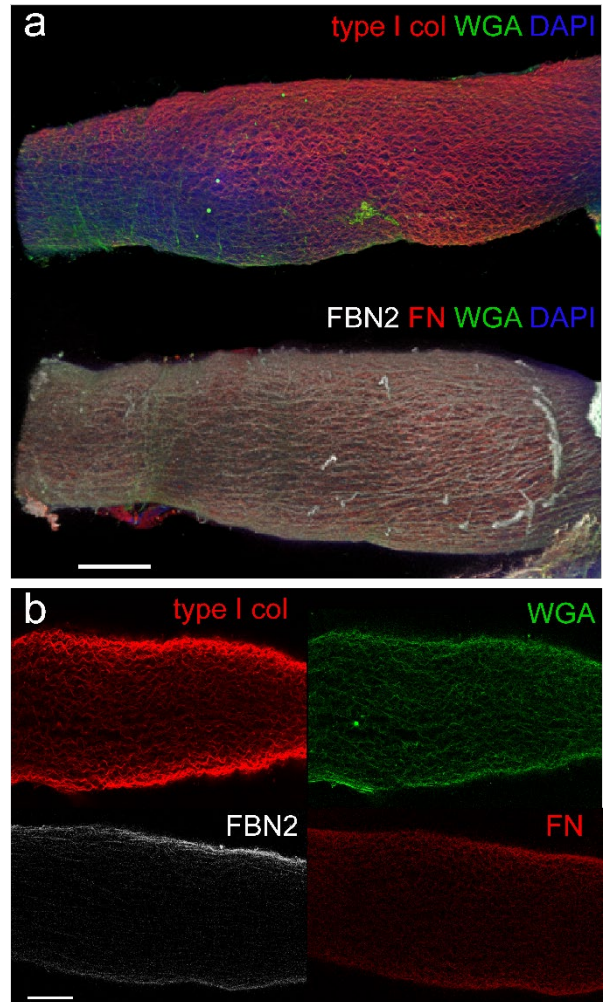


Figure 5.2. **a.** Representative 3D confocal rendering of TA immunostained to visualize ECM networks at 10x (bar=100  $\mu$ m). **b.** IHC shows independent ECM networks with distinct fibril 3D organization in the developing tendon at 10x (bar=50  $\mu$ m).

### 5.3.2 Preliminary uniaxial loading on confocal microscope

PET frames and a custom-made translating stage were designed to uniaxially load E16.5 decellularized tendons while on an inverted confocal for ECM imaging under tension. A ½'' linear translation stage with a differential adjuster (MT1A, Thor Labs) was mounted

on a custom plate allowing the setup to fit in a standard confocal stage. A fixed pin was used to keep in place the movable end of the PET frame the TA is attached to by the bone insertion. The translating pin was attached by the muscle insertion side. With the use of the differential adjuster, the stage moved the translating pin away from the fixed end (**Fig. 5.3a**). The PET frame + TA was coupled to the pins with a hole for either of the pins to go through. The use of two pins adjustable pins allowed the system to adapt to samples of varying lengths, as well as prevent the samples from floating once surrounded with PBS to keep hydrated during imaging. A loading well was created with polydimethylsiloxane (PDMS) cured on a glass-bottom coverslip to limit sample movement to the direction of load. For instance, AF488-labeled fibrin cast between porous polyethylene anchors was axially loaded on translating stage set-up and imaged at 10 $\times$  to visualize gel deformation (**Fig. 5.3b**). Preliminary experiments allowed the visualization of different ECM networks under tension (**Fig. 5.4**). Displacement fields were obtained with a fast-iterative digital volume correlation (FIDVC) algorithm and showed heterogenous deformation along the tendon and different displacement patterns for each network (**Fig. 5.5**)<sup>116,152</sup>.

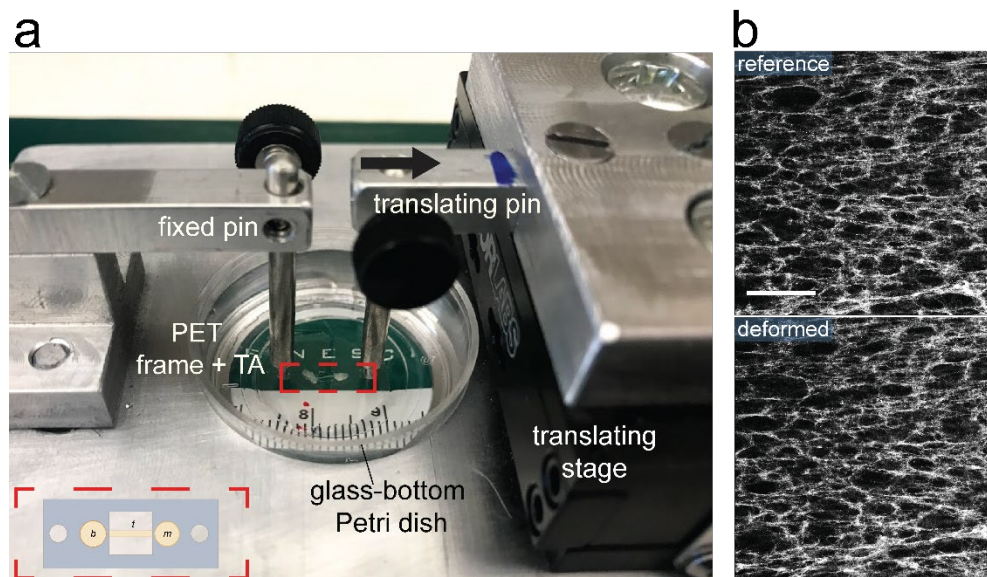


Figure 5.3. **a**. Custom micromanipulator-based set-up to image network deformation for an inverted confocal microscope with a representative PET frame-TA sample (dashed box). Schematic shows the location of the bone (fixed end) and muscle insertions (movable end) on the PET frame. **b**. Visualization of fibrin gel deformation. AF488-labeled fibrin cast between porous PE anchors was axially loaded on micromanipulator-based set-up and imaged at 10 $\times$  with an inverted confocal (bar=200 $\mu$ m).

Tendons were imaged using an inverted Zeiss LSM 880 confocal (Carl Zeiss Microscopy) and a 10× water immersion C-Apochromat (NA = 0.45) objective. In order to calculate engineering strain, lines were photobleached onto the immunostained samples to be used as fiducial markers. Using the *Crop* function in the Zen 2.3 (blue edition) software, rectangular areas of 5-10 μm in width and along the width of the tendon were drawn in order to photobleach 5 equidistant lines. The lasers were set to 50-100% power and by acquiring a z-stack along the entire sample thickness a line was photobleached into each of the ECM channels. After photobleached lines were generated, the reference z-stack of the entire tendon was acquired (**Fig. 5.6a**). Tension was applied by moving the translating pin away from the fixed end and visually inspecting changes in the distance between photobleached lines. During the first loading cycle, a reference z-stack was acquired and then tendons were uniaxially deformed to a target strain of 0.05, based on visual inspection of the distance between lines, and held at that position during z-stack acquisition of the same ROI. The sample was then brought back to the reference configuration using the differential adjuster and a z-stack was acquired to investigate the residual strain left in the ECM protein networks. Similarly, during the second cycle, the sample was uniaxially loaded to a 0.1 target strain and unloaded towards the reference configuration with  $566.8 \times 566.8 \times 42.8 \mu\text{m}^3$  z-stacks acquired at each of these configurations (**Fig. 5.6a**).

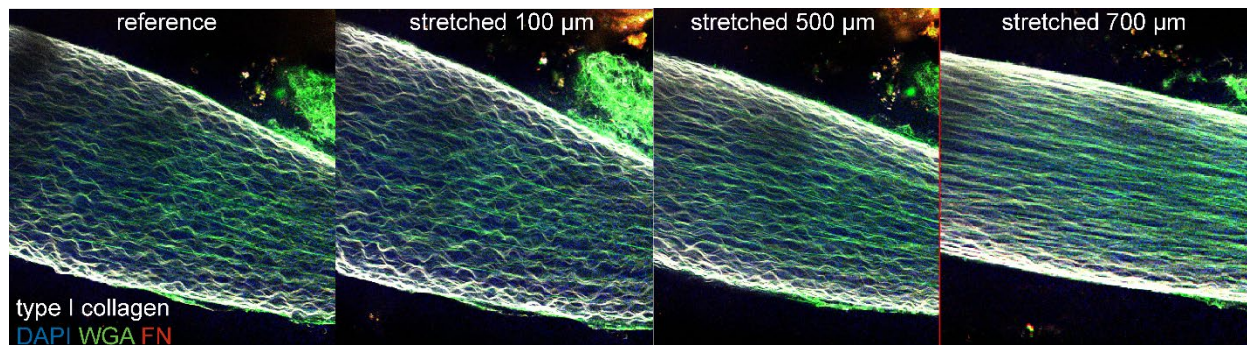


Figure 5.4. Preliminary experiments allowed the visualization of different ECM networks under tension. Z-stacks acquired at 10×.

Image processing was performed using FIJI (NIH) and MATLAB (MathWorks). Initially a MATLAB-based FIDVC algorithm was used to calculate tensile strain. The FIDVC algorithm also allowed the calculation of the maximum principal strain ( $E_1$ ) based on the calculated displacement fields<sup>152</sup>. The average  $E_1$  for type I collagen was 0.27, 0.29 for FN, and 0.21 for the

proteoglycans visualized with WGA. To investigate if FIDVC was the appropriate algorithm for uniaxial strain calculation, FBN2 z-stack were digitally strained to known values (0.05, 0.1, 0.15, 0.2) and ran through FIDVC. The obtained displacement fields presented high displacement error for strains ( $\epsilon_{xx}$ ) greater than 5%. As a result, a custom algorithm was written to instead calculate strain based on the change in distance between each pair of photobleached lines. First, *Nearest Neighbor Deconvolution* was performed within the ZenBlue software package (Carl Zeiss Microscopy) to remove some of the optical distortion inherent to confocal microscopy. The FN, WGA, and FBN2 or type I collagen channels were separated using FIJI. Each channel was processed with the filter *Gaussian Blur 3D* followed by *Find Edges* to enhance the contrast between the ECM network and the edges of the photobleached lines. Images were then opened in MATLAB as intensity arrays and their inverse was calculated. Next, the user was prompted to draw rectangles capturing each of the lines. Then, the minima of each row in these sub-arrays was found and determined to form the centerline of the photobleached line. The coordinates for the center of each photobleached line were saved and used to calculate the *in situ* engineering strain between two lines, using the average horizontal distance between lines across individual z-stacks (*i.e.*  $L-L_0/L_0$ ; **Fig. 5.6b**). The mean strain value along each sample was calculated in MATLAB and then compiled in GraphPad Prism 7.03 (GraphPad Software) for plotting and statistical analyses. Average strains across biological replicates ( $n=3$ ) are plotted as well as their mean and standard deviation (**Fig. 5.8**). Strains calculated from samples immunostained to visualize FN, type I collagen, and proteoglycans were similarly analyzed. An overlay of representative type I collagen and FBN2 using *3D Viewer* (FIJI) shows different network organization of proteins and as a result of loading (**Fig. 5.8**).

### 5.3.3 Uniaxial loading using micromanipulator system on confocal

After preliminary investigation of ECM network deformation resulting from uniaxial loading, our laboratory customized a commercially available FemtoTools micromanipulator system (FT-RS1002; **Chapter 4**) to perform uniaxial loading and characterize mesoscale mechanics of the ECM. The system was designed around custom 3D printed springs and hooked microforce sensors to connect the micromanipulator and the spring for the indirect coupling to the sample. The design of the spring and the hooked sensor allowed the PBS to be away from the electronics to prevent water damage while also keeping the sample hydrated during testing and

imaging. Our system was mounted on a Zeiss 800 upright confocal (Carl Zeiss Microscopy) to visualize the ECM during tensile testing (**Fig. 5.7**). In order to level the micromanipulator with the microscope stage and keep it from translating during testing, a custom platform was machined to be compatible with optical table the system is on. E16.5 TAs were dissected, glued onto  $4 \times 6 \text{ mm}^2$  frames laser cut out of  $100 \mu\text{m}$ -thick polyethylene terephthalate (PET), and decellularized before immunostaining to visualize fibrillin-2 (FBN2), and a subset of proteoglycans with wheat germ agglutinin (WGA). Prior to tensile testing, the sample was placed on the appropriate 3D printed spring, and the PET frame was cut to allow the sample to move during testing.

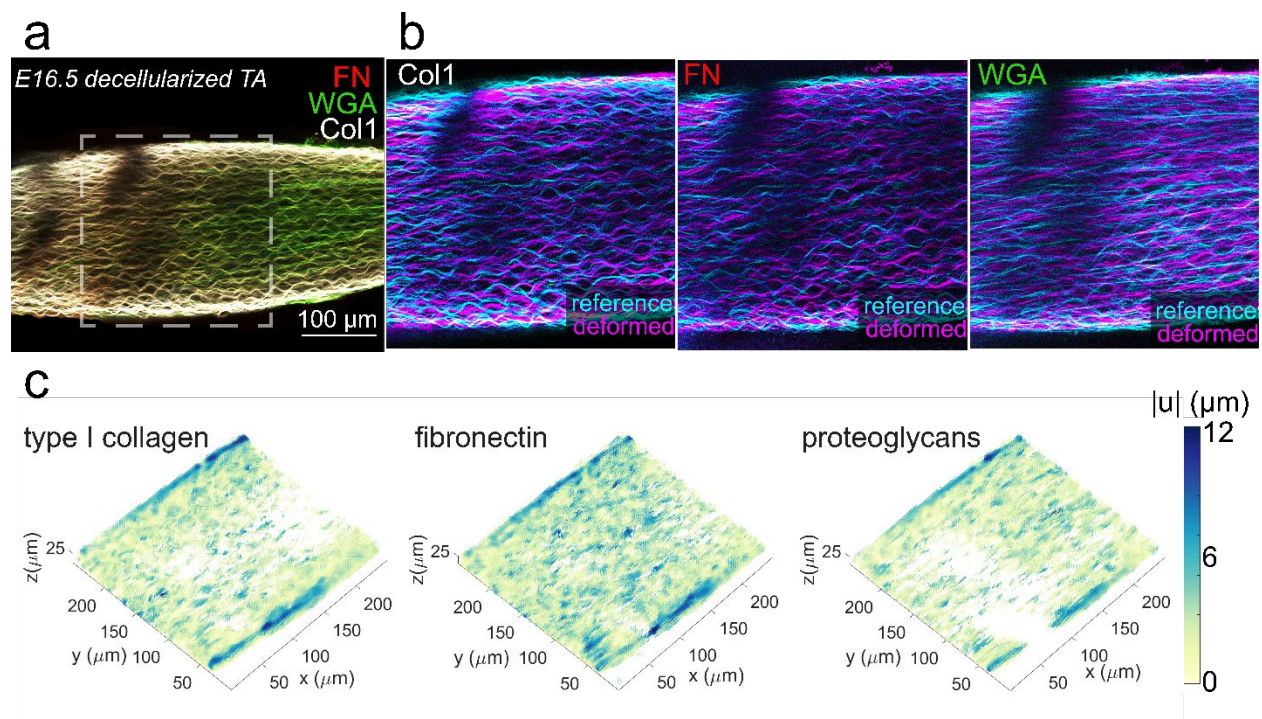


Figure 5.5. **a.** E16.5 Decellularized TA imaged with a  $10\times$ W objective after stretching the tissue with micromanipulator translating stage. **b.** Composites show an overlay of the reference (blue) and deformed (magenta) networks of type I collagen, fibronectin, and WGA. **c.** Resulting displacement fields from relating the references and uniaxially loaded configurations using FIDVC.

A  $20\times$  water immersion Plan-Apochromat ( $\text{NA} = 1.0$ ) objective was dipped in the PBS to come in close contact with the sample in order to locate it and position the stage ( $xyz$ ) accordingly for imaging (**Fig. 5.7**). In this system, the stage translates during image acquisition and the objective remains fixed. A region of interest of  $20 \mu\text{m}$  in width was drawn along sample width using the Zen software's *Crop* feature. Equidistant lines between the muscle and bone insertions

were photobleached onto the samples as fiduciary markers for the calculation of regional engineering strain. The 488 laser power was set to 100% and by acquiring a 40.3  $\mu\text{m}$  z-stack towards the center ( $z$ ) of the tendon in 1.09  $\mu\text{m}$  increments, a line was photobleached into the AF488 WGA stained tissue. After photobleached lines were generated, the middle region of the tendon was imaged by acquiring a z-stack, given that at this  $z$  position the entire length of the tendon was visible. The hooked microforce sensor was carefully attached to the PET 3D printed spring interface while the spring was on the stage and the objective was over the sample (**Fig. 5.7**). Uniaxial loading was conducted at  $0.01\text{s}^{-1}$  strain rate, force measurements were recorded at 100Hz, and z-stacks were acquired before and while in a loaded configuration (**Fig. 5.9**). The  $20\times$  objective at a 0.3 magnification allowed the acquisition of  $638.9\times 638.9\times 21\ \mu\text{m}^3$  in  $\sim 3$  minutes, with a voxel size of  $0.31\times 0.31\times 1.09\ \mu\text{m}^3$ .

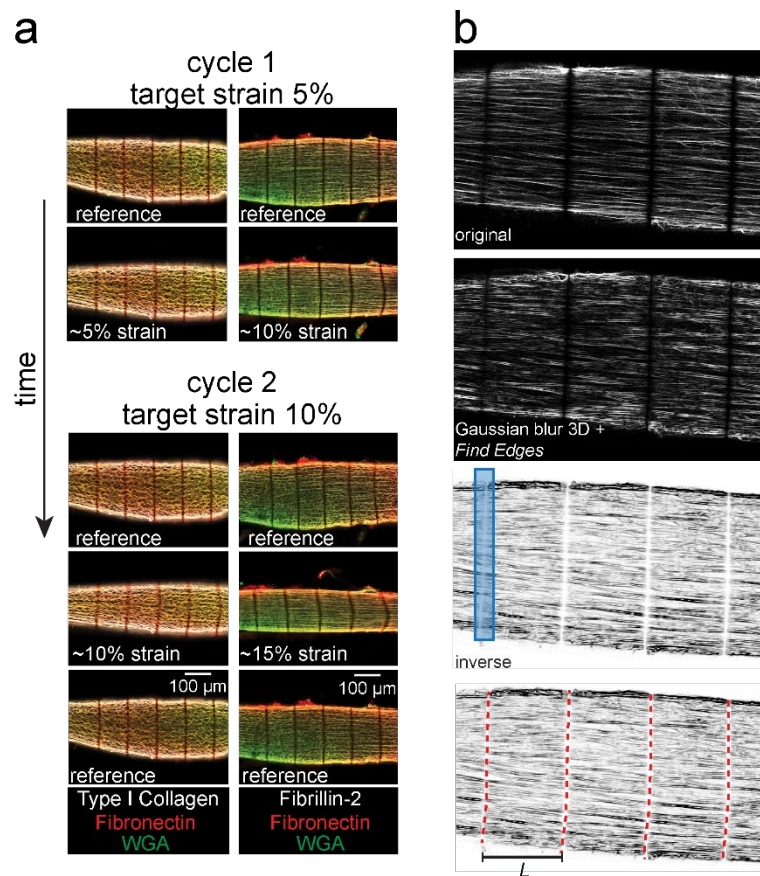


Figure 5.6. **a.** Representative confocal images for E16.5 tendons visualizing CollI, FBN2, FN, and WGA during 2 loading cycles using a customized translating stage and an inverted confocal. Z-stacks were acquired at  $10\times$ . **b.** Image processing for the calculation of engineering strain using FIJI and MATLAB based on photobleached lines.

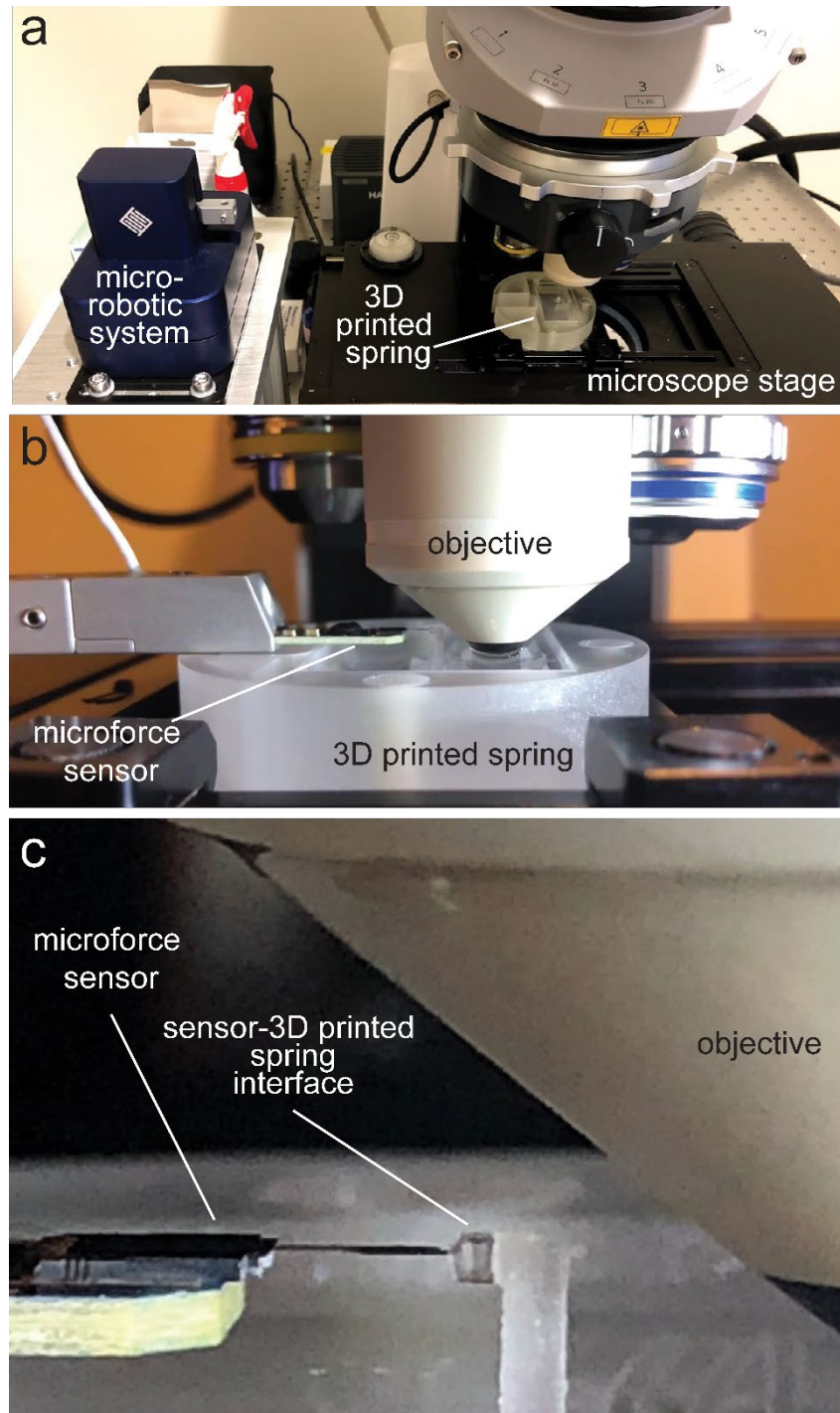


Figure 5.7. Adapting FemtoTools micro-robotic system to Zeiss 800 upright confocal for the visualization of immunostained ECM networks. **a.** A platform was machined to match the height of the microscope stage. **b.** The 3D printed spring is the same size as a 60 mm Petri dish, fitting well on the microscope stage. **c.** Sensor-3D printed spring interface and pillar do not interfere with objective.

### 5.3.4 Ultrastructure of embryonic and postnatal tendons

In order to investigate collagen fibril diameter distribution as a function of development and as a result of decellularization, transmission electron microscopy (TEM) images were acquired. After excision, TAs (muscle-tendon-bone units) were placed in chilled PBS and then fixed in 2 mL of 2% PFA and 2% glutaraldehyde in 0.1 M cacodylate buffer overnight at 4°C. P3 (n = 3) and E18.5 (n = 3) tendons samples were processed by the Purdue Life Science Microscopy facility as follows. Fixed samples were rinsed with cacodylate buffer, stained with 2% aqueous uranyl acetate for 30 min, and rinsed again with water. Samples were then ethanol dehydrated and transitioned to acetonitrile before infiltration with Embed 812 (Electron Microscopy Sciences) and acetonitrile rotating overnight, and resin for 3 hours rotating. Samples were embedded in flat molds and cured overnight at 70°C in fresh resin. Ultrathin sections were cut along the short-axis of the tendon at 85 nm with a 45-degree diamond knife (Diatome USA) on a UC6 ultramicrotome (Leica) and collected on 100 mesh formvar-coated copper grids and post stained in 4% aqueous uranyl acetate and 2% aqueous lead citrate. Transverse sections were imaged on a FEI T12 80kV TEM (FEI Company) in the Purdue Life Science Microscopy core facility.

Acquired images were processed using FIJI following Starborg *et al.*<sup>156</sup> in order to quantify fibril diameter. In brief, the threshold of each image was adjusted, followed by *Convert to Mask*. Each image was then processed with *Erode* and *Fill Holes*. Then, the images were made binary using *Watershed*. FIJI's *Analyze Particles* was then used and an ellipse was fitted to each of the fibrils in the image (**Fig. 5.10**). The minor diameter of each ellipse was then counted as the fibril diameter. Fibril diameter distribution in 3 technical replicates was calculated in MATLAB (MathWorks) for 3 samples (n = 3) for P3 (**Fig. 5.10**) and E18.5 (**Fig. 5.11**). Fibril diameter distribution values were then input to GraphPad Prism for plotting and statistical analyses.

## 5.4 Results

The methodologies and studies described present the foundation for the quantification of strain under uniaxial loading for the characterization of ECM networks *in situ* by combining confocal microscopy and tensile testing. In order to do so, decellularization protocols were adapted from those previously published and used for ECM visualization of embryonic and postnatal tendons<sup>78,115</sup>. Initial stretching showed an elongation of type I collagen fibers when a stretch of 700  $\mu\text{m}$  was imposed, or until the collagen fibers appeared almost straightened (**Fig. 5.4**). By using

a translating stage and an inverted confocal, ECM strain under uniaxial loading was quantified. The prescribed and residual strains for FN, type I collagen, and proteoglycans were calculated using the coordinates of photobleached lines for each protein. An unpaired t-test indicated significant differences in the residual strains corresponding to FBN2, type I collagen, and proteoglycans after loading cycle 1 compared to cycle 2 (**Fig. 5.8**).

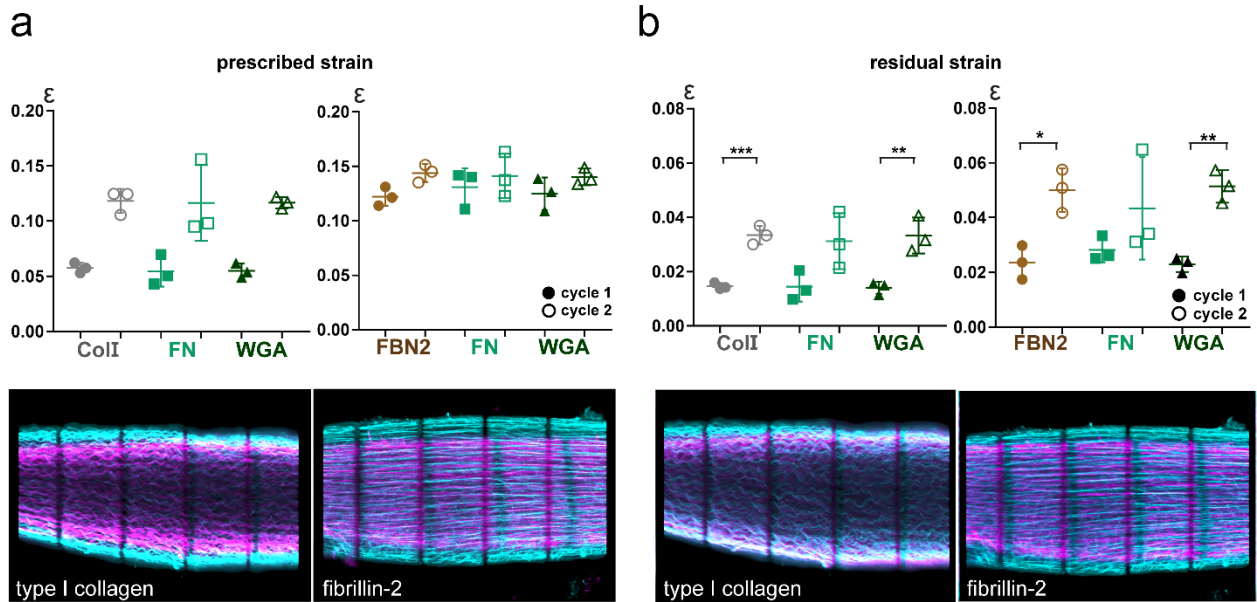


Figure 5.8. Calculated prescribed (**a**) and residual (**b**) strain over 2 loading cycles corresponding to ECM protein networks for different locations along tendons averaged across biological replicates ( $n=3$ ; bars = S.D;  $*0.0021 < p \leq 0.0332$ ;  $**0.0002 < p \leq 0.0021$ ,  $***0.0002 < p \leq 0.0001$ ) and a representative overlay of ColI and FBN2 before, during (**a**) or after (**b**) load.

The residual strain indicates how an ECM protein network recovers to the displacement prescribed, with FN being more extensible, or able to successfully recover after loading, when compared to type I collagen, FBN2, and proteoglycans visualized with WGA (**Fig. 5.8**). The lower residual strain on FN could be related to its biological numerous functions, such as interacting with other ECM proteins and functioning as a medium for force transmission, influencing the assembly of other ECM proteins, and acting a lubricant for shear<sup>37,157</sup>. Further, this can be related to the measured extensibility of FN when others have tested single fibers, showing these soft fibers are capable of full recovery of material properties after deformation ( $\sim 700\%$  strain)<sup>111,136,158</sup>. However, the reported mechanical behavior for FN varies depending on the isolation and testing protocols the fibers were evaluated under. Further, FN fibers could have a different mechanical

behavior *in situ* while interacting with other components of the microenvironment. The overlays of the reference z-stack and the z-stack after the second loading cycle, show residual strain given that the networks before and after loading do not completely overlap (**Fig. 5.8**). The residual strain could be an indicator of plastic deformation since networks are not able to successfully return to their pre-stressed state. The tissue might have been loaded beyond physiological strain in order to achieve a network strain of 0.1, leading to this deformed state.

To investigate ECM strain and record force measurements during tensile testing, we successfully adapted the FemtoTools micro-robotic system to an upright confocal. The adaptation and set-up were facilitated with the use of a custom-made platform to match the height of the FemtoTools system to that of the microscope stage. Testing time is critical when studying viscoelastic tissues. During imaging, the decellularized E16.5 tendon showed stress relaxation, indicated by the exponential decay in the recorded force, when held in tension. Successfully adapting our micromanipulator + 3D-printed spring system for compatibility with an upright confocal allowed the visualization of FBN2 and WGA (not pictured) networks during tensile testing (**Fig. 5.9**).

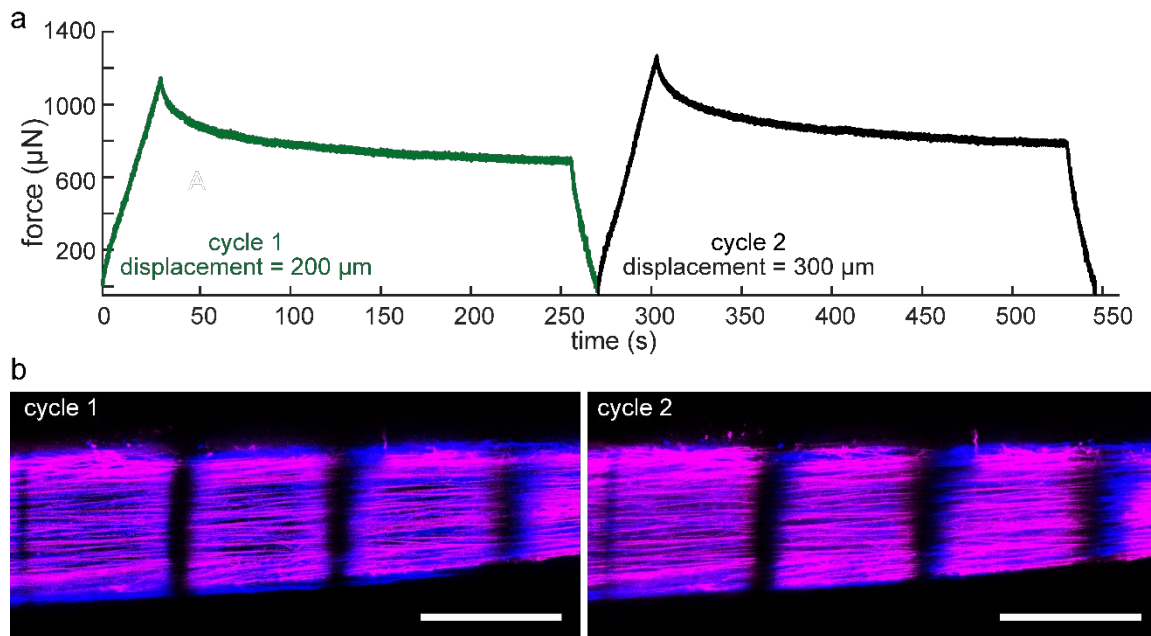


Figure 5.9. Force – time curve recorded during 2 cycles of uniaxial loading of a decellularized E16.5 TA tendon immunostained to visualize FBN2 during testing. b. FBN2 networks in the reference (blue) and deformed (magenta) configurations for cycles 1 & 2 (bar =100  $\mu\text{m}$ ).

Investigating the ultrastructure with TEM allowed the quantification of fibril diameter in embryonic (E18.5) and postnatal (P3) tendons. Biological replicates showed the variability within samples when the fibril diameter distribution was plotted (**Fig. 5.10**). The average type I collagen fibril diameter in P3 tendons was  $47.5 \pm 1.7$  nm, while  $39.9 \pm 0.7$  for fibrils in E18.5 tendons. The average and standard deviation were calculated over 3 biological replicates, along with 3 technical replicates for each. Technical replicates show the variability of distribution within one tendon sample (**Fig. 5.10, 5.11**). A t-test showed significant differences between in the mean fibril diameter between two time-points. Collagen fibril diameter may indirectly affect mechanics (stiffer tendon) due to fibril-fibril interactions or fibril-non-fibrillar matrix interactions. Similar analyses on embryonic mouse tail found a mean fibril diameter of  $35.4 \pm 0.2$  nm at E15.5 and  $46.5 \pm 1.1$  at P0<sup>159</sup>. Our results for E18.5 align with those previously published since both the mean fibril diameter value and the stage of development are in between E15.5 and P0.

## 5.5 Discussion

The results presented here demonstrate the potential for our method to resolve ECM deformation and strain *in situ* and characterizing ECM networks through confocal microscopy of immunostained embryonic tendons. Using embryonic tissues as a model system makes it easier to visualize and manipulate ECM networks while in their native configuration. Embryonic tissues are ideal model systems because the ECM architecture is less dense compared to most adult tissues, especially connective tissues that tend to be comprised of mostly ECM networks and low cellular content, with individual networks that are difficult to extract. Image processing was used to obtain ECM network strain in the direction of load, as others have often used along with fiducial markers<sup>132,160</sup>. Mechanical testing systems have often been coupled to other instruments to visualize ECM deformation as a result of tissue load<sup>71,74,161</sup>. However, *in situ* characterization of ECM networks oftentimes only looks at one protein or makes assumptions on the ECM content of the tissue (*i.e.* tendons are mostly made up of type I collagen so mesoscale analyses only considers these fibrils)<sup>74,162</sup>. By investigating multiple discrete ECM components, we are able to gather information and better inform future tensile testing; for instance, how applied tissue displacement translates to ECM strain. Despite some limitations, these studies provide the foundation for the *in situ* characterization of the cellular microenvironment.

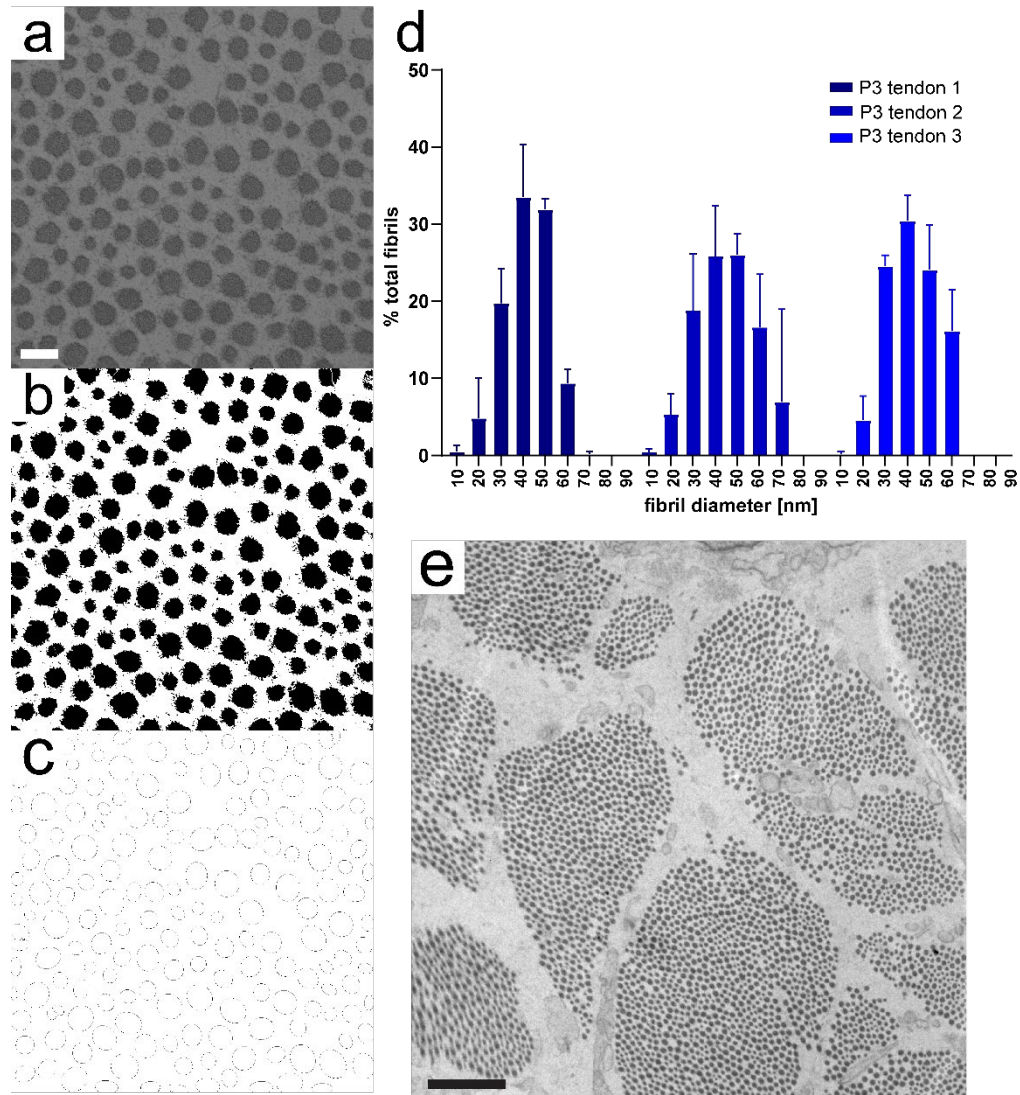


Figure 5.10. TEM image analysis and type I collagen fibril diameter results in P3 tendons. **a.** Representative type I collagen fibrils acquired at 68,000 $\times$  (bar=100 nm). **b.** Binarization of the image in (a) using thresholding in FIJI. **c.** Ellipses fitted to the fibrils in (a) to quantify fibril diameter. **d.** Distribution of fibril diameter for each sample across technical replicates (n=3; bars= S.D). **e.** Overview of fibril bundles acquired at 6,800 $\times$  (bar = 1 $\mu$ m).

Dissecting embryonic tendons successfully is an important first step to enhance repeatability of mechanical testing. Although the TA runs anterior to the foot and can be easily located under a dissecting scope, care has to be given to avoid tissue damage during dissection. An important consideration is keeping a hold of the hindlimb while removing the skin and connective tissue. If the hindlimb is not properly secure, the TA can be pinched or torn from the insertions. Using fine tweezers provided more control to remove connective tissue keeping the

tendon attached to the foot. The 11-blade provided a flat surface to insert under the tendon to separate it from the foot, as well as the tibialis anterior muscle from the bone in order to keep it intact. The size of the insertion was adjusted keeping in mind the size of the PET frame and allowing enough tissue for the glue to interface to keep the tendon secure. The amount of glue and the size of the insertions is qualitatively determined (*i.e.* performed manually according to visual inspection), which can lead to sample disruption by the surrounding glue when not performed properly. Therefore, it is important to inspect the sample soon after it is placed in a high volume of chilled PBS to remove any slight amount of glue that might have gotten on the surface of the tendon.

Decellularization was performed to enhance ECM visualization and retain independent networks. Previous work showed the structure of FN and FBN2 within control tissue could not be visualized beyond the surface (**Fig. 2.2**)<sup>115</sup>. Initial decellularization experiments of embryonic and postnatal tendons showed similar results when staining with WGA; proteoglycans could not be visualized in embryonic tendons a few microns past the surface. Proteoglycans serve several functions including to modulate collagen fibril diameter during fibrillogenesis, and cooperate with growth factors to regulate cell proliferation<sup>125</sup>. Treatment with SDS has been confirmed to not interfere with the spatial organization of the ECM. Cryosectioning of control E14.5 forelimbs showed similar fibrils to those imaged in decellularized limbs (**Fig. 2.9**), indicating the architecture visualized was likely not an artifact of decellularization<sup>115</sup>. Previously, an interpenetrating hydrogel network was used for support while keeping the ECM intact when decellularized E12.5 and E14.5 embryos and tissues. As expected, at later developmental stages, the stabilization of the geometry using the hydrogel appears to be unnecessary. Nonetheless, detergents may disrupt these fibrillar structures if delicate embryonic samples are decellularized for too long. The presence of a polyacrylamide framework would have likely influenced ECM deformation and increase the overall rigidity of the embryonic tissues, thus interfering with the characterization of ECM network mechanical properties. Similarly, to avoid increasing intrafibrillar crosslinking, the tissues were not fixed with 4% paraformaldehyde (PFA) prior to immunostaining. Therefore, all imaging and tensile testing was conducted immediately after. However, future work towards understanding how decellularizing with low concentrations of SDS might affect the ECM in developing tissues is needed. Preliminary proteomic analysis of E14.5 control and decellularized skin showed a decrease in the relative amounts of proteins such as type I collagen and FN (**Appendix B**). Thus,

a comprehensive analysis of the relative amounts in control and decellularized tissues needs to be conducted. Additionally, further ultrastructure analysis could also inform how decellularization affects type I collagen fibril diameter and area.

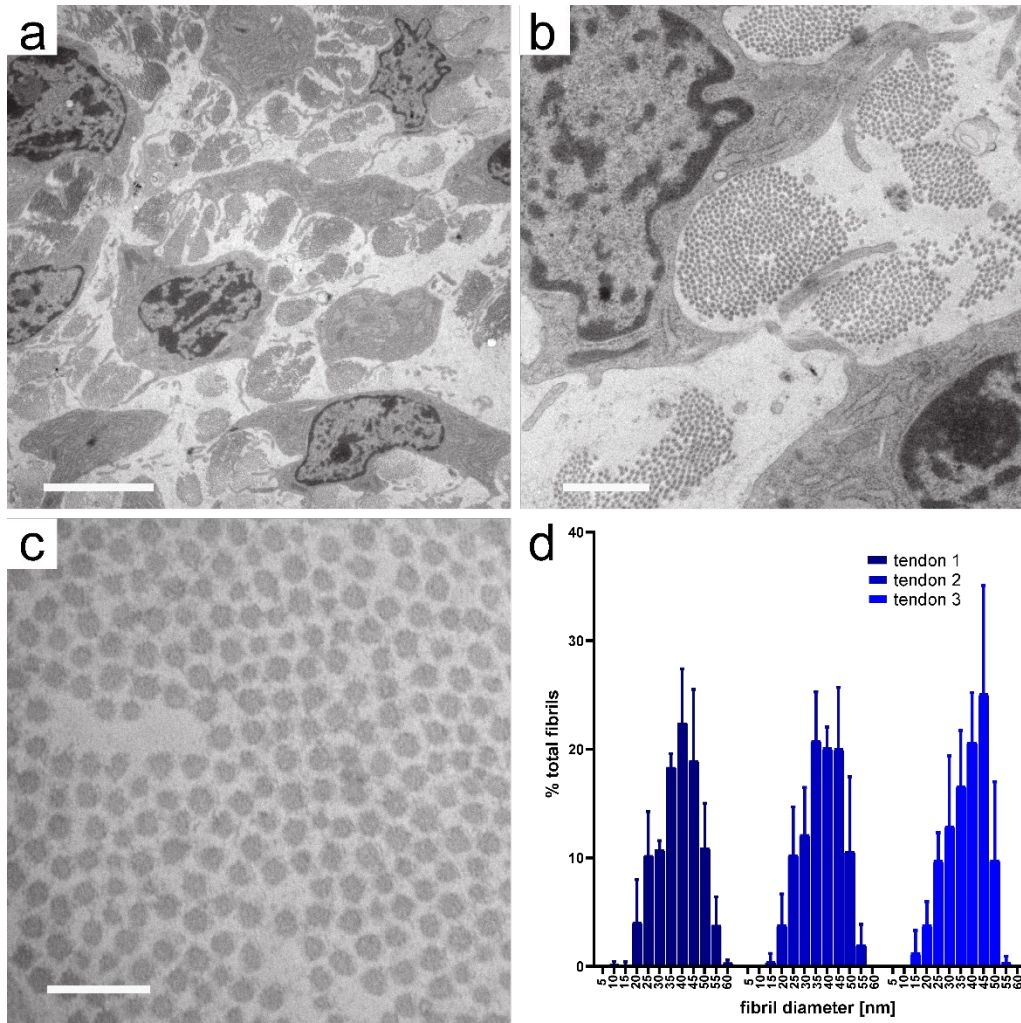


Figure 5.11. Ultrastructure of E18.5 tendons. **a.** Overview acquired at 2,550 $\times$  (bar=5 $\mu$ m). **b.** Fibril bundles imaged at 9,900 $\times$  (bar=1 $\mu$ m). **c.** Representative type I collagen fibrils acquired at 68,000 $\times$  for diameter quantification (bar=200 nm). **d.** Distribution of fibril diameter for each sample across technical replicates (n=3; bar=S.D.).

To enhance ECM visualization in postnatal tissues, different SDS concentrations and protease inhibitors were tested. Successful decellularization of postnatal tendon was determined based on visualization of independent ECM networks (*e.g.* FBN2, proteoglycans) and by the observed increase in tissue transparency (**Appendix B**). Staining for nucleic acids (DAPI) indicated that tissues were not fully decellularized; nevertheless, the ability to resolve ECM

architecture was greatly enhanced even with the presence of residual DNA (**Fig. 5.12**). The presence of DNA chains may influence mechanics and may be avoided in the future by incorporating enzymatic methods to the decellularization treatment such as DNase to help remove nucleotides after cell lysis<sup>81,163</sup>. Despite becoming denser, the optimal decellularization protocol for postnatal tendons used the same concentration (0.05%) and protease inhibitors as used on tissues earlier developmental stages only for a greater time period. The proteoglycan network imaged by staining with WGA appears to be denser than in embryonic tendons, as others have shown for postnatal development<sup>125</sup>. Additional optimization might be needed given that FN could not be resolved, potentially due to antibody penetration in these denser samples. FN is known to be a part of the tendon ECM, prevalent within the interfibrillar space, acting to maintain ECM assembly<sup>31,65</sup>. Consequently, a more stringent decellularization process might be needed to visualize FN without disrupting other ECM components we are also interested in characterizing (*e.g.* FBN2) and that contribute to the mechanics of the microenvironment. Visualizing the ECM in postnatal tissues is of interest to eventually investigate how the ECM architecture changes as a function of development. To study ECM network mechanics, E16.5 TA is therefore the ideal model system given its sparser network and better ECM visualization past the surface. Additionally, the smaller dimensions at this earlier timepoint allows for a shorter imaging time. We expect to be able to extrapolate these results and relate them back to the ECM of adult, bypassing the need to visualize and experimentally manipulate much denser and larger tissues.

The homogenous geometry of the TA made it possible to load under physiologically relevant conditions. In immunostained E16.5 tendons, we can visualize the distribution and architecture of type I collagen, FN, FBN2, and proteoglycans. In immunostained E16.5 tendons we visualize a waviness to type I collagen fibers, (**Fig. 5.2, 5.4**) that straightens out as the fibers are under tension. Others have reported the observed wavy pattern in unstrained tendons and a similar phenomenon when looking at adult tendons with multiphoton microscopy, as strain causes the straightening and alignment of individual collagen molecules in the fiber<sup>54,64,164</sup>. During the initial 100 micrometers of stretching, no change in the collagen periodicity was observed, potentially due to the tendon being slightly compressed or bent in the initial state, which had to be straightened before stress was applied to the fibers. These initial experiments inform the amount of displacement that is appropriate to impose when looking to apply physiologically relevant strains to the ECM networks (~15%) and understanding the relationship between macroscopic

displacement and ECM network strain. Given high error obtained with FIDVC for uniaxial loading of these networks, generating fiducial markers enable the calculation of network strain, under the assumption that a great majority of the displacement occurs in the direction of load. Since the TA has the appropriate aspect ratio for uniaxial loading, we do not expect significant transverse strains. We do see the sample slightly decrease in their transverse dimension, as part of the Poisson effect.

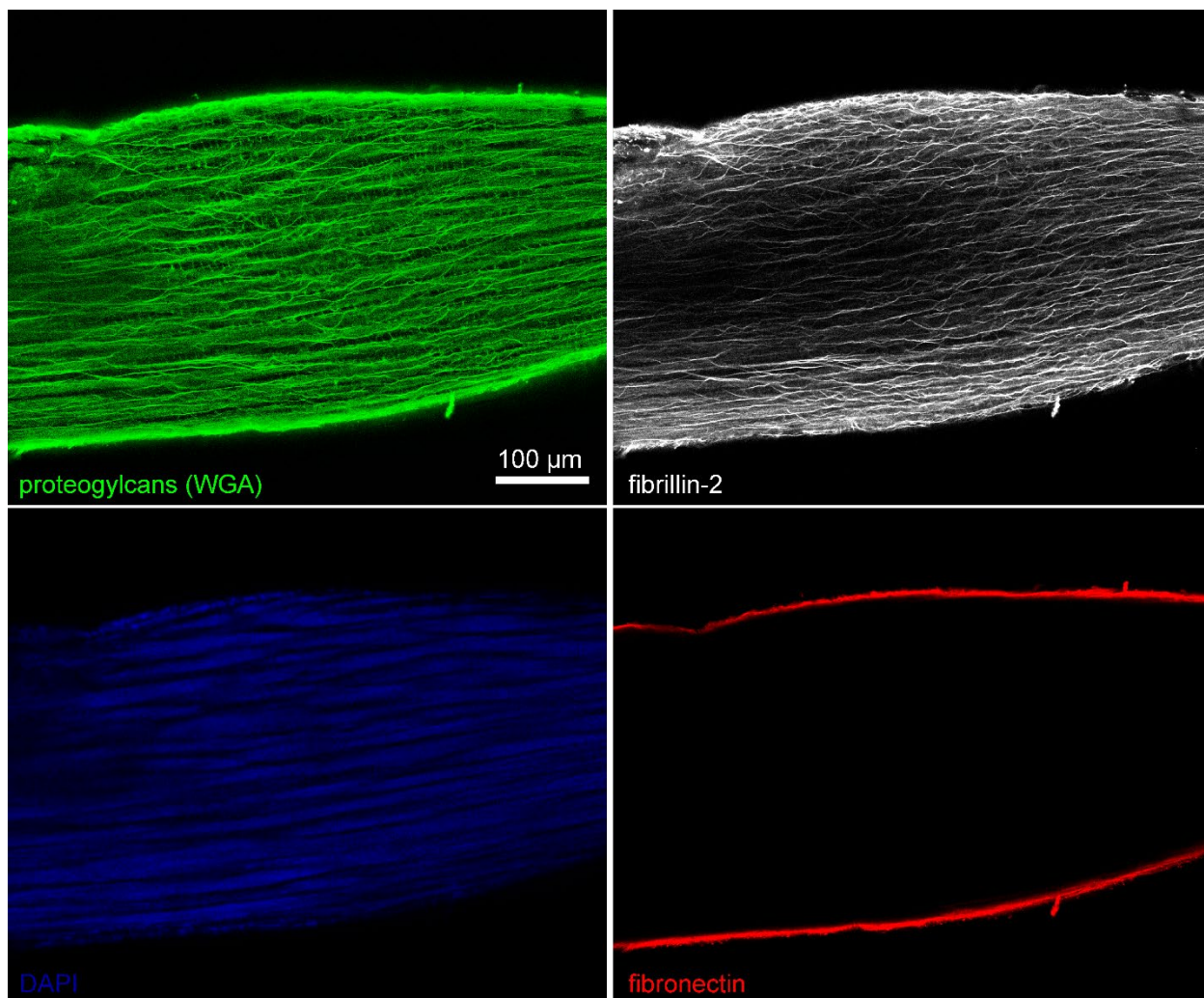


Figure 5.12. Confocal imaging of ECM networks in P3 tendons after decellularization by gentle rocking in a 0.05% and 1× PI solution for 7 days. Images acquired at 10×W.

Using a translating stage and photobleached lines we observed a discrepancy between *in situ* matrix stain and grip-to-grip strain (*i.e.* prescribed macroscopic displacement) such that calculated matrix strain was <30%, similar to what others have reported<sup>165</sup>. This could be a consequence of the limitations of our system or tearing along the glued interface between the

insertions and the PET frame. Additionally, attainment of target strain was determined via visual inspection using the *Live* feature, or the real time image shown via a quick scan, in the Zen software, which could have also led to greater ECM network strain than intended to. Further, the use of the differential adjuster for the application of stretch in fine (*i.e.* 20) coarse (*i.e.* 500) micrometers/rotation is also subject to error by the user. While the calculated strain values are within what is physiological<sup>20</sup>, the plastic deformation could come from the fact that they were held at this displacement during the length of the z-stack acquisition period. Perhaps greater recovery would be observed if these viscoelastic tissues were loaded at a more controlled strain rate and held in tension for less time. Under tension, we observed an increase in the curvature of photobleached lines, originally completely perpendicular (**Fig. 5.6, 5.8**). Others have quantified this deflection and attributed to *in situ* fiber sliding (*i.e.* deformation of interfibrillar structure) when uniaxially loading tendon fascicles<sup>74</sup>. The nonlinear mechanical behavior of tendon is thought to include the relative sliding of the subunits across scales, in addition to molecule, fibril, and fiber deformation<sup>160</sup>. The calculated residual strain could potentially relate to this non-recoverable sliding since others have shown a partial recovery in sliding might indicate tendon damage initiates at the interfibrillar structures<sup>74</sup>. Future quantification of the maximum horizontal distance between two pixels along each photobleached line would be needed to better understand how fiber sliding relates to ECM strain in decellularized embryonic tendons<sup>165</sup>.

The modular, high-precision micro-manipulator system we adapted has the ability to resolve forces and displacements relevant to the characterization of ECM network mechanics. With a displacement sensing range of 5 nm – 26 mm, we are able to apply precise displacements while recording force measurements ranging from 5 nN – 100 mN. To ultimately characterize these discrete ECM components, force recording is critical to build the equations and material parameters that describe their mechanical behavior. Our system allows mechanical testing while keeping the boundary conditions intact at the macro and mesoscale—critical for *in situ* characterization. As stress relaxation is expected to occur in a viscoelastic tissue such as tendon, imaging protocols will need to be optimized, since the ECM networks might also undergo stress relaxation<sup>165</sup>. Imaging time of high-resolution z-stacks increases depending on the number of channels acquired and voxel size. Imaging time should be minimized without compromising appropriate resolution for multiple ECM protein networks, particularly in the z-direction where the diameter of the fibers should be smaller than the z-step for acquisition to avoid missing

information on network geometry. Minimizing imaging time could help reduce the effects of stress relaxation. Quantifying the force relaxation as a function of the force measured is also a needed next step by acquiring z-stacks before and after each relaxation cycle to investigate how much each ECM network is relaxing during any given imaging time. This additional information would also help define the optimal sub-region dimensions by better understanding the viscoelastic response. Despite some limitations in data acquisition and analysis, our method provides a first step towards characterizing the material behavior of native ECM networks. By combining the acquired data from mesoscale and macroscale testing, constitutive equations and material parameters that describe the mechanical behavior of ECM networks *in situ* can then be identified. Quantifying the material properties of the native ECM will provide design parameters for physiologically relevant scaffolds that can direct cell behavior *in vitro* and *in vivo*, having a profound impact in mechanobiology and regenerative medicine.

## 6. CONCLUSIONS AND FUTURE DIRECTIONS

The goals of this dissertation were to develop experimental and computational methodologies to investigate the 3D organization and mechanical behavior of extracellular matrix (ECM) networks *in situ* in order to establish guidelines for microenvironments that facilitate tissue assembly. While significant efforts have been previously made in understanding the role of the ECM in disease progression and tissue formation, there remained an opportunity to explore the 3D organization and material behavior of ECM networks in their native conformation or *in situ*. In the completion of this work, we enhanced visualization of ECM networks during embryonic and postnatal development. We developed experimental and computation methods to quantify tissue-dependent ECM network strain, serving as proof-of-concept for the integration of confocal microscopy and digital volume correlation for the study of the embryonic ECM. We established modular mechanical testing systems to evaluate embryonic and postnatal tendon mechanics, as well as the mechanical behavior of soft biomaterials. Further, we investigated the ultrastructure to further understand the ECM and tendon mechanics as a function of development.

These methodologies and studies set the foundation for further investigations of tissue assembly and ECM network mechanics. A modular mechanical system allows the multiscale interrogation of a variety of biological questions that investigate the complexity and heterogeneity of tissues and their ECM. For instance, ECM network mechanics could be interrogated in embryonic tendons from a mouse model of osteogenesis imperfecta (Coll1a2<sup>-/-</sup>) to understand how a homotrimer collagen molecule impacts the ECM at the network and tissue scales. Additionally, the effect of tissue decellularization on ECM composition and ultrastructure needs to be investigated. Thorough proteomic analyses comparing fresh and decellularized tissues will need to be conducted for each developmental timepoint and tissue of interest. The influence of detergents could vary depending on the tissue type and dimensions. Further, criteria could be developed to determine when the incorporation of an interpenetrating network is needed to maintain tissue integrity in order to streamline the adaptation of the method for other tissues and investigations. This work serves as the foundation for establishing mechanical guidelines for microenvironments that facilitate functional tissue assembly and better recapitulating microenvironments found *in vivo*. Quantifying how the

material properties of the ECM change during growth and remodeling will have a profound impact in mechanobiology and regenerative medicine.

## APPENDIX A. SUPPLEMENT TO CHAPTER 4

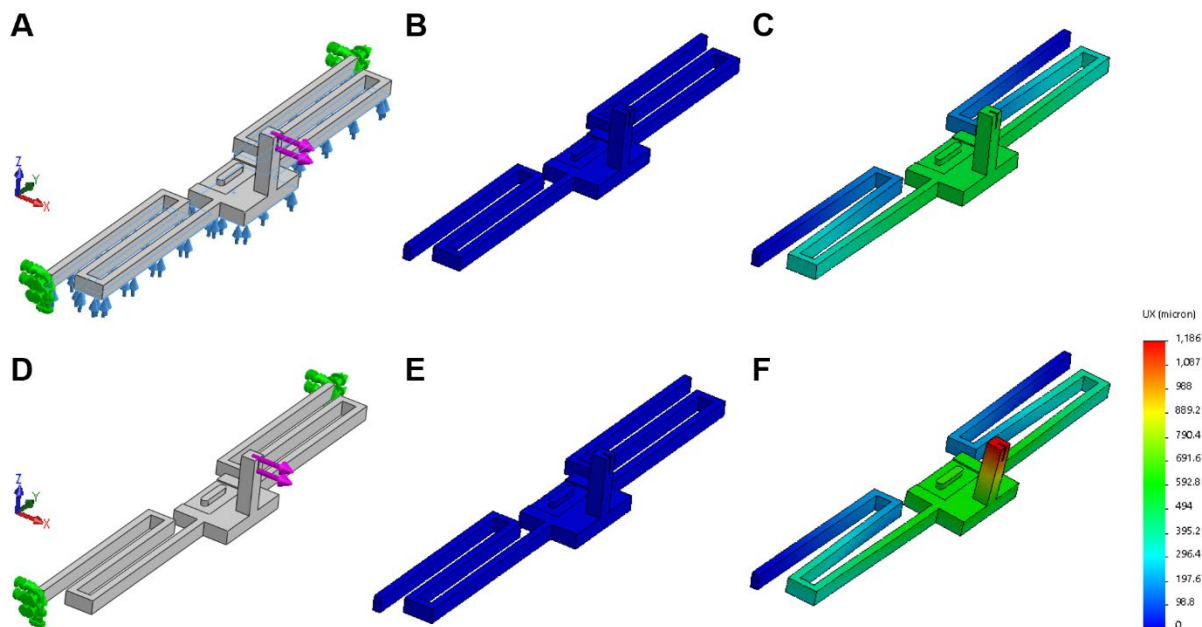


Figure A.1. SolidWorks assembly and finite element model simulations (mesh element size:  $125\ \mu\text{m}$ ). **A.** Fixtures for **B** and **C** – fixed geometry (green), roller/slider (blue); and external load of  $400\ \mu\text{N}$  (pink). **D.** Fixtures for **E** and **F** – fixed geometry (green), and external load of  $400\ \mu\text{N}$  (pink). **B, E.** Displacement results from simulations ran using the elastic modulus for M2R-CL polymer provided by the manufacturer. Material properties – Young's modulus: 1750 MPa, shear modulus: 625 MPa, Poisson's ratio: 0.4, yield strength: 3.5 MPa, mass density:  $1160\ \text{kg/m}^3$ , tensile Strength: 40 MPa. **C, F.** Displacement results from simulations ran using the elastic modulus obtained from empirical force-displacement data to calculate the stiffness of the M2R-CL 3D-printed spring. Material properties – Young's modulus: 20 MPa, shear modulus: 7.2 MPa, Poisson's ratio: 0.4, yield strength: 0.04 MPa, mass density:  $1160\ \text{kg/m}^3$ , tensile strength: 40MPa.

## APPENDIX B. SUPPLEMENT TO CHAPTER 5

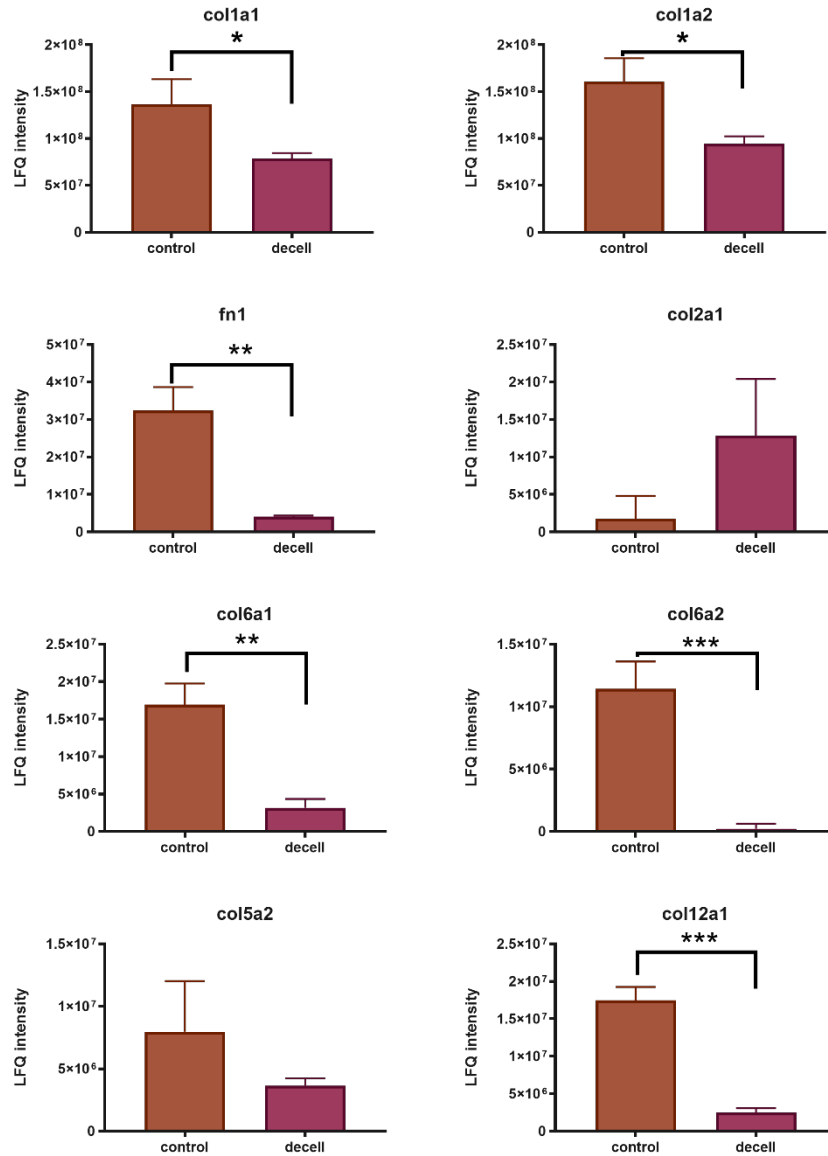


Figure B.1. Preliminary proteomic analysis of E14.5 control and decellularized skin showed a significant decrease in the relative amounts of ECM proteins, when comparing the label-free quantification (LfQ) intensity. GraphPad Prism was used to perform an unpaired t-test for protein control and decellularized group (n=3; bars=S.D.; \*0.0021 < p ≤ 0.0332; \*\*0.0002 < p ≤ 0.0021, \*\*\*0.0002 < p ≤ 0.0001, \*\*\*\* p < 0.0001).

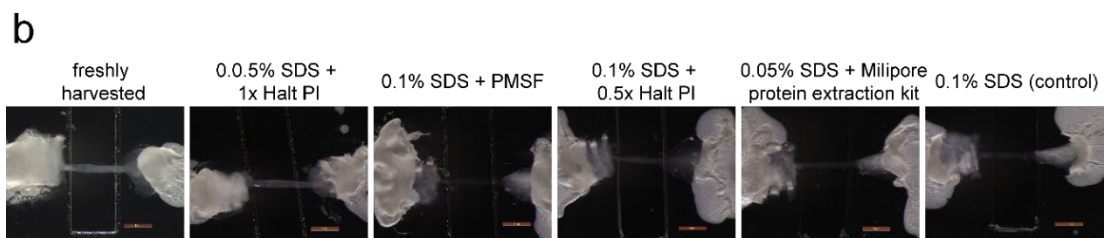
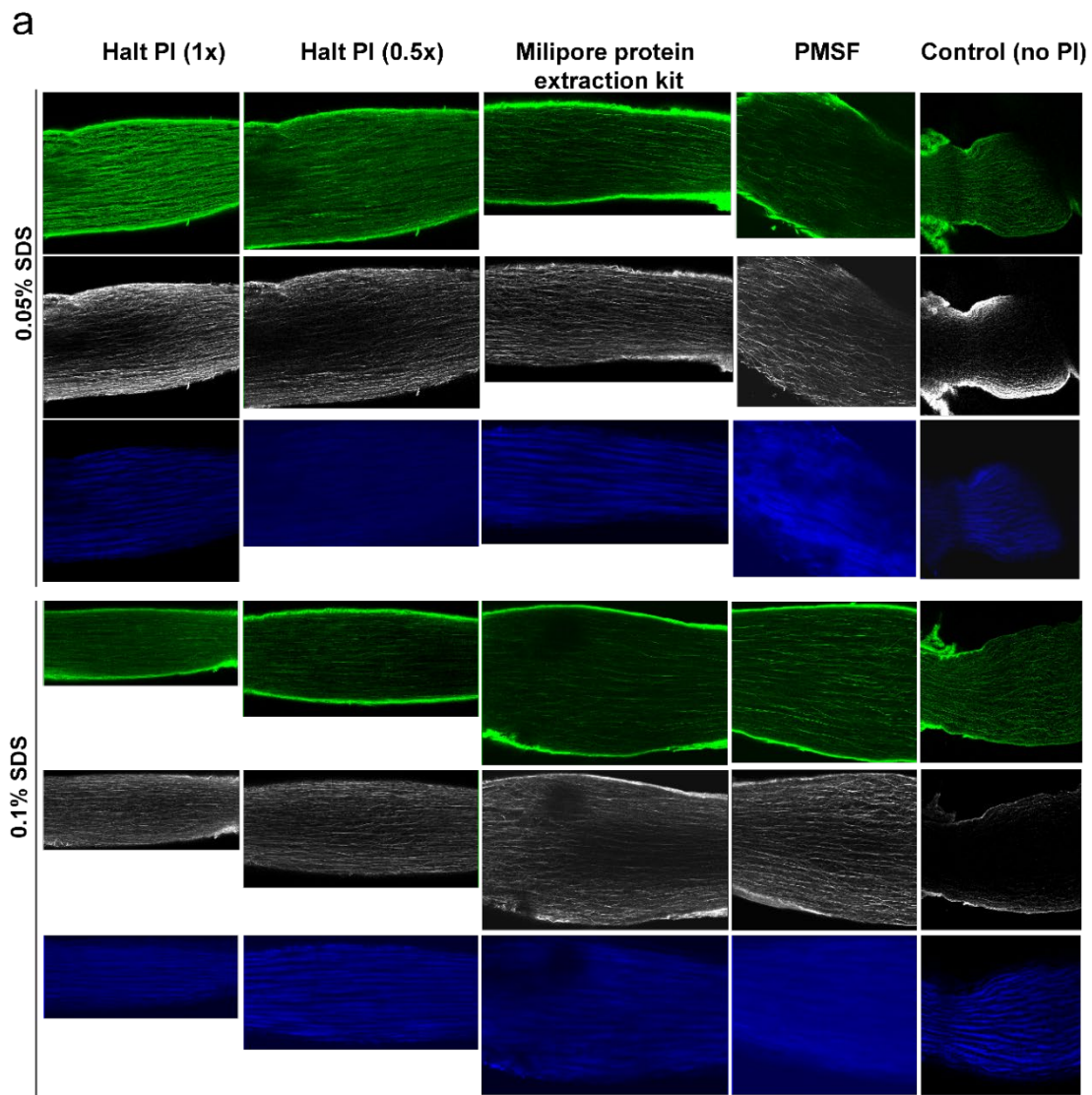


Figure B.2. Decellularization of postnatal (P3) tendons with different treatments. **a**. Representative confocal images of treated tendons after immunostaining showing WGA (green), fibrillin-2 (white), and DAPI (blue). All images were acquired at 10 $\times$ . **b**. Dissecting microscope images of control (freshly harvested) and treated tendons showing an increase in tissue transparency.

## REFERENCES

1. Bonnans, C., Chou, J. & Werb, Z. Remodelling the extracellular matrix in development and disease. *Nat. Rev. Mol. Cell Biol.* **15**, 786–801 (2014).
2. Mouw, J. K., Ou, G. & Weaver, V. M. Extracellular matrix assembly: a multiscale deconstruction. *Nat. Publ. Gr.* **15**, (2014).
3. Schwartz, M. A. Integrins and extracellular matrix in mechanotransduction. *Cold Spring Harb. Perspect. Biol.* **2**, (2010).
4. Lu, P., Takai, K., Weaver, V. M. & Werb, Z. Extracellular Matrix Degradation and Remodeling in Development and Disease.
5. Freedman, B. R. *et al.* The (dys)functional extracellular matrix ☆ HHS Public Access. *Biochim Biophys Acta Biochim Biophys Acta Pt B* **1853**, 3153–3164 (2016).
6. Rozario, T. & DeSimone, D. W. The extracellular matrix in development and morphogenesis: A dynamic view. *Dev. Biol.* **341**, 126–140 (2010).
7. Doyle, A. D. & Yamada, K. M. Mechanosensing via cell-matrix adhesions in 3D microenvironments. *Exp. Cell Res.* **343**, 60–66 (2016).
8. Lutolf, M. P. & Hubbell, J. A. Synthetic biomaterials as instructive extracellular microenvironments for morphogenesis in tissue engineering. *Nature Biotechnology* **23**, 47–55 (2005).
9. Rikitake, Y. & Takai, Y. Directional Cell Migration. Regulation by Small G Proteins, Nectin-like Molecule-5, and Afadin. in *International Review of Cell and Molecular Biology* **287**, 97–143 (Elsevier Inc., 2011).
10. Hynes, R. O. Integrins: Versatility, modulation, and signaling in cell adhesion. *Cell* **69**, 11–25 (1992).
11. Humphrey, J. D. Vascular Adaptation and Mechanical Homeostasis at Tissue, Cellular, and Sub-cellular Levels. (2007). doi:10.1007/s12013-007-9002-3
12. Swinehart, I. T., Schlientz, A. J., Quintanilla, C. A., Mortlock, D. P. & Wellik, D. M. Hox11 genes are required for regional patterning and integration of muscle, tendon and bone. *Dev.* **140**, 4574–4582 (2013).

13. Calve, S. & Simon, H.-G. Biochemical and mechanical environment cooperatively regulate skeletal muscle regeneration. *FASEB J.* **26**, 2538–2545 (2012).
14. Xu, X., Li, Z., Cai, L., Calve, S. & Neu, C. P. Mapping the Nonreciprocal Micromechanics of Individual Cells and the Surrounding Matrix Within Living Tissues. *Nat. Publ. Gr.* (2016). doi:10.1038/srep24272
15. Gattazzo, F., Urciuolo, A. & Bonaldo, P. Extracellular matrix: a dynamic microenvironment for stem cell niche. *Biochim. Biophys. Acta* **1840**, 2506–19 (2014).
16. Heinegård, D. & Saxne, T. The role of the cartilage matrix in osteoarthritis. *Nature Reviews Rheumatology* **7**, 50–56 (2011).
17. Connizzo, B. K., Yannascoli, S. M. & Soslowsky, L. J. Structure–function relationships of postnatal tendon development: A parallel to healing. *Matrix Biol.* **32**, 106–116 (2013).
18. Subramanian, A. & Schilling, T. F. Tendon development and musculoskeletal assembly: emerging roles for the extracellular matrix. (2015). doi:10.1242/dev.114777
19. Mecham, R. P. Overview of Extracellular Matrix. *Curr. Protoc. Cell Biol.* **00**, 10.1.1-10.1.14 (1998).
20. Zhang, G. *et al.* Development of tendon structure and function: Regulation of collagen fibrillogenesis. *Journal of Musculoskeletal Neuronal Interactions* (2005). doi:10.1016/j.biomaterials.2010.02.062
21. Birk, D. E., Zycband, E. I., Woodruff, S., Winkelmann, D. A. & Trelstad, R. L. Collagen fibrillogenesis in situ: Fibril segments become long fibrils as the developing tendon matures. *Dev. Dyn.* **208**, 291–298 (1997).
22. Banos, C. C., Thomas, A. H. & Kuo, C. K. Collagen fibrillogenesis in tendon development: Current models and regulation of fibril assembly. *Birth Defects Res. Part C - Embryo Today Rev.* **84**, 228–244 (2008).
23. Kadler, K. E., Hill, A., Canty-Laird, E. G., Ginsberg, M. & Schwarzbauer, J. Collagen fibrillogenesis: fibronectin, integrins, and minor collagens as organizers and nucleators. *Curr. Opin. Cell Biol.* **20**, 495–501 (2008).
24. Singh, P., Carraher, C. & Schwarzbauer, J. E. Assembly of fibronectin extracellular matrix. *Annu. Rev. Cell Dev. Biol.* **26**, 397–419 (2010).
25. Theocharis, A. D., Skandalis, S. S., Gialeli, C. & Karamanos, N. K. Extracellular matrix structure ☆. *Adv. Drug Deliv. Rev.* **97**, 4–27 (2016).

26. Screen, H. R. C., Berk, D. E., Kadler, K. E., Ramirez, F. & Young, M. F. Tendon Functional Extracellular Matrix. **17**, 793–799 (2015).
27. Singh, P., Carraher, C. & Schwarzbauer, J. E. Assembly of Fibronectin Extracellular Matrix ECM: extracellular matrix. *Annu. Rev. Cell Dev. Biol* **26**, 397–419 (2010).
28. Olivieri, J., Smaldone, S. & Ramirez, F. Fibrillin assemblies: extracellular determinants of tissue formation and fibrosis. doi:10.1186/1755-1536-3-24
29. Ramirez, F., Sakai, L. Y., Dietz, H. C. & Rifkin, D. B. Fibrillin microfibrils: Multipurpose extracellular networks in organismal physiology. *Physiological Genomics* **19**, 151–154 (2005).
30. Robinson, P. N. *et al.* The molecular genetics of Marfan syndrome and related disorders. *J Med Genet* **43**, 769–787 (2006).
31. Halper, J. & Kjaer, M. Basic Components of Connective Tissues and Extracellular Matrix: Elastin, Fibrillin, Fibulins, Fibrinogen, Fibronectin, Laminin, Tenascins and Thrombospondins. *Adv. Exp. Med. Biol.* **802**,
32. Charbonneau, N. L. *et al.* Microfibril Structure Masks Fibrillin-2 in Postnatal Tissues. *J. Biol. Chem.* **285**, 20242 (2010).
33. Kieltyl, C. M. • *et al.* Fibrillin-rich microfibrils: elastic biopolymers of the extracellular matrix 581. *Journal of Muscle Research and Cell Motility* **23**, (2002).
34. Bradshaw, M. J. & Smith, M. L. Multiscale relationships between fibronectin structure and functional properties. *Acta Biomater.* **10**, 1524–1531 (2014).
35. Bowers, S. L. K., Banerjee, I. & Baudino, T. A. The extracellular matrix: At the center of it all. *J. Mol. Cell. Cardiol.* **48**, 474–482 (2009).
36. Corda, S., Samuel, J. L. & Rappaport, L. Extracellular matrix and growth factors during heart growth. *Heart Failure Reviews* **5**, 119–130 (2000).
37. Zollinger, A. J. & Smith, M. L. Fibronectin, the extracellular glue. *Matrix Biol.* **60–61**, 27–37 (2017).
38. Astrof, S., Crowley, D. & Hynes, R. O. Multiple cardiovascular defects caused by the absence of alternatively spliced segments of fibronectin. (2007). doi:10.1016/j.ydbio.2007.07.005
39. Shawky, J. H. & Davidson, L. A. Tissue Mechanics and Adhesion during Embryo Development. doi:10.1016/j.ydbio.2014.12.005

40. Daley, W. P., Peters, S. B. & Larsen, M. Extracellular matrix dynamics in development and regenerative medicine. doi:10.1242/jcs.006064
41. Rosso, F., Giordano, A., Barbarisi, M. & Barbarisi, A. From Cell – ECM Interactions to Tissue Engineering. **180**, 174–180 (2004).
42. Frantz, C., Stewart, K. M. & Weaver, V. M. The extracellular matrix at a glance. *Journal of Cell Science* **123**, 4195–4200 (2010).
43. Ocken, A. R., Ku, M. M., Kinzer-Ursem, T. L. & Calve, S. Perlecan knockdown significantly alters extracellular matrix composition and organization during cartilage development. *Mol. Cell. Proteomics* mcp.RA120.001998 (2020). doi:10.1074/mcp.ra120.001998
44. Saleh, A. M., Jacobson, K. R., Kinzer-Ursem, T. L. & Calve, S. Dynamics of Non-Canonical Amino Acid-Labeled Intra- and Extracellular Proteins in the Developing Mouse. *Cell. Mol. Bioeng.* **12**, 495–509 (2019).
45. Rowe, R. G. & Weiss, S. J. Breaching the basement membrane: who, when and how? *Trends in Cell Biology* **18**, 560–574 (2008).
46. Schaefer, L. & Schaefer, R. M. Proteoglycans: From structural compounds to signaling molecules. *Cell and Tissue Research* **339**, 237–246 (2010).
47. Thottappillil, N. & Nair, P. D. Scaffolds in vascular regeneration: current status. *Vasc. Health Risk Manag.* **11**, 79–91 (2015).
48. Scarritt, M., Murdock, M. & Badylak, S. F. Biologic Scaffolds Composed of Extracellular Matrix for Regenerative Medicine. in *Principles of Regenerative Medicine* 613–626 (Elsevier, 2019). doi:10.1016/b978-0-12-809880-6.00035-7
49. Silva Garcia, J. M., Panitch, A. & Calve, S. Functionalization of hyaluronic acid hydrogels with ECM-derived peptides to control myoblast behavior. *Acta Biomater.* **84**, 169–179 (2019).
50. Kuo, C. K. & Smith, M. L. Biomaterial design motivated by characterization of natural extracellular matrices. *MRS Bull.* **39**, 18–24 (2014).
51. Jansen, K. A., Bacabac, R. G., Piechocka, I. K. & Koenderink, G. H. Cells actively stiffen fibrin networks by generating contractile stress. *Biophys. J.* **105**, 2240–2251 (2013).

52. Kang, H. *et al.* Nonlinear elasticity of stiff filament networks: Strain stiffening, negative normal stress, and filament alignment in fibrin gels. *J. Phys. Chem. B* **113**, 3799–3805 (2009).
53. Dusseiller, M. R., Smith, M. L., Vogel, V. & Textor, M. Microfabricated three-dimensional environments for single cell studies. *Biointerphases* **1**, P1–P4 (2006).
54. Pritchard, R. H., Huang, Y. Y. S. & Terentjev, E. M. Mechanics of biological networks: from the cell cytoskeleton to connective tissue. *Soft Matter* **10**, 1864–84 (2014).
55. Arruda, E. M., Calve, S. C., Garikipati, K., Grosh, K. & Narayanan, H. Characterization and modeling of growth and remodeling in tendon and soft tissue constructs. in *Mechanics of Biological Tissue* 63–75 (Springer Berlin Heidelberg, 2006). doi:10.1007/3-540-31184-X\_5
56. Wenstrup, R. J. *et al.* Type V collagen controls the initiation of collagen fibril assembly. *J. Biol. Chem.* **279**, 53331–53337 (2004).
57. Asgari, M., Latifi, N., Heris, H. K., Vali, H. & Mongeau, L. In vitro fibrillogenesis of tropocollagen type III in collagen type I affects its relative fibrillar topology and mechanics. *Sci. Rep.* **7**, (2017).
58. Brightman, A. O. *et al.* Time-lapse confocal reflection microscopy of collagen fibrillogenesis and extracellular matrix assembly in vitro. *Biopolymers* **54**, 222–234 (2000).
59. Pins, G. D., Christiansen, D. L., Patel, R. & Silver, F. H. Self-assembly of collagen fibers. Influence of fibrillar alignment and decorin on mechanical properties. *Biophys. J.* **73**, 2164–2172 (1997).
60. Susilo, M. E. *et al.* Prediction of equibiaxial loading stress in collagen-based extracellular matrix using a three-dimensional unit cell model. *Acta Biomater.* **9**, 5544–5553 (2012).
61. Lake, S. P., Hadi, M. F., Lai, V. K. & Barocas, V. H. Mechanics of a Fiber Network Within a Non-Fibrillar Matrix: Model and Comparison with Collagen-Agarose Co-gels. (2012). doi:10.1007/s10439-012-0584-6
62. Stylianopoulos, T. & Barocas, V. H. Volume-averaging theory for the study of the mechanics of collagen networks. *Comput. Methods Appl. Mech. Eng.* **196**, 2981–2990 (2007).
63. Britton, S. *et al.* Contribution of nascent cohesive fiber-fiber interactions to the non-linear elasticity of fibrin networks under tensile load. (2019). doi:10.1016/j.actbio.2019.05.068

64. Gautieri, A., Vesentini, S., Redaelli, A. & Ballarini, R. Modeling and measuring visco-elastic properties: From collagen molecules to collagen fibrils. *Int. J. Non. Linear. Mech.* **56**, 25–33 (2013).
65. Richardson, D. S. & Lichtman, J. W. Clarifying Tissue Clearing. *Cell* **162**, 246–257 (2015).
66. Orlich, M. & Kiefer, F. A qualitative comparison of ten tissue clearing techniques. (2017). doi:10.14670/HH-11-903
67. Lee, E. *et al.* ACT-PRESTO: Rapid and consistent tissue clearing and labeling method for 3-dimensional (3D) imaging. **6**, (2016).
68. Calve, S., Ready, A., Huppenbauer, C., Main, R. & Neu, C. P. Optical Clearing in Dense Connective Tissues to Visualize Cellular Connectivity In Situ. *PLoS One* **10**, e0116662 (2015).
69. Hou, B. *et al.* Scalable and DiI-compatible optical clearance of the mammalian brain. (2015). doi:10.3389/fnana.2015.00019
70. Hama, H. *et al.* ScaleS: an optical clearing palette for biological imaging. *Nat. Neurosci.* **18**, 1518–1529 (2015).
71. Keyes, J. T. *et al.* Design and Demonstration of a Microbiaxial Optomechanical Device for Multiscale Characterization of Soft Biological Tissues with Two-Photon Microscopy. *Microsc. Microanal.* **17**, 167–175 (2011).
72. Fata, B. *et al.* Regional structural and biomechanical alterations of the ovine main pulmonary artery during postnatal growth. *J. Biomech. Eng.* **135**, 021022 (2013).
73. Freedman, B. R. *et al.* Tendon healing affects the multiscale mechanical, structural and compositional response of tendon to quasi-static tensile loading. *J. R. Soc. Interface* **15**, 20170880 (2018).
74. Lee, A. H., Szczesny, S. E., Santare, M. H. & Elliott, D. M. Investigating mechanisms of tendon damage by measuring multi-scale recovery following tensile loading. *Acta Biomater.* **57**, 363–372 Contents (2017).
75. Swinehart, I. T. & Badylak, S. F. Extracellular matrix bioscaffolds in tissue remodeling and morphogenesis. *Developmental Dynamics* **245**, 351–360 (2016).
76. Wohl, A. P., Troilo, H., Collins, R. F., Baldock, C. & Sengle, G. Extracellular regulation of bone morphogenetic protein activity by the microfibril component fibrillin-1. *J. Biol. Chem.* **291**, 12732–12746 (2016).

77. de Almeida, P. G., Pinheiro, G. G., Nunes, A. M., Gonçalves, A. B. & Thorsteinsdóttir, S. Fibronectin assembly during early embryo development: A versatile communication system between cells and tissues. *Dev. Dyn.* **245**, 520–535 (2016).
78. Chung, K. *et al.* Structural and molecular interrogation of intact biological systems. *Nature* **497**, 332–7 (2013).
79. Ke, M.-T., Fujimoto, S. & Imai, T. SeeDB: a simple and morphology-preserving optical clearing agent for neuronal circuit reconstruction. *Nat. Publ. Gr.* **16**, (2013).
80. Neu, C. P., Novak, T., Gilliland, K. F., Marshall, P. & Calve, S. Optical clearing in collagen- and proteoglycan-rich osteochondral tissues. *Osteoarthr. Cartil.* **23**, 405–413 (2015).
81. Crapo, P. M., Gilbert, T. W. & Badylak, S. F. An overview of tissue and whole organ decellularization processes. *Biomaterials* **32**, 3233–3243 (2011).
82. Lumpkins, S. B., Pierre, N. & McFetridge, P. S. A mechanical evaluation of three decellularization methods in the design of a xenogeneic scaffold for tissue engineering the temporomandibular joint disc. *Acta Biomater.* **4**, 808–816 (2008).
83. Nakayama, K. H., Batchelder, C. A., Lee, C. I. & Tarantal, A. F. Decellularized Rhesus Monkey Kidney as a Three-Dimensional Scaffold for Renal Tissue Engineering. *Tissue Eng. Part A* **16**, 2207–2216 (2010).
84. Taghiabadi, E., Nasri, S., Shafieyan, S., Firoozinezhad, S. J. & Aghdami, N. Fabrication and characterization of spongy denuded amniotic membrane based scaffold for tissue engineering. *Cell J.* **16**, 476–487 (2015).
85. Yang, B. *et al.* Single-cell phenotyping within transparent intact tissue through whole-body clearing. *Cell* **158**, 945–958 (2014).
86. Calve, S., Odelberg, S. J. & Simon, H. G. A transitional extracellular matrix instructs cell behavior during muscle regeneration. *Dev. Biol.* **344**, 259–271 (2010).
87. Lin, J. B. *et al.* Imaging of Small Animal Peripheral Artery Disease Models: Recent Advancements and Translational Potential. *Int. J. Mol. Sci* **16**, 11131–11177 (2015).
88. Yang, B. *et al.* Single-Cell Phenotyping within Transparent Intact Tissue through Whole-Body Clearing. (2014). doi:10.1016/j.cell.2014.07.017
89. Tanaka, T. & Fillmore, D. J. Kinetics of swelling of gels. *J. Chem. Phys.* **70**, 1214–1218 (1979).

90. Tainaka, K. *et al.* Whole-Body Imaging with Single-Cell Resolution by Tissue Decolorization. *Cell* **159**, 911–924 (2014).
91. Chen, F., Tillberg, P. W. & Boyden, E. S. Expansion microscopy. *Science (80-. )*. **347**, 543–548 (2015).
92. George, E. L., Georges-Labouesse, E. N., Patel-King, R. S., Rayburn, H. & Hynes, R. O. Defects in mesoderm, neural tube and vascular development in mouse embryos lacking FN. *Development* **119**, 1079–1091 (1993).
93. Risau, W. & Lemmon, V. Changes in the Vascular Extracellular Matrix during Embryonic Vasculogenesis and Angiogenesis. *Dev. Biol.* **125**, 441–450 (1988).
94. Arteaga-Solis, E. *et al.* Regulation of limb patterning by extracellular microfibrils. *J. Cell Biol.* **154**, 275–281 (2001).
95. Kostrominova, T. Y. Application of WGA lectin staining for visualization of the connective tissue in skeletal muscle, bone, and ligament/tendon studies. *Microsc. Res. Tech.* **74**, 18–22 (2011).
96. Koyama, E. *et al.* Expression of syndecan-3 and tenascin-C: Possible involvement in periosteum development. *J. Orthop. Res.* **14**, 403–412 (1996).
97. Ros, M. A., Rivero, F. B., Hinchliffe, J. R. & Hurle, J. M. Immunohistological and ultrastructural study of the developing tendons of the avian foot. *Anat. Embryol. (Berl)*. **192**, 483–496 (1995).
98. Zhang, H., Hu, W. & Ramirez, F. Developmental expression of fibrillin genes suggests heterogeneity of extracellular microfibrils. *J. Cell Biol.* **129**, 1165–1176 (1995).
99. Arikawa-Hirasawa, E., Watanabe, H., Takami, H., Hassell, J. R. & Yamada, Y. Perlecan is essential for cartilage and cephalic development. *Nat. Genet.* **23**, 354–358 (1999).
100. Landolt, R. M., Vaughan, L., Winterhalter, K. H. & Zimmermann, D. R. Versican is selectively expressed in embryonic tissues that act as barriers to neural crest cell migration and axon outgrowth. *Development* **121**, 2303–2312 (1995).
101. Huang, A. H. *et al.* Musculoskeletal integration at the wrist underlies the modular development of limb tendons. *Dev.* **142**, 2431–2441 (2015).
102. Yamamoto-Shiraishi, Y. I. & Kuroiwa, A. Wnt and BMP signaling cooperate with Hox in the control of Six2 expression in limb tendon precursor. *Dev. Biol.* **377**, 363–374 (2013).

103. Hurler, J. M., Kitten, G. T., Sakai, L. Y., Volpin, D. & Solursh, M. Elastic extracellular matrix of the embryonic chick heart: an immunohistological study using laser confocal microscopy. *Dev. Dyn.* **200**, 321–32 (1994).
104. Hurler, J. M., Ros, M. A., Hinchliffe, J. R., Critchlow, M. A. & Genis-Galvez, J. M. The extracellular matrix architecture relating to myotendinous pattern formation in the distal part of the developing chick limb: An ultrastructural, histochemical and immunocytochemical analysis. *Cell Differ. Dev.* **27**, 103–120 (1989).
105. Hardman, M. J., Sisi, P., Banbury, D. N. & Byrne, C. Patterned acquisition of skin barrier function during development. *Development* **125**, 1541–1552 (1998).
106. Hynes, R. O. & Naba, A. Overview of the matrisome--an inventory of extracellular matrix constituents and functions. *Cold Spring Harb. Perspect. Biol.* **4**, a004903 (2012).
107. Kjær, M. Role of Extracellular Matrix in Adaptation of Tendon and Skeletal Muscle to Mechanical Loading. *Physiological Reviews* **84**, 649–698 (2004).
108. Hartman, C. D., Isenberg, B. C., Chua, S. G. & Wong, J. Y. Vascular smooth muscle cell durotaxis depends on extracellular matrix composition. doi:10.1073/pnas.1611324113
109. Rowlands, A. S., George, P. A. & Cooper-White, J. J. Directing osteogenic and myogenic differentiation of MSCs: interplay of stiffness and adhesive ligand presentation. *Am J Physiol Cell Physiol* **295**, 1037–1044 (2008).
110. Li, L., Eyekmans, J. & Chen, C. S. Designer biomaterials for mechanobiology. *Nature Materials* **16**, 1164–1168 (2017).
111. Klotzsch, E. *et al.* Fibronectin forms the most extensible biological fibers displaying switchable force-exposed cryptic binding sites. (2009).
112. Li, W. *et al.* Fibrin Fiber Stiffness Is Strongly Affected by Fiber Diameter, but Not by Fibrinogen Glycation. *Biophys. J.* **110**, 1400–1410 (2016).
113. Eriksen, T. A., Wright, D. M., Purslow, P. P. & Duance, V. C. Role of Ca<sup>2+</sup> for the mechanical properties of fibrillin. *Proteins Struct. Funct. Genet.* **45**, 90–95 (2001).
114. Liu Shen, Z., Kahn, H., Ballarini, R. & Eppell, S. J. Viscoelastic Properties of Isolated Collagen Fibrils. *Biophysj* **100**, 3008–3015 (2011).
115. Acuna, A., Drakopoulos, M. A., Leng, Y., Goergen, C. J. & Calve, S. Three-dimensional visualization of extracellular matrix networks during murine development. *Dev. Biol.* **435**, 122–129 (2018).

116. Bar-Kochba, E., Toyjanova, J., Andrews, E., Kim, K.-S. & Franck, C. A Fast Iterative Digital Volume Correlation Algorithm for Large Deformations. *Exp. Mech.* **C**, 261–274 (2015).
117. Tinevez, J. Y. *et al.* TrackMate: An open and extensible platform for single-particle tracking. *Methods* **115**, 80–90 (2017).
118. Midgett, D. E. *et al.* The pressure-induced deformation response of the human lamina cribrosa: Analysis of regional variations. *Acta Biomater.* **53**, 123–139 (2017).
119. Zhang, Y. & Ben Hamza, A. Vertex-based anisotropic smoothing of 3D mesh data. in *Canadian Conference on Electrical and Computer Engineering* 202–205 (Institute of Electrical and Electronics Engineers Inc., 2006). doi:10.1109/CCECE.2006.277433
120. Yan, Z., Matuszewski, B. J., Shark, L. K. & Moore, C. J. Medical image segmentation using new hybrid level-set method. in *Proceedings - 5th International Conference BioMedical Visualization, Information Visualization in Medical and Biomedical Informatics, MediVis 2008* 71–76 (2008). doi:10.1109/MediVis.2008.12
121. Fang, Q. & Boas, D. A. Tetrahedral mesh generation from volumetric binary and grayscale images. in *Proceedings - 2009 IEEE International Symposium on Biomedical Imaging: From Nano to Macro, ISBI 2009* 1142–1145 (2009). doi:10.1109/ISBI.2009.5193259
122. Muhammad, M. & Choi, T. S. Sampling for shape from focus in optical microscopy. *IEEE Trans. Pattern Anal. Mach. Intell.* **34**, 564–573 (2012).
123. Lakadamyali, M., Babcock, H., Bates, M., Zhuang, X. & Lichtman, J. 3D Multicolor Super-Resolution Imaging Offers Improved Accuracy in Neuron Tracing. *PLoS One* **7**, e30826 (2012).
124. Chen, H. & Kassab, G. S. Microstructure-based biomechanics of coronary arteries in health and disease. *J. Biomech.* (2016). doi:10.1016/j.jbiomech.2016.03.023
125. Fang, F. & Lake, S. P. Experimental evaluation of multiscale tendon mechanics. *J. Orthop. Res.* **35**, 1353–1365 (2017).
126. Bancelin, S. *et al.* Ex vivo multiscale quantitation of skin biomechanics in wild-type and genetically-modified mice using multiphoton microscopy. *Sci. Rep.* **5**, (2015).
127. Rosakis, P., Notbohm, J. & Ravichandran, G. A model for compression-weakening materials and the elastic fields due to contractile cells. *J. Mech. Phys. Solids* **85**, 16–32 (2015).

128. Khodabakhshi, G. *et al.* Measuring three-dimensional strain distribution in tendon. *J. Microsc.* **249**, 195–205 (2013).
129. Böl, M., Ehret, A. E., Leichsenring, K. & Ernst, M. Tissue-scale anisotropy and compressibility of tendon in semi-confined compression tests. doi:10.1016/j.jbiomech.2015.01.024
130. Jiang, M. *et al.* Clamping soft biologic tissues for uniaxial tensile testing: A brief survey of current methods and development of a novel clamping mechanism. *J. Mech. Behav. Biomed. Mater.* **103**, 103503 (2020).
131. Yoshida, K., Mahendroo, M., Vink, J., Wapner, R. & Myers, K. Material properties of mouse cervical tissue in normal gestation. *Acta Biomater.* **36**, 195–209 (2016).
132. Calve, S., Lytle, I. F., Grosh, K., Brown, D. L. & Arruda, E. M. Implantation increases tensile strength and collagen content of self-assembled tendon constructs. *J Appl Physiol* **108**, 875–881 (2010).
133. Henninger, H. B., Ellis, B. J., Scott, S. A. & Weiss, J. A. Contributions of elastic fibers, collagen, and extracellular matrix to the multiaxial mechanics of ligament. *J. Mech. Behav. Biomed. Mater.* (2019). doi:10.1016/j.jmbbm.2019.07.018
134. Humphrey, J. D., Vawter, D. L. & Vito, R. P. Quantification of strains in biaxially tested soft tissues. *J. Biomech.* **20**, 59–65 (1987).
135. Svensson, R. B., Smith, S. T., Moyer, P. J. & Magnusson, S. P. Effects of maturation and advanced glycation on tensile mechanics of collagen fibrils from rat tail and Achilles tendons. *Acta Biomater.* (2018). doi:10.1016/j.actbio.2018.02.005
136. Bradshaw, M. J., Hoffmann, G. A., Wong, J. Y. & Smith, M. L. Fibronectin fiber creep under constant force loading. *Acta Biomater.* **88**, 78–85 (2019).
137. Elhebeary, M., Emon, M. A. B., Aydin, O. & Saif, M. T. A. A novel technique for in situ uniaxial tests of self-assembled soft biomaterials. *Lab Chip* **19**, 1153–1161 (2019).
138. Jayyosi, C. *et al.* The mechanical response of the mouse cervix to tensile cyclic loading in term and preterm pregnancy. *Acta Biomater.* **78**, 308–319 (2018).
139. Ingber, D. E. Mechanical control of tissue morphogenesis during embryological development. *Int. J. Dev. Biol.* **50**, 255–266 (2006).
140. Shinde, A. *et al.* Autocrine fibronectin inhibits breast cancer metastasis. *Mol. Cancer Res.* **16**, 1579–1589 (2018).

141. Jordahl, S. *et al.* Engineered Fibrillar Fibronectin Networks as Three-Dimensional Tissue Scaffolds. *Adv. Mater.* **31**, (2019).
142. Ruedinger, K. L., Medero, R., Rolda'n, A. & Rolda'n-Alzate, R. Fabrication of Low-Cost Patient-Specific Vascular Models for Particle Image Velocimetry. *Cardiovasc. Eng. Technol.* **10**,
143. Solaris™ Product Information | Smooth-On, Inc. Available at: <https://www.smooth-on.com/products/solaris/>. (Accessed: 23rd July 2020)
144. Arruda, E. M., Calve, S., Dennis, R. G., Mundy, K. & Baar, K. Regional variation of tibialis anterior tendon mechanics is lost following denervation. *J Appl Physiol* **101**, 1113–1117 (2006).
145. Pan, X. S., Li, J., Brown, E. B. & Kuo, C. K. Embryo movements regulate tendon mechanical property development. *Philos. Trans. R. Soc. Lond. B. Biol. Sci.* **373**, 20170325 (2018).
146. Marturano, J. E., Arena, J. D., Schiller, Z. A., Georgakoudi, I. & Kuo, C. K. Characterization of mechanical and biochemical properties of developing embryonic tendon. *Proc Natl Acad Sci USA* doi:10.1073/pnas.1300135110
147. Andriotis, O. G. *et al.* Structure-mechanics relationships of collagen fibrils in the osteogenesis imperfecta mouse model. *J. R. Soc. Interface* **12**, (2015).
148. Eekhoff, J. D., Fang, F. & Lake, S. P. Multiscale mechanical effects of native collagen cross-linking in tendon. *Connect. Tissue Res.* **59**, 410–422 (2018).
149. Byron, A., Humphries, J. D. & Humphries, M. J. Defining the extracellular matrix using proteomics. *Int. J. Exp. Pathol.* **94**, 75–92 (2013).
150. Gautieri, A., Vesentini, S., Redaelli, A. & Buehler, M. J. Hierarchical structure and nanomechanics of collagen microfibrils from the atomistic scale up. *Nano Lett.* **11**, 757–766 (2011).
151. Litvinov, R. I. & Weisel, J. W. Fibrin mechanical properties and their structural origins. *Matrix Biology* **60–61**, 110–123 (2017).
152. Acuna, A., Sofronici, S. H., Goergen, C. J. & Calve, S. In Situ Measurement of Native Extracellular Matrix Strain. *Exp. Mech.* 1–15 (2019).
153. Sergueeva, A. V., Zhou, J., Meacham, B. E. & Branagan, D. J. Gage length and sample size effect on measured properties during tensile testing. *Mater. Sci. Eng. A* **526**, 79–83 (2009).

154. Yoon, J. I. *et al.* Obtaining Reliable True Plastic Stress-Strain Curves in a Wide Range of Strains Using Digital Image Correlation in Tensile Testing . *대한금속·재료학회지 (Korean J. Met. Mater.)* **54**, 231–236 (2016).
155. Wood, L. K., Arruda, E. M. & Brooks, S. V. Regional stiffening with aging in tibialis anterior tendons of mice occurs independent of changes in collagen fibril morphology. *J Appl Physiol* **111**, 999–1006 (2011).
156. Starborg, T. *et al.* Using transmission electron microscopy and 3View to determine collagen fibril size and three-dimensional organization. *Nat. Protoc.* **8**, 1433–1448 (2013).
157. Graham, J., Raghunath, M. & Vogel, V. Fibrillar fibronectin plays a key role as nucleator of collagen i polymerization during macromolecular crowding-enhanced matrix assembly. *Biomater. Sci.* **7**, 4519–4535 (2019).
158. Smith, M. L. *et al.* Force-Induced Unfolding of Fibronectin in the Extracellular Matrix of Living Cells. **5**, (2007).
159. Kalson, N. S. *et al.* A structure-based extracellular matrix expansion mechanism of fibrous tissue growth. *Elife* (2015). doi:10.7554/eLife.05958.001
160. Duncan, N. A., Bruehlmann, S. B., Hunter, C. J., Shao, X. & Kelly, E. J. In situ cell-matrix mechanics in tendon fascicles and seeded collagen gels: implications for the multiscale design of biomaterials. *Comput. Methods Biomech. Biomed. Engin.* **17**, 39–47 (2014).
161. Wang, R., Brewster, L. P., Gleason, R. L. & Woodruff, G. W. In-situ characterization of the uncrimping process of arterial collagen fibers using two-photon confocal microscopy and digital image correlation. (2013). doi:10.1016/j.jbiomech.2013.08.001
162. Nierenberger, M., Fargier, G., Ahzi, S. & Rémond, Y. Evolution of the three-dimensional collagen structure in vascular walls during deformation : an in situ mechanical testing under multiphoton microscopy observation. *Biomech. Model. Mechanobiol.* 693–702 (2015). doi:10.1007/s10237-014-0630-4
163. Petersen, T. H., Calle, E. A., Colehour, M. B. & Niklason, L. E. Matrix Composition and Mechanics of Decellularized Lung Scaffolds. *Cells Tissues Organs* **195**, 222–231 (2012).
164. Lilledahl, M. B., Skallerud, B. & Davies, C. Mechanical properties of tissue determined by multiphoton microscopy. *Multiphot. Microsc. Biomed. Sci. IX* **7183**, 718325 (2009).
165. Szczyzny, S. E. & Elliott, D. M. Interfibrillar shear stress is the loading mechanism of collagen fibrils in tendon. *Acta Biomater.* **10**, 2582–2590 (2014).

## PUBLICATIONS

1. **Acuna, A.\***, Drakopoulos, M. A.\*, Leng, Y., Goergen, C. J., Calve, S. (2018), “Three-dimensional visualization of extracellular matrix networks during murine development”, *Developmental Biology*, DOI: 10.1016/j.ydbio.2017.12.022.
2. **Acuna, A.\***, Berman, A. G.\*, Damen, F. W.\*, Meyers, B. A.\*, Adelsperger, A. R., Bayer, K., Brindise, M. C., Bungart, B., Kiel, A., Morrison, R., Muskat, J., Wasilczuk, K., Wen, Y., Zhang, J., Zito, P., and Goergen, C. J., (2018), “Computational Fluid Dynamics of Vascular Disease in Animal Models,” *ASME J. Biomech. Eng.*, 140(8), p. 080801. doi:10.1115/1.4039678.
3. **Acuna, A.**, Sofrinici, S.L., Goergen, C.J., Calve, S. (2019) “*In situ* characterization of native extracellular matrix deformation,” *Experimental Mechanics*, DOI: 10.1007/s11340-019-00499-y
4. Sangha, G. S., Busch A., **Acuna, A.**, Berman, A. G., Phillips, E. H., Trenner, M., Eckstein, H. H., Maegdefessel, L., Goergen, C. J. (2019).” Effects of Iliac Stenosis on Abdominal Aortic Aneurysm Formation in Mice and Humans”, *Journal of Vascular Research*. doi: 10.1159/000501312.
5. Jacobson, K.R., Lipp, S.N., **Acuna, A.**, Leng, Y., Bu, Y., Calve, S. “Comparative Analysis of the Extracellular Matrix Proteome Across the Myotendinous Junction”. *under review*